Laboratory, Field and Numerical Investigations of Holmboe's Instability

by

Edmund W. Tedford

B.A.Sc., The University of New Brunswick, 1997
M.A.Sc., The University of British Columbia, 1999

A THESIS SUBMITTED IN PARTIAL FULFILMENT OF
THE REQUIREMENTS FOR THE DEGREE OF

Doctor of Philosophy

in

The Faculty of Graduate Studies

(Civil Engineering)

The University Of British Columbia

(Vancouver)

April 2009

© Edmund W. Tedford 2009

Abstract

The instabilities that occur at a sheared density interface are investigated in the laboratory, the Fraser River estuary and with Direct Numerical Simulations (DNS).

In the laboratory, symmetric Holmboe instabilities are observed during steady, maximal two-layer exchange flow in a long channel of rectangular cross section. Internal hydraulic controls at each end of the channel isolate the subcritical region within the channel from disturbances in the reservoirs. Inside the channel, the instabilities form cusp-like waves that propagate in both directions. The phase speed of the instabilities is consistent with linear theory, and increases along the length of the channel as a result of the gradual acceleration of each layer. This acceleration causes the wavelength of any given instability to increase in the direction of flow. As the instabilities are elongated new instabilities form, and as a consequence, the average wavelength is almost constant along the length of the channel.

In the Fraser River estuary, a detailed stability analysis is conducted based on the Taylor-Goldstein (TG) equation, and compared to direct observations in the estuary. We find that each set of instabilities observed coincides with an unstable mode predicted by the TG equation. Each of these instabilities occurs in a region where the gradient Richardson number is less than the critical value of 1/4. Both the TG predictions and echosoundings indicate the instabilities are concentrated either above or below the density interface. These 'one-sided' instabilities are closer in structure to the Holmboe instability than to the Kelvin-Helmholtz instability. Although the dominant source of mixing in the estuary appears to be caused by shear instability, there is also evidence of small-scale overturning due to boundary layer turbulence when the tide produces strong near-bed velocities.

Many features of the numerical simulations are consistent with linear theory and the laboratory experiments. However, inherent differences between the DNS and the experiments are responsible for variations in the dominant wavenumber and amplitude of the wave field. The simulations exhibit a nonlinear 'wave coarsening' effect, whereby the energy is shifted to lower wavenumber in discrete jumps. This process is, in part, related to the

occurrence of ejections of mixed fluid away from the density interface. In the case of the laboratory experiment, energy is transferred to lower wavenumber by the 'stretching' of the wave field by a gradually varying mean velocity. This stretching of the waves results in a reduction in amplitude compared to the DNS. The results of the comparison show the dependence of the nonlinear evolution of a Holmboe wave field on temporal and spatial variations of the mean flow.

Table of Contents

Abstract ii

Table of Contents iv

List of Tables vii

List of Figures viii

Acknowledgments x

Statement of Co-Authorship xi

1 Introduction 1
- 1.1 Linear Stability Analysis: the Taylor-Goldstein Equation . . 2
  - 1.1.1 The Three Basic Unstable Modes 3
  - 1.1.2 Symmetric Holmboe Instability 9
  - 1.1.3 Asymmetry and One-sidedness 10
  - 1.1.4 Smooth Profiles 11
  - 1.1.5 Eigenfunctions 13

Bibliography 16

2 Holmboe Instabilities in a Laboratory Exchange Flow . . 18
- 2.1 Introduction 18
- 2.2 Background Theory 21
  - 2.2.1 Hydraulics of Exchange Flow 21
  - 2.2.2 Dispersion Relation and Instability 21
- 2.3 Experimental Setup 24
- 2.4 Evolution of Mean Flow 27
- 2.5 Wave Evolution 30
- 2.6 Summary and Conclusions 36

Bibliography 38

3 Shear Instability in the Fraser River Estuary 40
3.1 Introduction 40
3.2 Site Description and Data Collection 41
3.3 General Description of the Salinity Intrusion 44
3.3.1 High Discharge 44
3.3.2 Low Discharge 46
3.4 Stability of Stratified Shear Flows 48
3.4.1 Taylor-Goldstein Equation 48
3.4.2 Miles-Howard Criterion 48
3.4.3 Mixing Layer Solution 49
3.4.4 Solution of the TG Equation for Observed Profiles . . 50
3.5 Results 51
3.6 Small Scale Overturns and Bottom Stress 59
3.7 Discussion 60
3.8 Conclusions 62

Bibliography 64

4 Holmboe Wave Fields in Simulation and Experiment . . . 67
4.1 Introduction 67
4.2 Linear Stability of Stratified Shear Layers 69
4.3 Methods 70
4.3.1 Description of the Numerical Simulations 70
4.3.2 Description of the Laboratory Experiment 73
4.4 Wave Structure 73
4.5 Phase Speed 76
4.6 Spectral Evolution 77
4.6.1 Frequency Shifting 78
4.6.2 Wave Energy Spectra 80
4.7 Wave Growth and Amplitude 82
4.7.1 Wave Growth 83
4.7.2 Comparison of Saturated Amplitudes 84
4.8 Conclusions 86

Bibliography 88

5 Conclusion 91
5.1 Summary 91
5.2 The Occurrence of Holmboe and Holmboe-Like Instabilities . 92

5.3 Contributions to the Study of Shear Instabilities in Stratified Flows 92
5.3.1 Laboratory Experiments 92
5.3.2 Field Experiments 93
5.3.3 Direct Numerical Simulations 94
5.4 Future Research 94

Bibliography 96

List of Tables

2.1 Experimental parameters 24
2.2 Summary of laboratory experiments 26

3.1 Transect details 42

4.1 Basic parameters of the simulations and laboratory experiments 72

List of Figures

1.1 Schematic of piecewise linear profiles 4
1.2 Dispersion relation for piecewise linear profiles 5
1.3 Sketches of three basic instabilities 7
1.4 Piecewise linear fit of laboratory profiles 9
1.5 Stability diagram 11
1.6 Dispersion relation for piecewise linear and smooth profiles . 12
1.7 Eigenfunctions 14
1.8 Displacement of dye lines 15

2.1 Close up image of interface 20
2.2 Definition sketch for piecewise linear profiles used in the analysis of Holmboe instabilities. 22
2.3 Celerity dispersion relations 23
2.4 Experimental setup 25
2.5 Phase speed 28
2.6 Interface statistics 29
2.7 Wave characteristics 31
2.8 Traced characteristics and statistics 33
2.9 Spectral evolution 35
2.10 Schematic of wave stretching and formation 36

3.1 Map of the lower 27 km of the Fraser River 41
3.2 Observed tides at Point Atkinson and New Westminster . . . 43
3.3 Echo soundings observed during high discharge 45
3.4 Echo soundings observed during low discharge 47
3.5 Transect 1 stability analysis 52
3.6 Transect 2 stability analysis 53
3.7 Transect 3 stability analysis 55
3.8 Transect 4 stability analysis 56
3.9 Transect 5 stability analysis 57
3.10 Transect 6 stability analysis 58
3.11 Selected density profiles 60

4.1 Growth rate and dispersion relations for the DNS 70
4.2 Evolution of the background profiles 71
4.3 Spatial changes in $U(z)$ and layer depths in the laboratory . . 74
4.4 Sample density fields from the laboratory experiments and the simulations 75
4.5 Wave characteristics in the laboratory experiments and the simulations 77
4.6 Traced wave characteristics 78
4.7 Spectral evolution in the laboratory experiments and the simulations 80
4.8 Growth of kinetic energy in the simulations 84

Acknowledgments

I would like to thank my supervisory committee for its guidance. Special thanks to my supervisor, Greg Lawrence, for his unyielding support and for giving me all the freedom I could hope for. Special thanks to Roger Pieters for his support in the laboratory and the field and to Rich Pawlowicz for inviting me on the initial cruises on the Fraser River. In addition, I would like to thank my family and friends for their patience and support over the course of this work.

Statement of Co-Authorship

The authors of Chapter 2 are myself, R. Pieters and G. Lawrence. With the exception of extensive discussion and editing, I was responsible for all aspects of the research and the manuscript preparation. A version of this chapter has been accepted for publication subject to revision in the Journal of Fluid Mechanics.

The authors of Chapter 3 are myself, J.R. Carpenter, R. Pawlowicz, R. Pieters and G.A. Lawrence. A version of this chapter has been submitted for publication in the Journal of Geophysical Research. My contributions to the work are as follows:

- The research program was developed by R. Pawlowicz, myself and J.R. Carpenter.
- I participated in every cruise and was responsible for the largest part of the data collection.
- I was responsible for all of the data analysis.
- I prepared the initial manuscript. J.R. Carpenter made additions particularly in describing the theory and the results of the analysis.

The authors of Chapter 4 are J.R. Carpenter, myself, M. Rahmani and G.A. Lawrence. A version of this chapter is in preparation for submission for publication.

- J.R. Carpenter and I initialized the research.
- I described the relevant details of the laboratory experiments.
- I developed the analyses of the laboratory data and contributed to adapting the analyses to the simulations. J.R. Carpenter and I, together, identified the basic concepts used to interpret the results.
- J.R. Carpenter prepared the manuscript and I made additions.

Chapter 1

Introduction

The primary motivation for studying shear instabilities, such as the Holmboe instability, is to better understand and predict mixing. Although such instabilities are not the only mechanism that causes mixing, they are, in many cases the dominant one. The Fraser River estuary is a good example of a stratified shear flow where shear instabilities control mixing [Geyer & Farmer, 1989]. The frequent occurrence of strong vertical gradients in density and velocity in the estuary provides ideal conditions for generating these instabilities.

Before examining instabilities in a system as complex as the Fraser River estuary it is helpful to examine them in the laboratory. The first component of this study is therefore, to conduct laboratory experiments that generate shear instabilities that are similar to those that occur in nature. The experiments were carried out in the two-layer exchange flow facility used by Zhu & Lawrence [2001]. The shear instabilities form at the density interface of two layers of water of different salinity (density). The two layers are flowing in opposite directions so that the vertical gradient of the streamwise velocity (shear) is centered on, and maximized at, the density interface. The sill in Zhu & Lawrence [2001] was removed resulting in simplified flow and to allow a more thorough study of the instabilities. With the aid of dye and particles, illuminated by laser light, images of the instabilities were captured. The combined use of digital imaging and spatial-temporal filtering allowed a more thorough description of the instabilities than has been previously achieved. The background for, and results of, the laboratory experiments are described in Chapter 2.

The second component of this study is observation of shear instabilities in the Fraser River estuary and comparison of these observations with predictions from linear stability analysis. The observations were collected in the salinity stratified region of the estuary during periods of strong shear. They include: echosoundings that show the structure of the instabilities, velocity measurements to quantify the shear, and temperature and conductivity measurements to quantify the density stratification. Results from the Fraser River estuary are described in Chapter 3.

The third component of this study is a comparison of the results from the laboratory experiments with direct numerical simulations (DNS). Because the linear stability analysis used in Chapters 2 and 3 is most accurate when the instabilities are very small, this analysis does not provide a complete description of the development of the instabilities. The nonlinear effects that become important at larger amplitudes are accurately described with DNS. There are, however, some differences between DNS and real flows associated with boundary and initial conditions, as well as computing power limitations, that limit the predictive capabilities of DNS. The results of the comparison between the laboratory experiments and DNS are discussed in Chapter 4.

The background information specific to each of these three components will be reviewed at the beginning of each of the respective chapters. In all three cases (Chapters 2, 3 and 4), predictions based on the Taylor-Goldstein equation are used to understand the basic behaviour of the instabilities; i.e. phase speed, wavelength and vertical structure. Because of its importance generally in stratified shear flows and particularly in this study, several illustrative solutions of the equation are discussed in detail in the remaining sections of this chapter.

1.1 Linear Stability Analysis: the Taylor-Goldstein Equation

The Taylor-Goldstein (TG) equation results from application of the method of normal modes to simplified equations of motion for stratified shear flow. It is assumed that the fluid is inviscid, incompressible, non diffusive and that the background flow is parallel (density and velocity are horizontally uniform in the background). The Boussinesq approximation is also made. Although the TG equation was originally derived for studying atmospheric dynamics [Taylor, 1931; Goldstein, 1931] it is also applicable to the flow of stratified water considered here. For a thorough derivation and a description of the assumptions see Drazin & Reid [1982]. The Taylor-Goldstein equation is:

$$\frac{d^2\hat{\psi}}{dz^2} + \Big[\frac{N^2}{(U-c)^2} - \frac{d^2U/dz^2}{U-c} - k^2\Big]\hat{\psi} = 0, \tag{1.1}$$

where the streamfunction of the perturbation is given by

$$\psi(x,z,t) = \hat{\psi}(z)e^{ik(x-ct)}. \tag{1.2}$$

The vertical coordinate is given by z. $U(z)$ is the background profile of the horizontal velocity. $N(z)$ is the profile of the Brunt Vaisala frequency, given by $N^2 = -(g/\rho_0)(d\rho/dz)$, where g is the gravitational acceleration, ρ is the density and ρ_0 is a reference density. With the addition of boundary conditions at the top and bottom (1.1) defines an eigenvalue problem for the complex phase speed, c, given the wavenumber, k. The resulting eigenfunction $\hat{\psi}(z)$ gives the vertical mode shape, from which we can determine where in the vertical the greatest displacements will occur. The dispersion relation, $c(k)$, will be used in this section to illustrate the three basic instability mechanisms that occur in a stably stratified shear flow. In later chapters calculated dispersion relations will be compared with observations. In these cases the Taylor-Goldstein equation is solved analytically for piecewise linear profiles [Drazin & Reid, 1982] and numerically for continuous profiles [Moum *et al.*, 2003]. The results presented here are for vertically bounded flow (i.e. the vertical velocity of the perturbation and therefore $\hat{\psi}$ are equal to zero).

1.1.1 The Three Basic Unstable Modes

The three sets of piecewise linear profiles shown in figure 1.1 can be considered the basic building blocks in the study of shear instability in stratified flow. With piecewise linear profiles there is one eigenvalue for each step in vorticity and two for each step in density. The vorticity steps are located at the kinks in the velocity profile, i.e. where the shear, dU/dz, changes. The two steps in vorticity in figure 1.1a will support one mode each. The two density steps in figure 1.1b will support four modes in total, two for each density step. The set of profiles in figure 1.1c will support three modes, one for the step in vorticity and two for the step in density. The three sets of profiles are referred to here as the Rayleigh, Taylor and Holmboe cases respectively.

In figure 1.2 the calculated eigenvalues, c, are plotted as solid lines against wavenumber, k, giving the dispersion relation for each set of profiles in figure 1.1. The wave number is nondimensionalized by the length scale h and the velocity is nondimensionalized by $\Delta U/2$. In all three cases ΔU is the change in velocity that occurs over h (see figure 1.1). The dispersion relation shown for the Rayleigh case is therefore general as all the dimensions have been accounted for. Because the nondimensionalization does not account for changes in density the dispersion relations of the Taylor and Holmboe cases will change when the size of the density step is changed. The dispersion relations for these two cases are general, but only in a qualitative

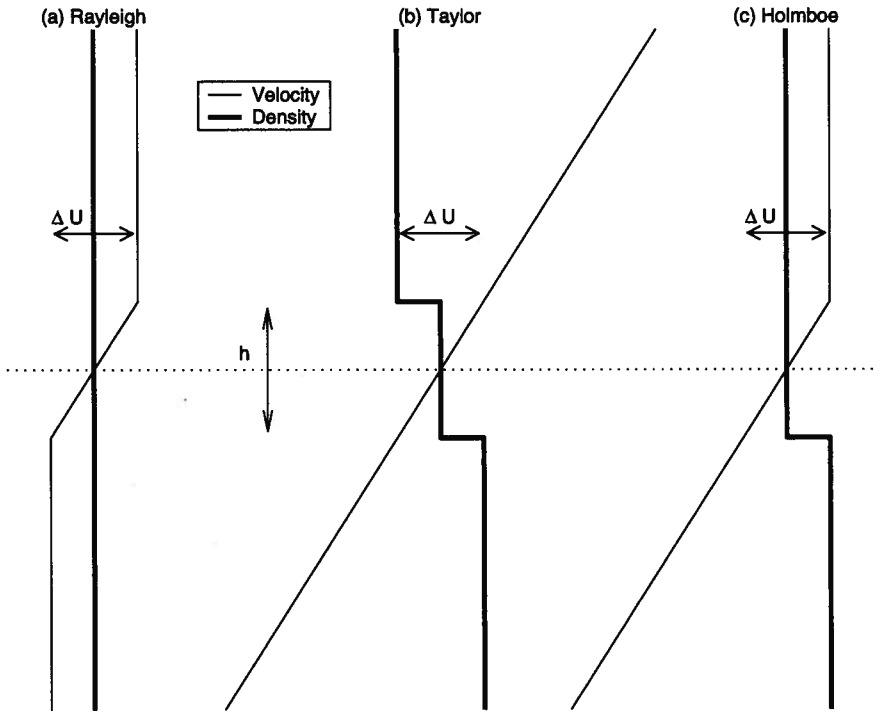

Figure 1.1: Vertical profiles of horizontal velocity and density for the three basic flow cases. In all three cases the velocity is zero at mid-depth (indicated by the dotted line).

sense, i.e. both cases will have the same unstable and stable modes no matter the size of the density step(s) but specific details of the dispersion curves will vary. The inclusion of the density into the non dimensionalization will be discussed further in section 1.1.2. In the cases considered here the length scale associated with the total depth is only important when considering waves at or near the longwave limit.

For all three cases, the dispersion relation was also calculated for each step separately, as if the other step in the profile did not exist and these are shown in figure 1.2 as dashed lines. At shorter wavelengths the modes on each step act in isolation (the solid line equals the dashed line). At greater wavelengths the modes on the different steps interact with the each other (the solid lines diverge from the dashed lines). In each of the three cases it

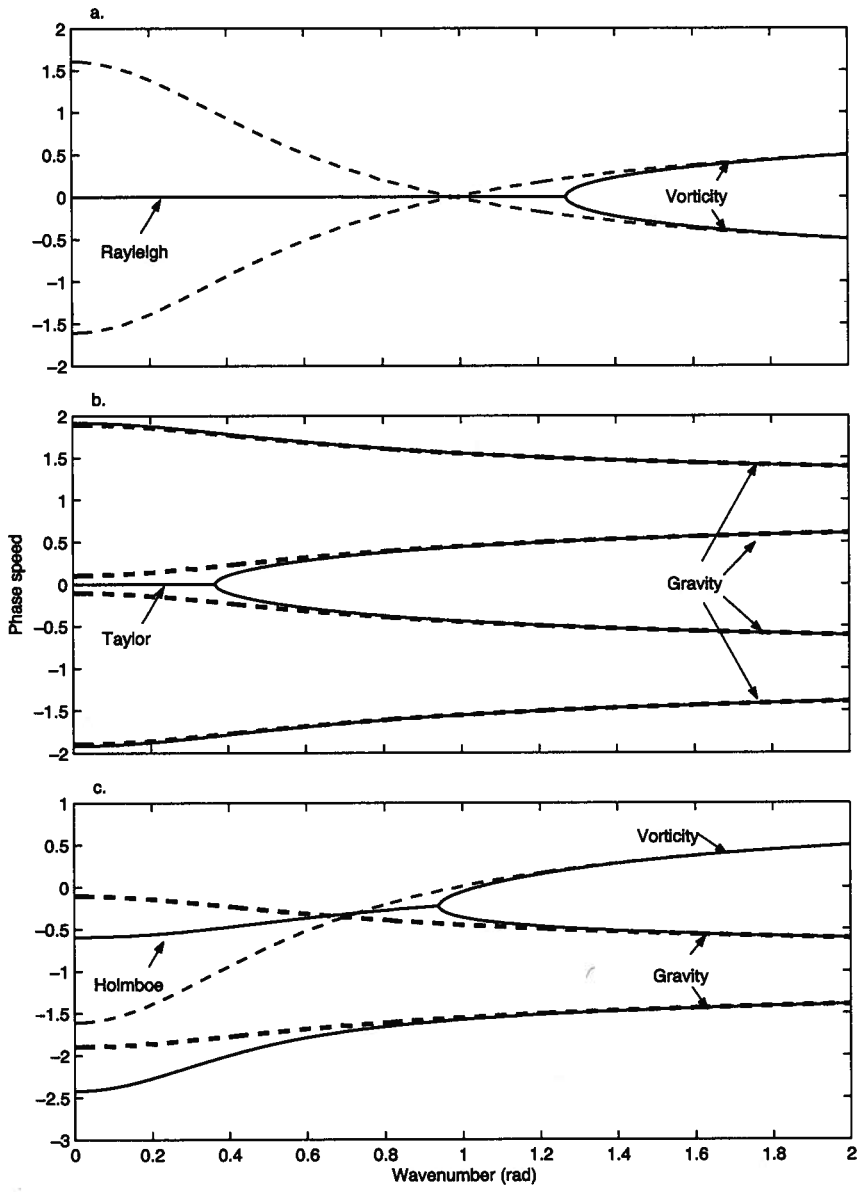

Figure 1.2: Dispersion relations for the three basic flow cases (solid lines). The dashed lines show the modes supported by individual vorticity (thin) and density (heavy) interfaces. The phase speed has been nondimensionalized by the $\Delta U/2$ and the wavenumber by h (see figure 1.1).

is the interaction of the steps (density or vorticity) at longer wavelengths, that causes instability.

Looking first at the Rayleigh [1896] case, at short wavelength there are two stable modes shown by solid lines at high wavenumber in figure 1.2a. These stable modes are associated with the vorticity steps and are referred to as vorticity modes. The mode focussed on the upper vorticity step is propagating to the right (positive c) and the mode focused on the bottom step is propagating to the left. As the wavelength increases (wavenumber, k, decreases) the phase speed of the two stable modes goes to zero. At this wavelength the two stable modes change into two unstable modes. Both unstable modes have the same phase speed ($c = 0$) but one is decaying and the other is growing. The decaying mode is generally ignored. In this example $N^2(z) = 0$ but this need not be the case for the Rayleigh instability mechanism to occur. As long as the stratification is relatively weak the two vorticity steps will interact creating an unstable mode.

In the Taylor case (figure 1.1b and 1.2b) at the shortest wavelengths there are four stable modes [Taylor, 1931]. These modes are simple gravity waves propagating with equal and opposite velocity relative to the velocity at the density step. The two modes propagating to the right lie on the upper density step and the two modes propagating to the left lie on the lower density step. At longer wavelengths, two of the modes, one from each interface, interact and merge into a stationary unstable mode. This unstable mode is referred to as a Taylor instability.

In the Holmboe case (figure 1.1c and 1.2c) at the shortest wavelength there are three stable modes. The mode with the fastest phase speed is propagating to the right and represents a vorticity wave focussed on the upper vorticity step. This mode is identical to the positive vorticity mode in the Rayleigh case (figure 1.2a). The other two stable modes are gravity modes that lie on the lower density step. These two modes are identical to the leftward propagating modes of the Taylor case. As the wavelength increases ($k \downarrow$) the vorticity mode and one of the gravity modes interact and merge into an unstable mode. I will refer to this type of instability as a Holmboe instability. This unstable mode was first examined by Holmboe [1962] although in his analysis there was an additional vorticity step below the density step. The simpler case shown in figure 1.1c was first discussed in Baines & Mitsudera [1994].

In the Rayleigh case $N^2(z) = 0$ and in the Taylor case $d^2U/dz^2 = 0$. The result, in both cases, is that equation 1.1 is greatly simplified. In the case of the Holmboe instability both these terms are non-zero, indeed, it is the interaction of vertical gradients in stratification, $N^2(z)$, and vorticity,

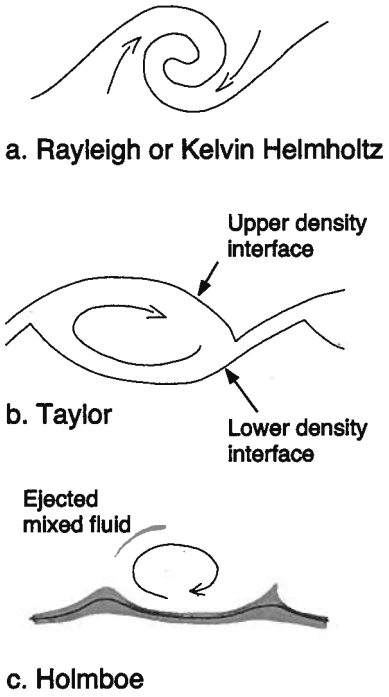

Figure 1.3: Sketches of the three basic instabilities that occur in stratified shear flows: a Rayleigh, b Taylor and c Holmboe. The arrows indicate the primary vortical motion. The sketches are based on DNS and laboratory observations. The gray shading in c indicates fluid of intermediate density.

d^2U/dz^2, that generates the Holmboe instability.

Finite Amplitude Appearance and Mixing

Although the focus of future chapters is on comparing the predicted wave dispersion with observations it should be noted that these three types of instabilities have other differences of practical importance. At finite amplitude the Rayleigh instability has a spiralling billow that resembles the sketch in figure 1.3a. As the instability grows, neighboring billows interact

and combine ('pair') to form a new billow with twice the wavelength and increased amplitude [Browand & Winant, 1973]. In the absence of density stratification pairing will cause the wavelength and amplitude to increase until boundaries are reached. The presence of a density interface centred within the shear layer restricts the pairing and reduces the amplitude of individual billows (they become more elliptical than circular). The amplitude of the billows and the resultant mixing decrease as the strength of the density stratification increases [Thorpe, 1973]. The 2D spiral structure shown in figure 1.3a is most persistent at low Reynolds number. At high Reynolds number the billow breaks down into 3D turbulence before a well defined spiral can form [Brown & Roshko, 1974].

It must be noted that instabilities that occur on a density interface and that are a result of the Rayleigh mechanism described above are invariably referred to as Kelvin-Helmholtz (KH) instabilities rather than Rayleigh instabilities. This potential source of confusion was emphasized in Lawrence *et al.* [1991]. In later chapters these instabilities will also be referred to as KH instabilities rather than Rayleigh instabilities. Strictly speaking the KH instability is the result of coincident steps in both the density and velocity profile [Kelvin, 1871]. The step in velocity, in this case, means the flow is always unstable, no matter the strength of the density stratification. Caulfield [1994] describes all of the unstable modes that result from the interaction of two vorticity interfaces separated by a density interface.

At finite amplitude the Taylor instability (figure 1.3b) has a series of vortices located between the two density interfaces similar to rollers between a conveyer belt (the upper and lower density interfaces). Non-linear simulations of Taylor instabilities suggest they are longer lived and cause much slower mixing than Rayleigh instabilities [Lee & Caulfield, 2001]. Unlike Rayleigh instabilities, their development did not cause complete overturning of the density interface.

The Holmboe instability (figure 1.3c) features cusping waves somewhat resembling surface water waves. At the cusp of the wave mixed fluid accumulates, eventually being ejected as a wisp into the upper layer (or the lower layer if there is a vorticity step below the density step). Like the Taylor instability the Holmboe instability does not cause complete overturning of the density interface [Carpenter *et al.*, 2007]. In direct numerical simulations, Smyth & Winters [2003] found that although Holmboe instabilities grow more slowly than Rayleigh (KH) instabilities the total amount of mixing may be comparable.

It is worth noting that some authors [e.g. Koop, 1976] refer to any instability that occurs in stably stratified shear flow as a KH instability.

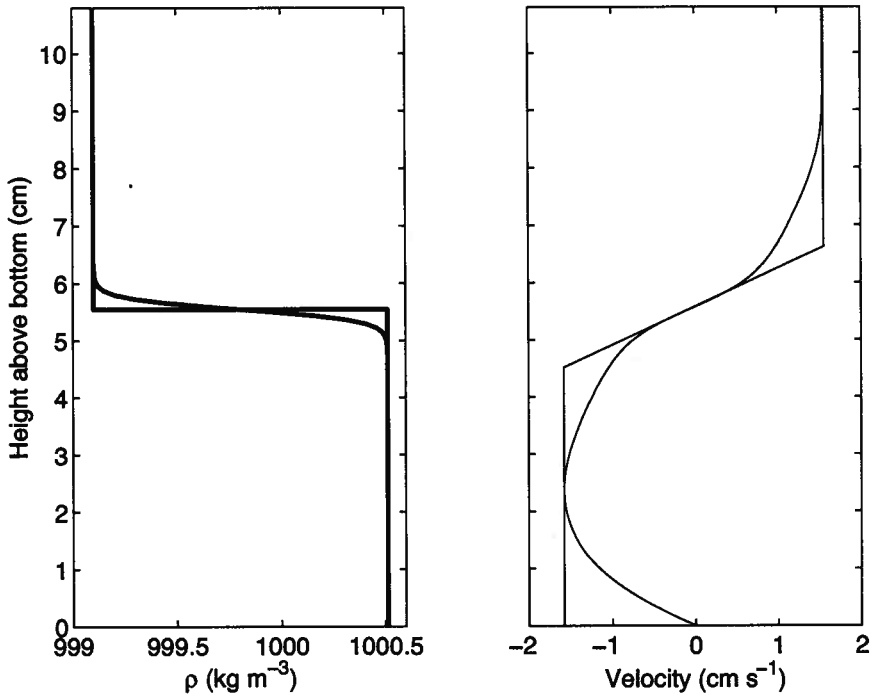

Figure 1.4: Smooth profiles observed in the lab with a piecewise linear fit matching the symmetric Holmboe case.

1.1.2 Symmetric Holmboe Instability

The piecewise linear profiles shown in figure 1.4 were originally analyzed by Smyth [1986]. They represent a bounded version of the flow configuration considered by Holmboe [1962]. In this chapter I will refer to this case as the symmetric Holmboe case. In later chapters, and in the literature in general, it is referred to simply as the Holmboe case. The sharp density interface positioned within a uniform shear layer approximates conditions observed in salt stratified shear flows at laboratory scales (the smooth profiles are from the experiments discussed in chapter 2). This case will support a single Rayleigh instability or two Holmboe instabilities depending on the strength of the shear compared to the strength of the stratification.

In this case the strength of the stratification is characterized with the reduced gravity: $g' = g\Delta\rho/\rho_0$, where ρ_0 is the average density and $\Delta\rho$ is the

density difference between the layers. The bulk stability is then given by the Richardson number, $J = g'h/(\Delta U)^2$, ΔU is the total shear and h is the shear layer thickness. To obtain a representative value of h the piecewise linear velocity profile is fit to the maximum layer velocities (see figure 1.4).

In figure 1.5 the regions where Holmboe and Rayleigh instability will occur is mapped in Richardson number - wave number space. The stability bounds shown are determined by calculating the dispersion relation for a range of J values. For weak stratification ($J < 0.07$) the Rayleigh instability will occur and at higher Richardson number only the Holmboe instability will occur. In the laboratory flow considered in chapters 2 and 4 the bulk Richardson number is 0.3 (the horizontal line in figure 1.5), well above the upper limit for a Rayleigh instability. The dispersion relation for the two Holmboe modes at this value of J is plotted in figure 1.6. It is very similar to the dispersion relation for the Holmboe case (figure 1.2c). At short wavelengths there is an additional (stable) vorticity mode associated with the second, lower, vorticity step (not shown in figure 1.6). At longer wavelengths this additional vorticity mode merges with the leftward propagating gravity mode to form a second Holmboe instability. This second Holmboe mode propagates in the opposite direction (negative phase velocity) and has a nearly identical growth rate (figure 1.6b).

1.1.3 Asymmetry and One-sidedness

If the density interface shown in figure 1.4 is not centred within the shear layer, e.g. if the density interface is closer to one vorticity interface than the other, then the growth rates and dispersion relations of the two Holmboe modes will differ. For example, in the splitter plate experiments of Lawrence *et al.* [1991], the density interface was positioned closer to the lower vorticity interface than to the upper vorticity interface. This asymmetry in the profiles resulted in the upper Holmboe mode having a greater growth rate than the lower Holmboe mode. The more unstable mode tended to dominate such that at finite amplitude the instability resembled the Holmboe instability sketched in figure 1.3. These asymmetric instabilities are typically referred to as 'one-sided'. Because the density and velocity profiles that occur in nature often include some asymmetry one-sided instabilities are common (see chapter 3).

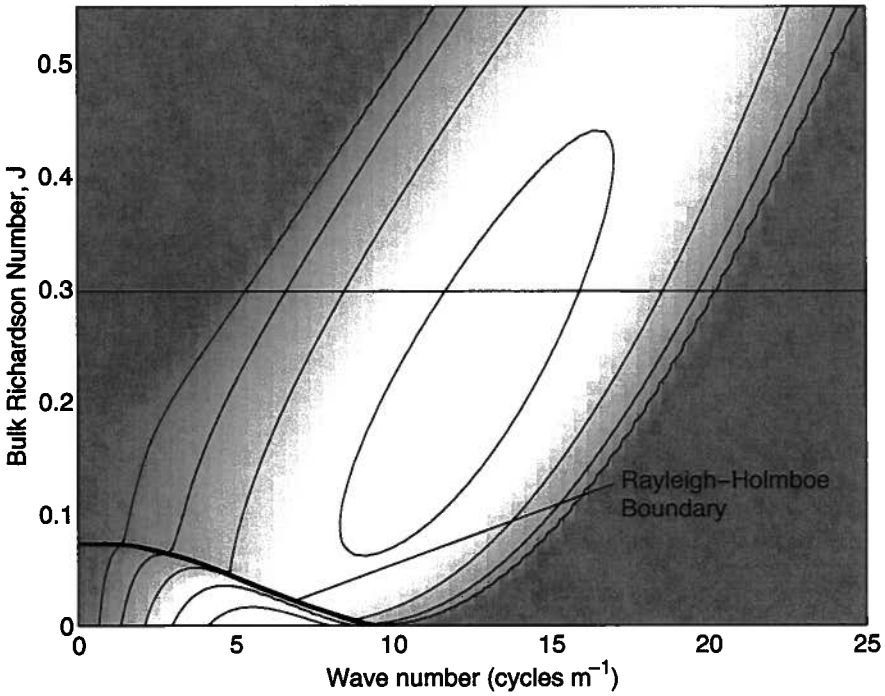

Figure 1.5: Stability diagram for the symmetric Holmboe case with the total depth, $H \approx 5h$. The growth rate of unstable modes is contoured and shaded. The regions with the darkest shade of gray are stable. The horizontal line indicates the value of J of interest.

1.1.4 Smooth Profiles

Before discussing solutions to the TG equation based on smooth profiles, the relationship between piecewise linear and smooth profiles, especially for the Holmboe profiles, should be emphasized. In the piecewise linear profiles, unstable modes resulted from the interaction of a step in the density profile and a kink in the velocity profile. Similarily, in smooth profiles, unstable modes result from the interaction of a maximum in the vertical gradient of ρ (N^2 in the TG equation) and a maximum in the curvature of the velocity profile (d^2U/dz^2 in the TG equation).

Velocity and density profiles measured in the lab (see chapter 3) are plotted in figure 1.4. Using the method outlined in Moum *et al.* [2003] the dispersion relation for this set of profiles was calculated. The method

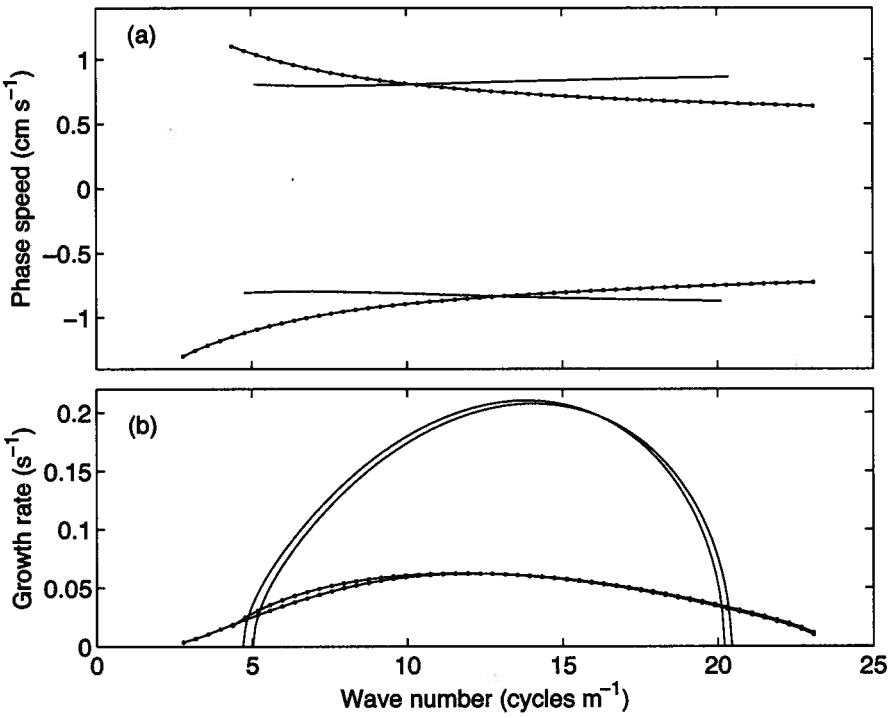

Figure 1.6: Phase speed (a) and growth rate (b) for the symmetric Holmboe case (solid line) and smooth profiles observed in the lab (dotted solid line). The small differences between the leftward and rightward propagating modes are due to slight asymmetry in both the observed and fit profiles.

includes the effect of viscosity. The viscosity plays a secondary role in the flows considered here in that it tends to slightly stabilize short waves. In the case shown in figure 1.6 the velocity and density profiles have been measured at a fine enough vertical resolution such that on the scale of the entire depth they appear smooth. On the scale of the vertical resolution they will have steps in the density and vorticity just as the piecewise linear profiles did. As in the piecewise linear cases each of these small steps will support two gravity modes and one vorticity mode. Most of these modes are due only to the details of the resolution or discretization. Following Moum *et al.* [2003], these spurious modes are rejected using a kinetic energy criteria.

For the smooth set of profiles shown in figure 1.4 there are two Holmboe

modes (i.e. unstable modes) with similar phase speeds to those that occur for the piecewise linear fit. The dispersion relations for the smooth and piecewise linear profiles are plotted together in figure 1.6a. The phase speed for the smooth profiles shows more variation over k with long waves propagating more quickly than in the piecewise linear case and shorter waves propagating more slowly. The growth rates (the imaginary part of c) are similar in that the peak occurs at approximately the same wave number (k =15 cycles m^{-1} for the smooth and k =14 cycles m^{-1} for the piecewise linear). The magnitude of the growth rate is considerably less for the smooth profiles. This difference is primarily due to the greater thickness of the density interface in the case of the smooth profiles (i.e. finite rather than a step). For a description of the dependence of growth rate on density interface thickness see Smyth & Winters [2003] and Haigh [1995].

1.1.5 Eigenfunctions

So far I have discussed only the eigenvalue, c, and not the associated eigenfunction $\hat{\psi}$. Two quantities derived from $\hat{\psi}$ are particularly useful, the displacement function $\hat{n(z)} = w(z)/(U-c)$ and the shear production uw. By the definition of the streamfunction the vertical velocity of the perturbation, $w(z)$, is equal to $\hat{\psi}$ multiplied by an arbitrary constant and phase shift. The horizontal velocity of the perturbation, $u(z)$, is equal to $\frac{dw}{dz}/k$. The displacement function shows where in the vertical we can expect to see the largest vertical deflections e.g. where isopycnals will show the greatest vertical movement. The shear production shows where in the vertical kinetic energy is transferred from the mean flow to the instability. Figure 1.7a and c show that the displacement and shear production have a maximum amplitude just above the elevation of the density interface (the dotted line in figure 1.7). It is in this region, between the maximum curvature in the velocity profile, d^2U/dz^2, and the maximum gradient in the density, N^2, that the interaction between the vorticity and stratification is strongest. In figure 1.7b the phase of the displacement function is also plotted.

To aid in the interpretation of the displacement function it is plotted in an alternative form in figure 1.8. The figure shows sinusoidal waves with relative amplitudes and phases matching the displacement function. These sinusoids can be thought of as dye streaks. The reader should be reminded the TG equation is for infinitesimal waves, so the waves in figure 1.8 have been given finite amplitude for illustrative purposes. Hazel [1972] used a similar diagram for illustrating various shear instabilities.

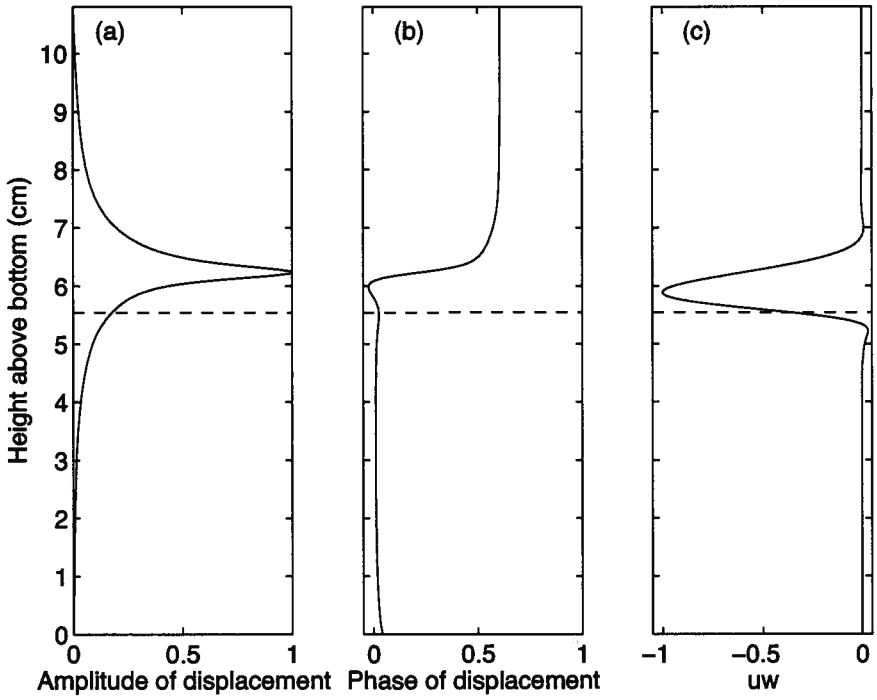

Figure 1.7: Eigenfunction derived quantities for the rightward propagating Holmboe mode at the wave number of maximum growth. The phase is in $radians/\pi$. The eigenfunctions were calculated using the smooth profiles in figure 1.4. The dash line indicates the height of the density interface.

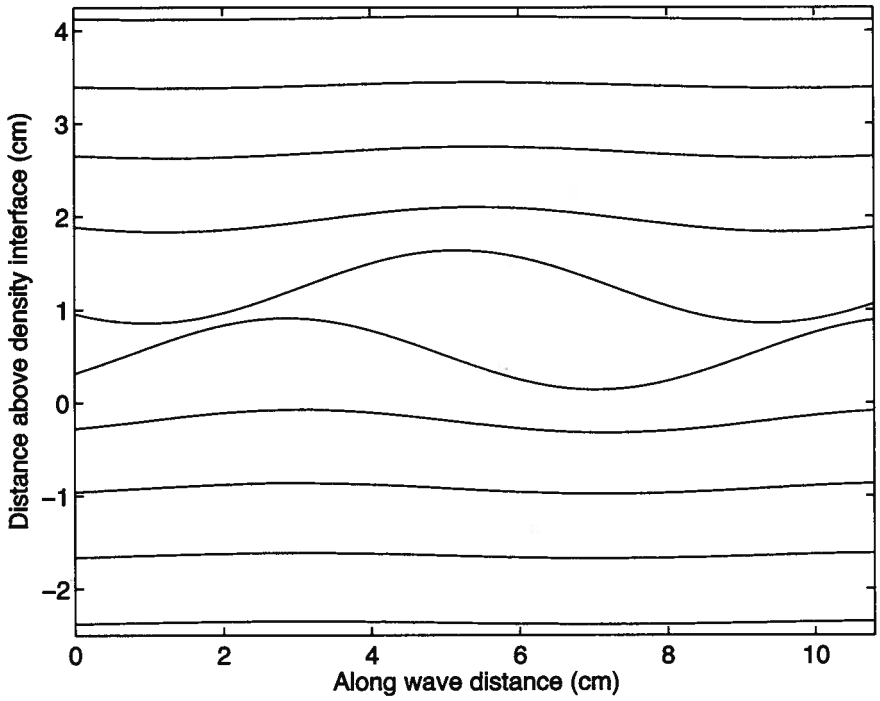

Figure 1.8: Displacement of dye lines for the rightward propagating Holmboe mode at the wave number of maximum growth.

Bibliography

BAINES, P.G. & MITSUDERA, H. 1994 On the mechanism of shear flow instabilities. *J. Fluid Mech.* **276**, 327–342.

BROWAND, F.K. & WINANT, C.D. 1973 Laboratory observations of shear-layer instability in a stratified fluid. *Boundary-Layer Met.* **5**, 67–77.

BROWN, F.L. & ROSHKO, A. 1974 On the density effects and large structure in turbulent mixing layers. *J. Fluid Mech.* **64**, 775–816.

CARPENTER, J.R., LAWRENCE, G.A. & SMYTH, W.D. 2007 Evolution and mixing of asymmetric Holmboe instabilities. *J. Fluid Mech.* **582**, 103–132.

CAULFIELD, C.P. 1994 Multiple linear instability of layered stratified shear flow. *J. Fluid Mech.* **258**, 255–285.

DRAZIN, P.G. & REID, W.H. 1982 *Hydrodynamic Stability*, first paperback edn. Cambridge University Press.

GEYER, W.R. & FARMER, D.M. 1989 Tide-induced variation of the dynamics of a salt wedge estuary. *J. Phys. Oceanogr.* **19**, 1060–1672.

GOLDSTEIN, S. 1931 On the stability of superposed streams of fluids of different densities. *Proc. R. Soc. Lond. A* **132**, 524–548.

HAIGH, S.P. 1995 Non-symmetric Holmboe waves. PhD thesis, University of British Columbia.

HAZEL, P. 1972 Numerical studies of the stability of inviscid stratified shear flows. *J. Fluid Mech.* **51**, 39–61.

HOLMBOE, J. 1962 On the behavior of symmetric waves in stratified shear layers. *Geofys. Publ.* **24**, 67–112.

KELVIN, W. 1871 Hydrokinetic solutions and observations. *Philos. Mag.* **42**, 362–377.

KOOP, C.G. 1976 *Instability and turbulence in a stratified shear layer*. Department of Aerospace Engineering, University of Southern California.

LAWRENCE, G.A., BROWAND, F.K. & REDEKOPP, L.G. 1991 The stability of a sheared density interface. *Phys. Fluids* **3** (10), 2360–2370.

LEE, V. & CAULFIELD, C.P. 2001 Nonlinear evolution of a layered stratified shear flow. *Dyn. Atmos. Oceans* **24**, 173–182.

MOUM, J.N., FARMER, D.M., SMYTH, W.D., ARMI, L. & VAGLE, S. 2003 Structure and generation of turbulence at interfaces strained by internal solitary waves propagating shoreward over the continental shelf. *J. Phys. Oceanogr.* **33**, 2093–2112.

RAYLEIGH, J.W.S. 1896 *Theory of Sound*, 2nd edn. Macmillan.

SMYTH, W.D. 1986 *M.Sc. thesis*. Department of Physics, University of Toronto.

SMYTH, W.D. & WINTERS, K.B. 2003 Turbulence and mixing in Holmboe waves. *J. Phys. Oceanogr.* **33**, 694–711.

TAYLOR, G.I. 1931 Effect of variation in density on the stability of superposed streams of fluid. *Proc. R. Soc. Lond. A* **132**, 499–523.

THORPE, S.A. 1973 Experiments on instability and turbulence in a stratified shear flow. *J. Fluid Mech.* **61**, 731–751.

ZHU, D. & LAWRENCE, G.A. 2001 Holmboe's instability in exchange flows. *J. Fluid Mech.* **429**, 391–409.

Chapter 2

Symmetric Holmboe Instabilities in a Laboratory Exchange Flow [1]

2.1 Introduction

Flows in the environment often consist of well defined layers of different density. A density difference can result from salinity (e.g. in an estuary or the ocean), temperature (e.g. in a lake), sediment (e.g. gravity current) or other factors. Studies of geophysical flows have shown that wavelike features occur at the interface between sheared layers [Wesson & Gregg, 1994; Geyer & Smith, 1987; Tedford *et al.*, 2007]. As these interfacial features or instabilities grow, fluid is exchanged vertically between the layers. Mixing between layers is important because it controls the vertical transfer of salt, heat, nutrients, pollutants and momentum.

Stratified shear flows in the laboratory also exhibit a variety of wave-like features. The most well known are the Kelvin-Helmholtz (KH) instabilities observed in the classic experiments of Thorpe [1971]. The shear between two homogeneous layers of differing salinity causes instabilities that are exceptionally uniform in wavelength and amplitude. These instabilities quickly grow into stationary billows which, in turn, break down into three dimensional turbulence. Of the shear instabilities that occur in stratified flows, the KH instability has been studied most extensively, but in recent years increasing attention has been paid to the Holmboe instability.

Holmboe [1962] analyzed the stability of a sharp density interface subjected to shear. He predicted that when stratification is strong enough to suppress the KH instability, two wave trains develop that travel with equal and opposite phase speeds with respect to the mean flow. An example of

[1] This chapter has been accepted for publication subject to revision in: E. W. Tedford, R. Pieters and G.A. Lawrence (2009), Symmetric Holmboe Instabilities in a Laboratory Exchange Flow, *J. Fluid Mech.*

Holmboe's instability from the present experiments is shown in figure 2.1. The potential importance of Holmboe instabilities was recently highlighted by the direct numerical simulations of Smyth & Winters [2003], who found that, although Holmboe instabilities grow less rapidly than KH instabilities, the total amount of mixing can be greater [see also Smyth, 2006; Smyth *et al.*, 2007; Carpenter *et al.*, 2007]. Note that while Holmboe [1962] assumed a density step, Alexakis [2005] has shown that Holmboe instabilities can occur providing the thickness of the velocity interface is more than double the thickness of the density interface. Holmboe instabilities are thought to occur in natural flows such as the exchange flow through the Strait of Gibraltar [Farmer & Armi, 1998] and the salinity intrusion in a strongly stratified estuary [Yoshida *et al.*, 1998].

Several techniques have been used to study Holmboe instabilities in the laboratory. In the splitter plate experiments of Koop & Browand [1979] and Lawrence *et al.* [1991] only one of the two modes predicted by Holmboe appeared. A series of cusps from which wisps of interfacial fluid were occasionally ejected formed on only one side of the interface. This 'one-sidedness' was a result of a vertical displacement between the sharp density interface and the shear, an inherent condition in splitter plate experiments. While Carpenter *et al.* [2007] have postulated that one-sided instabilities may be an important source of mixing, we will restrict our attention to symmetric (two-sided) instabilities in the present study.

Using immiscible fluids and varying viscosity, Pouliquen *et al.* [1994] conducted tilting tube experiments to generate Holmboe instabilities. Due to the slow growth of the instabilities and the inherently short duration of tilting tube experiments they were only able to observe the early onset of instabilities and, unlike Thorpe [1971], they were required to use regularly spaced obstacles to force uniformity.

The one-sidedness of splitter plate experiments, and the short duration of tilting tube experiments, can be avoided by using exchange flow. Zhu & Lawrence [2001] studied Holmboe instabilities in exchange flow through a channel of uniform width with a sill. However, symmetric Holmboe instabilities were only a transient feature of these experiments. Hogg & Ivey [2003] studied exchange flow through a contraction. However, this contraction was relatively short so that only a small number of instabilities were present at any given time, and the background flow conditions changed over a single wavelength. In the present study we use a long channel of rectangular cross-section in which many waves are present at any given time.

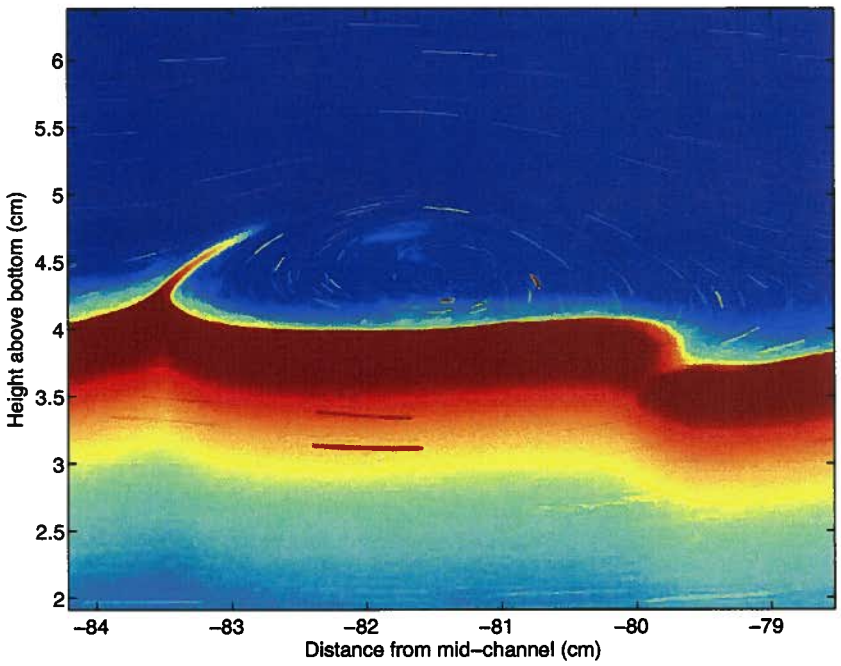

Figure 2.1: Close up image of the interface between two layers. The top, fresh layer is moving to the right and the bottom, saline layer is moving to the left. The upward pointing cusp is a positive, rightward propagating Holmboe instability and the downward pointing cusp is a negative, leftward propagating Holmboe instability. Colour varies from blue to red marking high to low fluorescence of dye. The decrease in fluorescence below the interface is caused by the dissipation of light. To generate particle streaks the shutter speed of the camera was set to 0.5 seconds.

The goals of this study are to carry out experiments in the laboratory that generate Holmboe instabilities and to compare the properties of these instabilities with the predictions of Holmboe [1962]. In the next section, the linear model of Holmboe [1962] is described. Section 3 describes the laboratory setup and methods. In section 4, the evolution of the mean flow and the observed wave characteristics are described. In section 5, the observations are compared with the linear predictions.

2.2 Background Theory

2.2.1 Hydraulics of Exchange Flow

The basic features of exchange flow can be described by two-layer hydraulics [Armi, 1986]. Here we briefly review the concept of internal hydraulic controls and their relevance to the instabilities. In single-layer flows the concept of 'hydraulic control' is used to determine how flow rate relates to channel geometry. A single layer control can occur where the flow exits a restriction, such as a horizontal expansion or an increase in bed slope. At the control the flow speed is equal to the long wave speed and is therefore said to be critical. In subcritical flow, waves may propagate in both directions, upstream or downstream. In supercritical flow waves can only propagate in one direction, downstream. At the control there is a transition from subcritical to supercritical flow.

Two-layer flows also exhibit hydraulic controls, but their occurrence is complicated by factors such as flow in both directions, channel geometry influencing each layer differently, shear influencing the long wave speed and mixing between the layers. Although waves can form on both the free surface and on the interface between the layers, here we are solely concerned with interfacial (internal) waves and instabilities. Similar to single layer flows an internal control occurs at a transition from subcritical to supercritical flow. In subcritical flow, internal waves, including instabilities, may propagate in both directions. In supercritical flow they can propagate in only one direction. In the present study we focus on maximal exchange flows, which are characterized by a control at each end of the channel [Gu & Lawrence, 2005]. The flow is subcritical within the channel and supercritical outside of it. In the supercritical regions just outside of the channel, waves can only propagate away from the channel, i.e. waves from the reservoirs cannot enter the channel.

2.2.2 Dispersion Relation and Instability

To investigate the dynamics of instabilities, Holmboe [1962] analyzed the piecewise linear velocity and density profiles shown in figure 2.2. The sharp density interface within a uniform shear layer approximates conditions observed in salt stratified shear flows at laboratory scales; sample profiles from the present experiments are shown in figure 2.2. Holmboe's analysis assumes the density interface is centred within the shear layer and does not account for the influence of the boundaries. The key parameters in the stability analysis are the velocity difference between the layers, $\Delta U = U_1 - U_2$, the

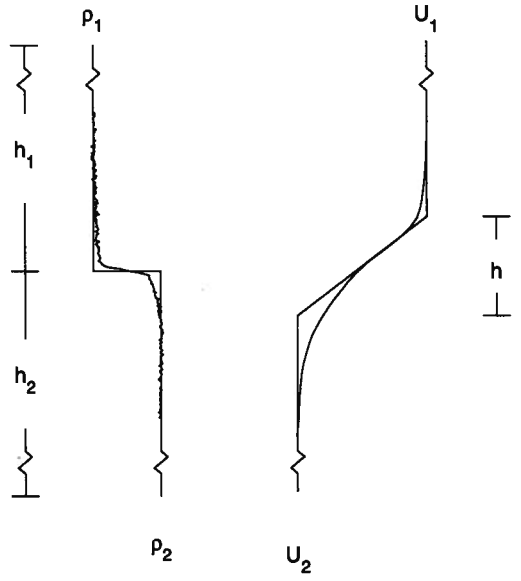

Figure 2.2: Definition sketch for piecewise linear profiles used in the analysis of Holmboe instabilities. Also shown are sample density and velocity profiles from the current study.

shear layer thickness, $h = \Delta U/(dU/dz)_{max}$ and the reduced gravitational acceleration, $g' = g\Delta\rho/\rho_0$ (where $\Delta\rho$ is the density difference and ρ_0 is the average density). The subscripts 1 and 2 indicate the upper and lower layer, respectively. To characterize the total shear across the interface, U_1 and U_2 are defined as the maximum or free stream velocity in each layer.

The shear and stratification parameters are combined to form the bulk Richardson number, $J = g'h/\Delta U^2$. Following Holmboe's analysis, Lawrence *et al.* [1991] used the Taylor-Goldstein (TG) equation to relate the complex phase speed ($c = c_r + ic_i$) to wave number (α) and J:

$$c^2 = \frac{-a_1 \pm \sqrt{a_1^2 - 4a_2}}{2} \tag{2.1}$$

where

$$a_1 = \beta_+\beta_- - n^2, \quad a_2 = n^2\beta_-^2, \quad \beta_\pm = [e^{-\alpha} \pm (1-\alpha)]/\alpha, \quad n^2 = 2J/\alpha$$

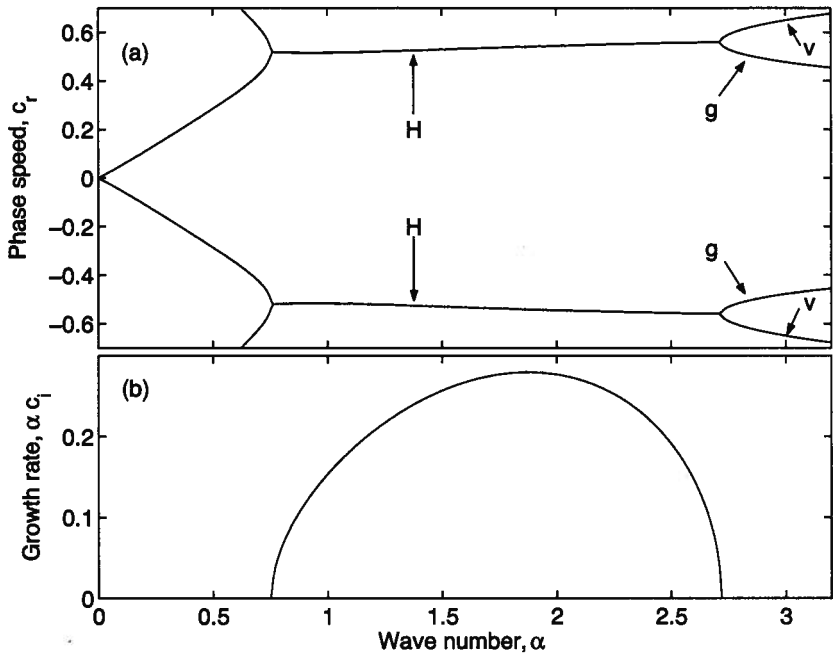

Figure 2.3: (a) Dispersion relation for the Holmboe flow configuration at $J = 0.3$. The labels H, v, and g indicate line segments associated with Holmboe (unstable), vorticity, and gravity modes respectively. (b) Exponential growth rate (αc_i) of the Holmboe mode. The wavenumber of maximum growth ($\alpha = 1.9$) corresponds to a dimensional wavelength $\lambda \approx 7$ cm for the present experiments. The phase speed is shown nondimensionalized by $\Delta U/2$; the wave number is nondimensionalized by the shear layer thickness, h; and the growth rate is nondimensionalized by $2h/\Delta U$.

For brevity, all of the terms in (2.1) are non-dimensional and the phase speed is relative to the mean of the free stream velocities, $\bar{U} = (U_1 + U_2)/2$. The dimensional phase speed $c^* = c\ \Delta U/2 + \bar{U}$ and the dimensional wavelength $\lambda = 2\pi h/\alpha$.

The dispersion relation (2.1) is plotted in figure 2.3 for $J = 0.3$ corresponding to conditions in our laboratory experiments (Table 2.1). At high wavenumber the flow supports two stable gravity modes and two stable vorticity modes (so called because wave propagation is governed by buoyancy in the first instance and by the vorticity gradient in the second). The

H (cm)	L (cm)	W (cm)	g' (cm s^{-2})	h (cm)	ΔU (cm s^{-1})	J
10.8	200	10	1.39	2.1	3.1	0.3

Table 2.1: Experimental parameters.

rightward propagating vorticity mode is associated with the upper vorticity interface (upper kink in the velocity profile) and the leftward propagating vorticity mode is associated with the lower vorticity interface. As wavenumber decreases the vorticity mode and gravity mode propagating in the same direction merge into one unstable mode ($\alpha \approx 2.6$). At lower wavenumber ($\alpha \lesssim 0.7$) the dispersion relation bifurcates back to four stable modes. Unlike the Kelvin-Helmholtz instability, the unstable mode particular to the Holmboe configuration is non-stationary.

When $J = 0.3$ the maximum growth rate of the Holmboe instability, $\alpha c_i = 0.28$, occurs at $\alpha = 1.9$ (figure 2.3b) with a corresponding phase speed $c_r = \pm 0.53$. Dimensionalizing by $h = 2.1$ cm and $\Delta U/2 = 1.56$ cm s^{-1}, as observed in our experiments, yields a maximum growth rate at a wavenumber $k = 2\pi/\lambda = 0.9$ cm^{-1} ($\lambda = 7$ cm) and a phase speed of $c_r^* = \bar{U} \pm 0.83$ cm s^{-1}. The dimensional growth rate $kc_i = 0.2$ s^{-1} results in a doubling time of 3.5 s. In the following sections we will compare the observed wave characteristics with predictions from (2.1), particularly at the wavenumber of maximum growth.

2.3 Experimental Setup

A schematic of the laboratory setup is shown in figure 2.4. The overall tank was 370 cm long, 106 cm wide and 30 cm deep as in Zhu & Lawrence [2001]. The tank was divided into two equally sized reservoirs and connected by a channel 10 cm wide and 200 cm long. The water was well mixed between the reservoirs to ensure uniform temperature ($\approx 20°C$) throughout the tank. A removable gate was placed in the middle of the channel isolating the left and right side. Salt was mixed into the right reservoir to provide a density difference of 1.41 kg m^{-3} (g' of 1.39 cm s^{-2}). The basic experimental parameters are provided in Table 2.1.

The experiments differ from those of Zhu & Lawrence [2001] in that the water depth was kept relatively shallow (H=10.8 cm) and there was no sill in the channel (flat bottom). These changes resulted in more gradual horizontal variations in U and J, and therefore more uniform wave properties.

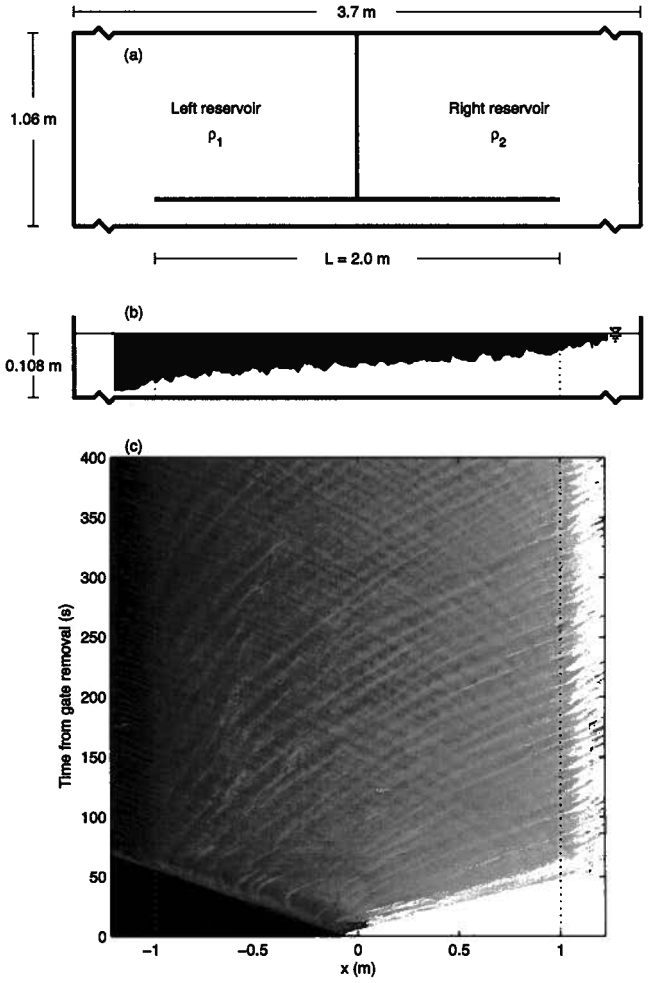

Figure 2.4: (a) Plan and (b) side view of the experimental setup and (c) wave characteristics plot. The left and right reservoirs initially contain fresh and saline water respectively. The side view (b) includes a sample image of the interface over the entire length of the channel plus a portion of each reservoir at $t = 400$ s. The lower layer contains dye and is illuminated from above with a laser generated light sheet. The characteristics (c) represent a compilation of interface heights observed in several thousand images. The shading is scaled such that black indicates the interface is near the bottom of the channel and white indicates the interface is near the free surface. Diagonal light and dark streaks represent interfacial waves.

Experiment	Measurement	Location	Replicates	Parameter
1-7	LIF	$-0.9 < x < 0.9$	7	h_2
8-12	PIV	$x = 0$	5	h, U_1, U_2
13	LIF	$-1.2 < x < 1.2$	1	h_2
14	PIV and LIF	$x = 0$	1	h, U_1, U_2
15	Particle streak	$x = -0.8$	1	-
16	Bottle samples	$x = -1, 0, 1$	1	g'

Table 2.2: Summary of laboratory experiments.

In addition, the shallower depth resulted in a prolonged period of maximal exchange. Experiments using yet shallower depths or smaller density differences were attempted, but resulted in the suppression of instabilities (presumably due to viscous effects). Larger density differences were also used, but were subject to a number of problems including shortened experiment duration, large changes in the index of refraction at the density interface and diminished image quality (due to the higher shutter speeds required to capture faster waves). To gather the data used in this study the experiment was repeated 16 times with depth and $\Delta\rho$ held constant (see Table 2.2).

Laser induced fluorescence (LIF) was used to visualize the density interface by illuminating fluorescein dye in the lower layer with a continuous 4 watt argon ion laser. The laser beam was passed through a Powell lens to generate a downward radiating light sheet along the centre of the channel. Images were collected using a digital camera; a sample image is shown in figure 2.4 b. The interface was identified by locating the maximum vertical gradient in light intensity.

A Dantec particle image velocimetry (PIV) system was used to measure the velocity of pliolite VT-L particles (Goodyear Chemical Co.). The particles were pulverized and sieved to diameters less than 0.24 mm. Although some particles did settle out there was sufficient quantity to perform PIV throughout the duration of the experiment. Pairs of images ($\Delta t = 0.04$s) were collected every 3 seconds. A 3-step adaptive correlation algorithm was used to calculate velocities. The final interrogation areas were 32 pixels wide by 16 pixels high (2.8 mm x 1.4 mm) with a 50 % overlap resulting in a 0.7 mm vertical spacing of vectors. The total image size was 11 cm wide by 9 cm high. Small scratches on the acrylic wall limited PIV to a single location ($x = 0$). The Dantec system was also used to determine density by quantitative measurement of dye fluorescence.

In experiment 13, LIF was performed over the entire viewable region of the tank ($-1.2\text{m} < x < 1.2\text{m}$). This experiment allowed us to include the critical and supercritical regions of the flow in our qualitative description of the wave characteristics. In experiment 14 both PIV and LIF were performed simultaneously to confirm that the density interface was much thinner than the shear layer (figure 2.2). Particle streak images (figure 2.1) were collected in experiment 15 to examine the structure of individual instabilities. Finally, fluid samples were collected with a syringe and analyzed in a densitometer to verify $\Delta\rho$ between the layers.

2.4 Evolution of Mean Flow

The experiment begins when the gate separating the fresh and salt water at the centre of the channel is removed. Two gravity currents immediately form and propagate in opposite directions; these gravity currents exit the channel at $t \approx 60$ s (figure 2.4c). The gravity currents generate mixed fluid which is gradually flushed out of the channel leaving two uniform layers separated by an interface approximately 2 mm thick ($t = 200$ s). In addition, a Helmholtz oscillation [Miles & Munk, 1961] is generated when the gate is removed and remains noticeable in velocity measurements until $t \approx 400$ s (figure 2.5) . This oscillation has a period of 28 s and is reflected in the measured phase speed of the instabilities.

Once the Helmholtz oscillations dampen out ($t = 300$ to 400s), the flow enters a long period of relatively steady maximal exchange, which ends when the control at the right end of the channel is flooded and the flow becomes subcritical in the right reservoir. After the control is lost, disturbances can enter the channel from the reservoir (not visible in figure 2.5). In the present study we focus on instabilities generated within the channel during the long period of maximal exchange when conditions are steady ($400\text{ s} < t < 800\text{s}$). During this period interfacial wave properties remain relatively constant.

For the steady period the mean interface height shows a gradual slope (≈ 0.02) throughout most of the channel (figure 2.6a); a steeper slope occurs at the ends of the channel consistent with the presence of controls. The observed interface height compares well with the analytical predictions of Gu & Lawrence [2005] using their $\alpha = 0.41$ and $r = 1$. The time averaged velocity profile observed at $x = 0$ is shown in figure 2.6a. At this point the average flow speed in each layer is 1.1 cm s^{-1}. This is just over half the flow speed predicted by the inviscid two-layer theory ($\sqrt{g'H}/2$ =1.9 cm s^{-1}).

The observed velocity profile can be approximated by a piecewise linear

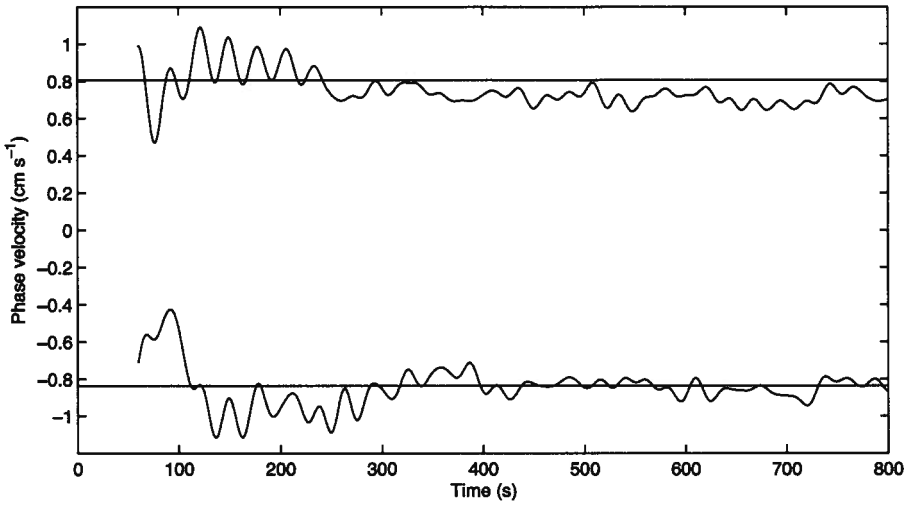

Figure 2.5: Phase velocity of rightward (positive) and leftward (negative) propagating waves at $x = 0$. The phase velocities were calculated using the cross correlation of the interface between successive images. A low pass filter (removing periods < 20 s) was applied to remove variability due to individual waves. The horizontal lines are the phase speeds predicted using the linear theory.

fit with free-stream (maximum) velocities in the upper and lower layers of $U_{1c} = 1.55$ cm s^{-1} and $U_{2c} = -1.57$ cm s^{-1}, respectively. The subscript c denotes the centre of the channel ($x = 0$). Because of the bottom boundary layer the lower layer has a slightly greater maximum velocity than the upper layer resulting in $\bar{U}_c \approx$ -0.01 cm s^{-1}. The velocity profile has a shear layer thickness $h = 2.1$ cm.

To understand the evolution of the waves discussed in the next section it is useful to estimate the mean, $\bar{U}(x) = \frac{U_1(x)+U_2(x)}{2}$, along the entire length of the channel. We assume that $U_1(x)$ and $U_2(x)$ can be estimated from the velocities observed at the centre of the channel using: $U_i(x) = U_{ic}y_{ic}/y_i(x)$, where the layer thicknesses, y_i, are based on the observed interface height (figure 2.6a). The resulting velocity estimates are plotted in figure 2.6b and will be used below to describe the evolution of the waves.

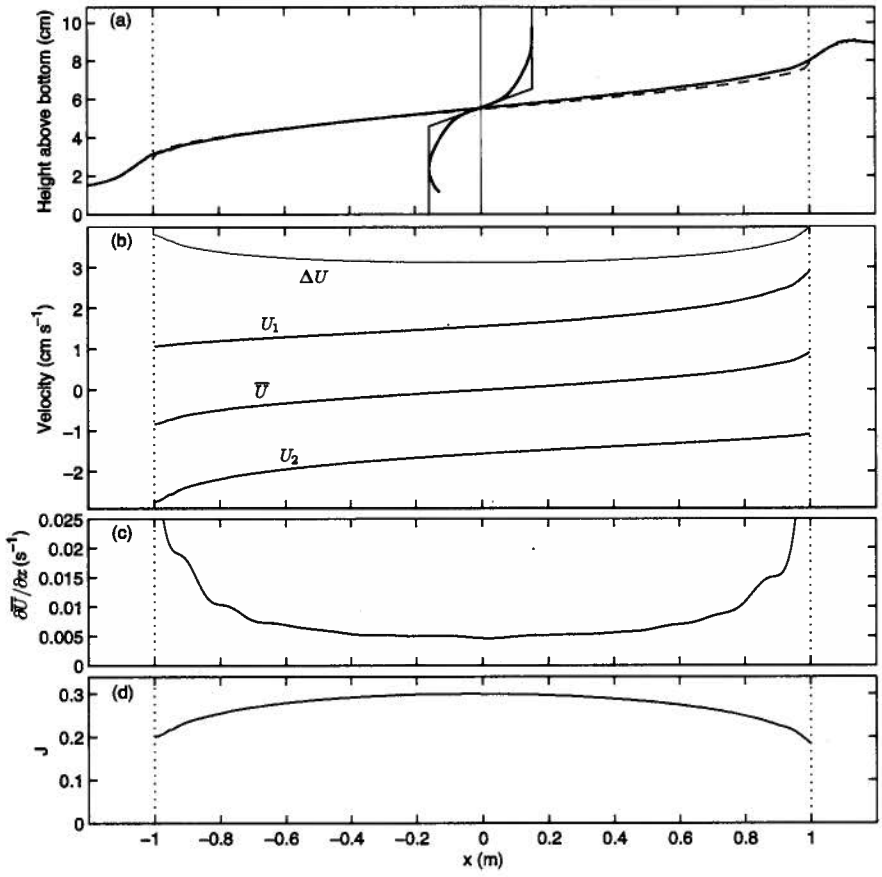

Figure 2.6: (a) Mean interface height along the channel during the period of steady exchange. The interface height predicted by two layer hydraulics (see text) is shown as a dashed line. Also shown is the average velocity profile observed at $x = 0$ and the piecewise linear profile used in the stability analysis. The maximum speeds in the upper and lower layers at $x = 0$ are $U_1 = 1.55$ cm s^{-1} and $U_2 = -1.57$ cm s^{-1} respectively. (b) Estimates of the free stream (maximum) velocities, $U_1(x)$ and $U_2(x)$, the total shear, $\Delta U(x)$, and the mean velocity, $\bar{U}(x)$. (c) Horizontal gradient in the mean velocity, $\partial \bar{U}(x)/\partial x$. (d) Bulk Richardson number. The vertical dotted lines show the locations of the channel ends.

2.5 Wave Evolution

The two waves in figure 2.1 exhibit the classic features of fully developed Holmboe instabilities. The upward pointing (positive) cusp is moving to the right with the upper layer and the downward pointing (negative) cusp is moving to the left with the lower layer. The positive cusp is ejecting a wisp of interfacial fluid into the upper layer. The particle streaks indicate an elliptical vortex leading the positive cusp. The centre of the vortex has nearly stationary particles and is well above the density interface. Such vortices are typically present in numerical simulations of these flows [e.g. Smyth & Winters, 2003] and play an important role in the generation of the wisps. The vortex carries partially mixed interfacial fluid back toward the cusp where there is a horizontal convergence. The convergence at the cusp carries the fluid vertically away from the interface. These wisps of mixed fluid can either get caught in the leading vortex or, in some cases, are ejected above the vortex into a region of decreased shear and higher velocity. A similar vortex leads the lower cusp. Its presence is masked by the dye in the lower layer.

During the steady period (400-800s) there is a roughly even distribution of rightward and leftward propagating waves as can be seen in the characteristics diagram figure 2.7b. The characteristics represent a compilation of the interface height observed in a sequence of several thousand images (e.g. the image in figure 2.4b). The time averaged interface height (figure 2.6a) was removed and the shading is scaled such that black indicates the trough of an instability and white indicates the crest. White and black diagonal lines represent the propagating cusps of positive and negative instabilities, respectively. In general the instabilities form quickly (< 20 s) and maintain a nearly constant amplitude while they are within the channel. Despite irregularities in the characteristics the instabilities can be filtered into distinct rightward (figure 2.7a) and leftward (figure 2.7c) propagating components using the two dimensional fast Fourier transform (FFT).

The influence of the controls can be seen in the characteristics at the ends of the channel ($x = \pm 1$ m, figure 2.7a and c). Within the channel, disturbances move in both directions (subcritical) and beyond the ends of the channel they only move outwards into the reservoirs (supercritical). Although difficult to see, both upward and downward cusping modes are propagating outwards in the supercritical regions (e.g. figure 2.7c, $x = -1.05$ m, $t = 625 - 650$ s). As expected the controls block disturbances from entering the channel, i.e. waves propagating within the channel have formed there rather than within the reservoirs. Because one of the two Holmboe modes

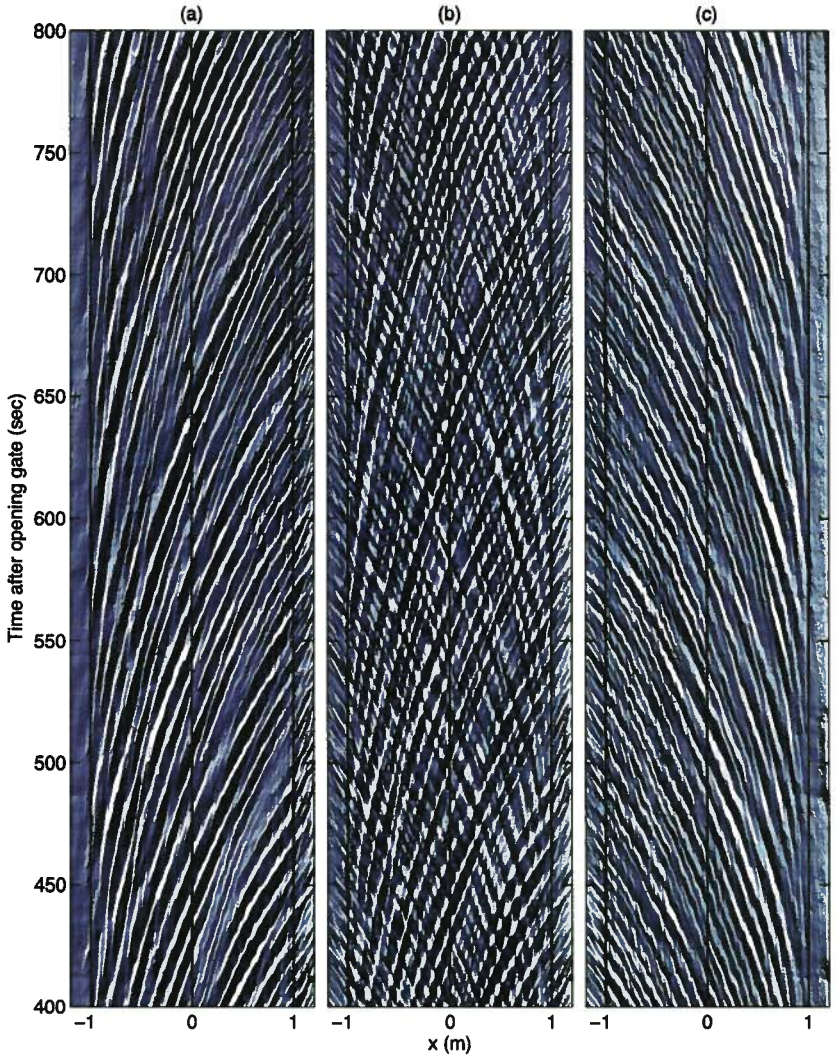

Figure 2.7: Characteristics during the period of steady exchange. The shading indicates the deviation of the interface elevation from the mean. Pure white (black) indicates a positive (negative) deviation greater than 3 mm. The characteristics in (b) were split into rightward (a) and leftward (c) propagating components using the two dimensional FFT. The ends of the channel are at $x = \pm 1$ m.

is stationary near each control, the separation of the modes using the two dimensional FFT is less effective near the ends of the channel. In addition, the nearly stationary waves near the ends of the channel have a very low frequency resulting in very few waves per experiment and therefore greater uncertainty in quantifying wave properties. For these reasons our analysis below will focus on -0.9 m$< x < 0.9$ m.

To further illustrate the wave evolution we have traced out the crests of a set of the positive, rightward propagating waves (figure 2.8a). At the left end of the channel four wave crests pass $x = -0.9$ m over a period of approximately 110 s indicating a wave period of 37 s (frequency, $\omega = 0.027$ Hz). At $x = +0.9$ m, there is still 110 s between the first and last wave crest, however, here there are 13 wave crests in total indicating an average wave period of 9.2 s ($\omega = 0.11$ Hz). This increase in frequency is a result of new waves forming throughout the channel.

The frequency evolution is quantified by counting all of the zero crossings that occur over the period of steady exchange (400 seconds) and averaging over seven experiments (Experiments 1 to 7). The characteristics were low pass filtered (wavelengths $>$ 1 cm) before counting the zero crossings to minimize the upward bias associated with noise. As in the traces, the zero crossings show an increase in the number of positive waves from left to right (figure 2.8b). The negative waves show the same accumulation in the opposite direction.

The formation of new waves is related to the changes in phase velocity that the waves undergo as they propagate along the channel. The phase velocity of a wave is given by the inverse of the slope of its characteristic (dx/dt). A nearly vertical line indicates a slow moving wave while a nearly horizontal line indicates a fast moving wave. The positive (rightward propagating) waves shown in figure 2.8a therefore accelerate from left to right (the traced lines become more horizontal). The dominant phase velocity of the waves (i.e. the slope of the wave characteristics) is determined by cross correlating time series of the interface height at adjacent locations along the channel. This phase velocity is calculated for experiments 1 to 7 and then averaged (figure 2.8c). The average shows that both the positive and negative waves accelerate as they propagate along the channel.

The wave acceleration is most easily understood by considering the variation in the mean velocity, $\bar{U}$, over the length of the channel (figure 2.6b). The mean velocity is replotted in figure 2.8c and shows a slope that is similar to the slope of the observed phase speeds. In other words, with respect to a frame of reference moving at the mean velocity, the velocity of both the rightward and leftward propagating waves remains approximately

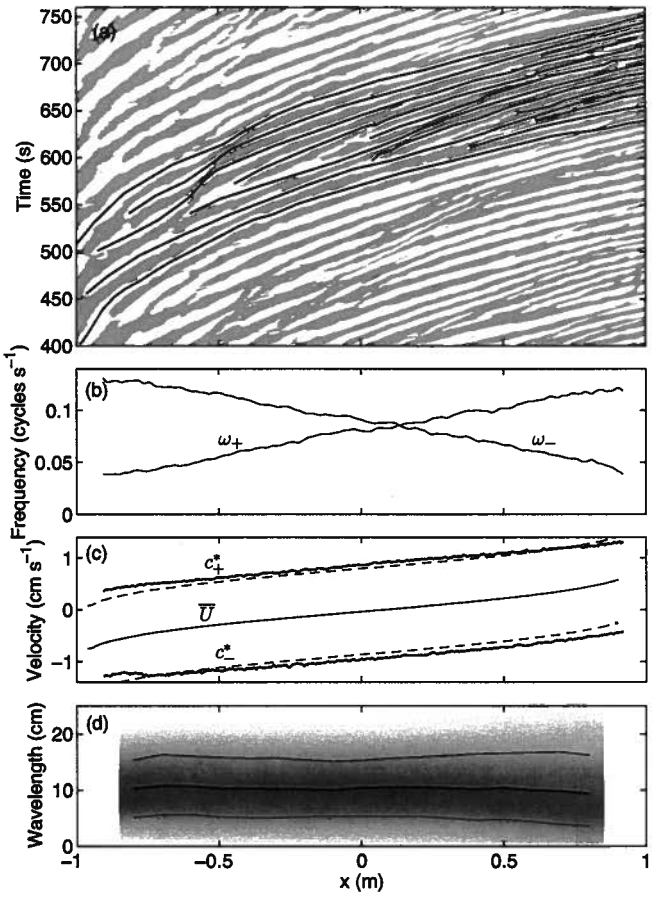

Figure 2.8: (a) Characteristics of rightward propagating waves; gray shading indicates a wave trough and white indicates a crest. The lines were traced by hand following individual wave crests. (b) The average frequency of the rightward (ω_+) and leftward (ω_-) propagating waves based on zero crossings. (c) The thick solid lines represent the phase velocity of the observed rightward (positive) propagating waves, (c^*_+) and leftward (negative) propagating waves, (c^*_-). The thin line shows $\bar{U}$ calculated using the velocity profile and interface height shown in figure 5. The dashed lines are the predicted phase speed of Holmboe instabilities. (d) The distribution of the wavelength for the rightward propagating waves with the average plotted as a heavy line and the 10 and 90 percentiles as thin lines.

constant. By adding $\bar{U}$ to the predicted phase speed for the Holmboe instability (equation 2.1) we predict the phase speed over the whole channel. This phase speed is shown for both the rightward and leftward propagating waves, $c_r^*(x) = \bar{U}(x) \pm 0.83$ cm s^{-1}, in figure 2.8c and matches closely the observed phase speed evolution.

This prediction of the phase speed (figure 2.8c) does not take into account possible changes in J along the length of the channel. However, over the central region of the channel, the variation in J is too small (figure 2.6d) to have a noticeable effect on the wavenumber of maximum growth and the corresponding phase speed.

The distribution of wavelength with respect to position is shown in figure 2.8d for rightward propagating waves. The average wavelength and position of all the waves was determined using zero crossings (similar to the frequency in figure 2.8b). The wavelength remains nearly constant ($\lambda \approx 10$ cm) throughout x. This is because the two processes, wave formation and wave acceleration, tend to cancel each other out.

Acting by itself, the increase in frequency associated with wave formation will shorten the average wavelength, $\lambda_B = \frac{\omega_A}{\omega_B}\lambda_A$, where the subscripts A and B represent different locations in x. The effect of the convective acceleration ($\partial\bar{U}/\partial x$) on the wavelength is not so obvious. As is commonly observed in surface waves [e.g. Peregrine, 1976], the acceleration will stretch the waves, increasing their wavelength, i.e. $\lambda_A = \frac{c_A}{c_B}\lambda_B$.

The wave stretching is most apparent in the temporal evolution of the wavenumber spectrum (figure 2.9 a and b). Similar to the characteristics, the spectral evolution was determined by compiling the spectrum of the interface height at each time and then contouring. Note that the horizontal axis in figure 2.9 is wavenumber not distance. The dark (high energy) diagonal streaks represent energy associated with waves moving through the channel in time (the vertical axis). The slope of the streaks is a result of individual waves stretching, i.e. waves are continuously decreasing in wavenumber (increasing in wavelength).

The time averaged spectra (figure 2.9 c and d) show the peaks in the wave energy occurring at approximately 0.5 cm^{-1} ($\lambda = 12.5$ cm). The temporal evolution and average spectrum together show the waves form near the wave number of maximum growth ($k \approx 0.9$ cm^{-1}, $\lambda \approx 7$ cm) get stretched and start to lose energy near the lower stability boundary ($k \approx 0.36$ cm^{-1}, $\lambda \approx$ 17 cm).

The two processes, wave stretching and wave formation, are illustrated in the simplified schematic shown in figure 2.10. The schematic shows the interface elevation at three times. The reference frame ($x = 0$ in the figure)

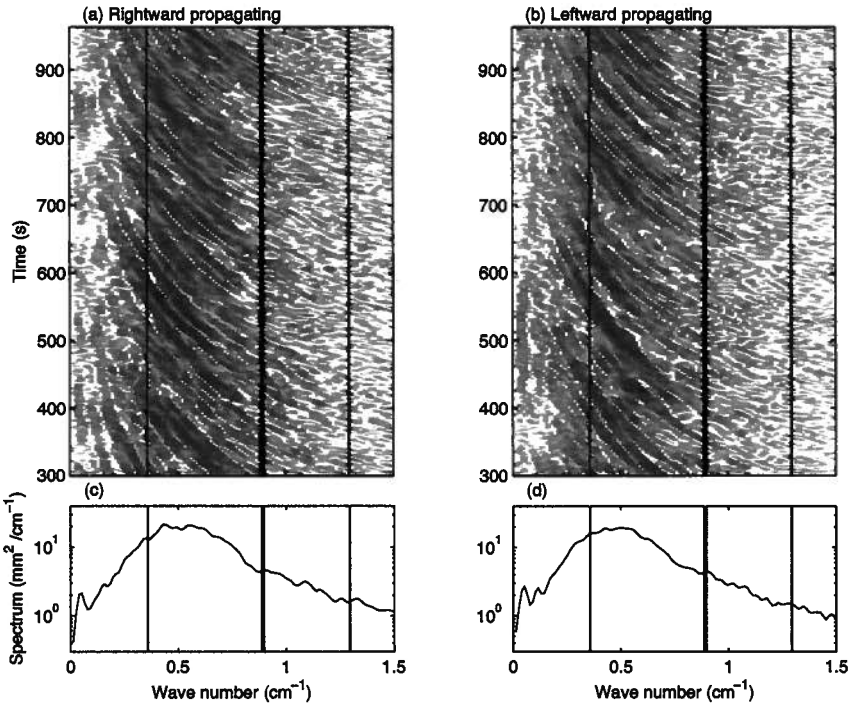

Figure 2.9: Spectrum of waves during the steady period between $x = -0.8$ m and $x = 0.8$ m. (a) and (b) Temporal evolution of the spectrum for the rightward and leftward propagating waves respectively. The shading is scaled logarithmically from white (low energy) to black (high energy). (c) and (d) Time averaged spectrum. The heavy vertical line indicates the wavenumber of maximum growth ($k \approx 0.9$ cm^{-1}, $\lambda \approx 7$ cm) and the thin vertical lines indicate the stability boundaries ($k \approx 0.36$ cm^{-1}, $\lambda \approx 17$ cm and $k \approx 1.3$ cm^{-1}, $\lambda \approx 5$ cm).

is moving at the speed of the trailing wave crest. As shown in figure 2.8c waves undergo the same convective acceleration as $\bar{U}(x)$. In the central region of the channel this acceleration is approximately 0.005 s^{-1} (see $\partial\bar{U}/\partial x$ in figure 2.6 c). As the pair of crests propagate through the channel the horizontal variation in $\bar{U}$ gives the leading crest a slightly greater phase speed than the trailing crest ($\lambda\ \partial\bar{U}/\partial x = 0.035$ cm s^{-1}). This difference in phase speed allows the leading crest to pull away from the trailing crest. As

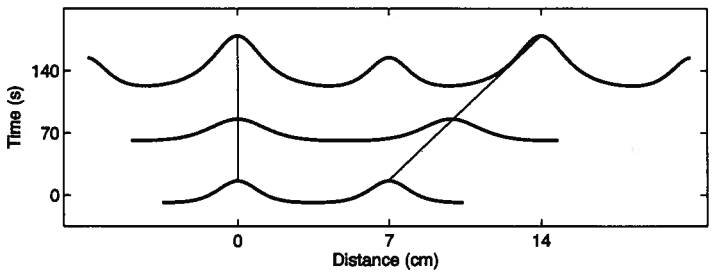

Figure 2.10: Schematic of stretching and formation of rightward propagating waves. The interface elevation is shown at three times tracking the same wave. The horizontal distance at each time is relative to the trailing crest of the wave. The wave is shown initially with a wavelength equal to the wavelength of maximum growth. Eventually the wave is stretched to twice this length. At the same time new waves form, also at the wavelength of maximum growth. The resulting interface has waves of mixed amplitude and wavelength. The time scale shown for doubling of the wavelength (approximately 140 s) is based on the observations (see figure 2.9a and b).

the spacing between the two crests (λ) increases, their growth rate decreases (i.e. they are no longer at the wavelength of maximum growth). On the other hand, as the spacing increases the interface between the crests becomes unstable to shorter waves (i.e. waves that are closer to the wavenumber of maximum growth) and a new wave forms. The new waves grow and stretch and eventually the process repeats itself (see figure 2.8a).

2.6 Summary and Conclusions

Instabilities were investigated using an exchange flow through a long rectangular channel with a rectangular cross section. The channel connected two large fresh water and salt water reservoirs. A long period of steady maximal exchange occurred after the cessation of Helmholtz resonance and ended when one of the controls was flooded. During this time symmetric Holmboe instabilities were observed. These instabilities evolved into cusps with a leading elliptical vortex. The vortices drew mixed fluid from the cusp into the free stream. The observed density interface was sharper than, and centred within, the shear layer.

The gradual slope of the interface along the length of the channel re-

sulted in the convective acceleration of each layer. The Holmboe instabilities also accelerated as they propagated through the channel. This acceleration caused the distance between successive cusps to increase and new waves formed. The new waves formed uniformly along the channel such that the average wavelength remained nearly constant.

By focusing on the central section of the channel we selected the region where the Bulk Richardson number is relatively constant. This, together with the prolonged period of steady exchange and simple channel geometry, resulted in instabilities that had average wave properties that were in good agreement with the linear predictions of Holmboe.

Bibliography

ALEXAKIS, A. 2005 On Holmboe's instability for smooth shear and density profiles. *Phys. Fluids* **17**, 084103.

ARMI, L. 1986 The hydraulics of two flowing layers with different densities. *J. Fluid Mech.* **163**, 27–58.

CARPENTER, J.R., LAWRENCE, G.A. & SMYTH, W.D. 2007 Evolution and mixing of asymmetric Holmboe instabilities. *J. Fluid Mech.* **582**, 103–132.

FARMER, D.M. & ARMI, L. 1998 The flow of Atlantic water through the Strait of Gibraltar. *Prog. Oceanogr.* **21**, 1–98.

GEYER, W.R. & SMITH, J.D. 1987 Shear instability in a highly stratified estuary. *J. Phys. Oceanogr.* **17**, 1668–1679.

GU, L. & LAWRENCE, G. 2005 Analytical solution for maximal frictional two-layer exchange flow. *J. Fluid Mech.* **543**, 1–17.

HOGG, A. MCC. & IVEY, G.N. 2003 The Kelvin-Helmholtz to Holmboe instability transition in stratified exchange flows. *J. Fluid Mech.* **477**, 339–362.

HOLMBOE, J. 1962 On the behavior of symmetric waves in stratified shear layers. *Geofys. Publ.* **24**, 67–112.

KOOP, C. G. & BROWAND, F.K. 1979 Instability and turbulence in a stratified fluid with shear. *J. Fluid Mech.* **93**, 135–159.

LAWRENCE, G.A., BROWAND, F.K. & REDEKOPP, L.G. 1991 The stability of a sheared density interface. *Phys. Fluids* **3** (10), 2360–2370.

MILES, J. & MUNK, W. 1961 Harbor paradox. *J. WatWays Harb. Am. Soc. Civ. Engrs WW3* **87**, 111–130.

PEREGRINE, D. H. 1976 Interaction of water waves and currents. *Adv. Appl. Mech.* **16**, 9–117.

POULIQUEN, O., CHOMAZ, J. M. & HUERRE, P. 1994 Propagating holmboe waves at the interface between two immiscible fluids. *J. Fluid Mech.* **266**, 277–302.

SMYTH, W.D. 2006 Secondary circulations in Holmboe waves. *Phys. Fluids* **18** (064104), 1–13.

SMYTH, W.D., CARPENTER, J.R. & LAWRENCE, G.A. 2007 Mixing in symmetric Holmboe waves. *J. Phys. Oceanogr.* **37**, 1566–1583.

SMYTH, W. D. & WINTERS, K. B. 2003 Turbulence and mixing in Holmboe waves. *J. Phys. Oceanogr.* **33**, 694–711.

TEDFORD, E., CARPENTER, J., PAWLOWICZ, R. & LAWRENCE, G. 2007 Linear stability analysis in a salt wedge. In *Proceedings of the Fifth International Symposium on Environmental Hydraulics*. Tempe, Arizona, USA.

THORPE, S. 1971 Experiments on instability of stratified shear flows: miscible fluids. *J. Fluid Mech.* **46**, 299–319.

WESSON, J. C. & GREGG, M. C. 1994 Mixing at Camarinal Sill in the Strait of Gibraltar. *J. Geophys. Res.* **99**, 9847–9878.

YOSHIDA, S., OHTANI, M., NISHIDA, S. & LINDEN, P.F. 1998 Mixing processes in a highly stratified river. In *Physical Processes in Lakes and Oceans*, *Coastal and Estuarine Studies*, vol. 54, pp. 389–400. American Geophysical Union.

ZHU, D. & LAWRENCE, G.A. 2001 Holmboe's instability in exchange flows. *J. Fluid Mech.* **429**, 391–409.

Chapter 3

Observation and Analysis of Shear Instability in the Fraser River Estuary [2]

3.1 Introduction

Shear instabilities occur in highly stratified estuaries and can influence the large scale dynamics by redistributing mass and momentum. Specifically, shear instabilities have been found to influence salinity intrusion in the Fraser River estuary [Geyer & Smith, 1987; Geyer & Farmer, 1989; MacDonald & Horner-Devine, 2008]. We describe recent observations in this estuary and examine the shear and stratification that lead to instability. The influence of long time scale processes such as freshwater discharge and the tidal cycle are also discussed.

Rather than relying on a bulk or gradient Richardson number to assess stability we use numerical solutions of the Taylor-Goldstein (TG) equation based on observed profiles of velocity and density. This approach has been used with some success in the ocean [e.g. Moum *et al.*, 2003] but, with the exception of the simplified application by Yoshida *et al.* [1998], has not been applied in estuaries. Solving the TG equation provides the growth rate, wavelength, phase speed and mode shape of the instabilities. We compare these predicted wave properties with instabilities observed using an echosounder.

Geyer & Farmer [1989] found that instabilities in the Fraser River estuary were most apparent during ebb tide when strong shear occurred over the length of the salinity intrusion. They outlined a progression of three phases of increasingly unstable flow that occurs over the course of the ebb. In the first phase, strain sharpens the density interface; shear is stronger than

[2]This chapter has been submitted for publication in: E.W. Tedford, J.R. Carpenter, R. Pawlowicz, R. Pieters and G.A. Lawrence (2009),Observation and Analysis of Shear Instability in the Fraser River Estuary, *J. Geophys. Res.*

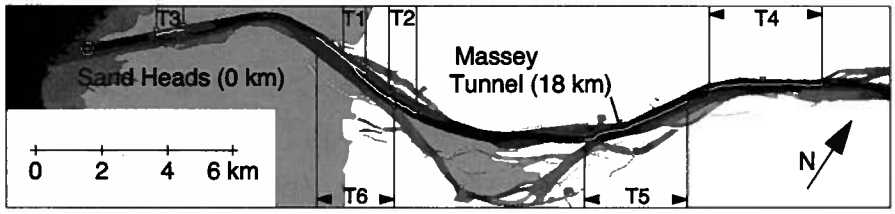

Figure 3.1: Map of the lower 27 km of the Fraser River. The locations of the six transects are marked T1-T6. The mouth of the river (Sand Heads) is located at 49° 6′ N and 123° 18′ W.

during flood but insufficient to cause shear instability. In the second phase, the lower layer reverses direction causing shear between the fresh and saline layers to increase. Shear instability and turbulent mixing are concentrated at the pycnocline rather than in the bottom boundary layer. By the third phase of the ebb, shear instability has completely mixed the two layers leaving homogeneous water throughout the depth. During flood there is some mixing, however it is concentrated at the front located at the landward tip of the salinity intrusion. Similarly, MacDonald & Horner-Devine [2008], studying mixing at high fresh water discharge (7000 m^3s^{-1}), found that two to three times more mixing occurred during ebb tide than during flood. The present analysis is focused on the ebb tide at high and low freshwater discharge, although some results during flood tide are also presented.

The paper is organized as follows. The setting and field methods are described in section 3.2. The general structure of the salinity intrusion is described in section 3.3. In section 3.4 we present the background theory needed to perform stability analysis in the Fraser River estuary. In section 3.5 predictions from the stability analysis are compared with observations. In section 3.6 the source of relatively small scale overturning is briefly discussed. In section 3.7 the results of the stability analysis are discussed followed by conclusions in section 3.8.

3.2 Site Description and Data Collection

Data were collected in the main arm of the Fraser River estuary, British Columbia, Canada (figure 3.1). The estuary is 10 to 20 m deep with a channel width of 600 to 900 m. Cruises were conducted on June 12, 14 and

	Discharge ($m^3\ s^{-1}$)	Tide	x (km)	ΔU ($m\ s^{-1}$)	$\Delta\rho$ ($kg\ m^{-3}$)	h (m)	J
1	6400	Ebb	8.6	1.6	14.3	5.2	0.29
2	6500	Ebb	11	1.65	20	3.5	0.25
3	5700	Flood	2.2	1.5	23.1	3.5	0.35
4	850	Ebb	24.5	1.5	12.9	12	1.3
5	850	Ebb	19	1.5	12.9	12	1.3
6	850	Ebb	10.5	2.5	7.3	12	0.3

Table 3.1: Details of transects shown in figures 3.1 and 3.2. The location indicates the distance upstream from the mouth (Sand Heads).

21, 2006 and March 10, 2008. Here we present one transect from each of the June 2006 cruises and three transects from the March 2008 cruise (see Table 3.1). The freshwater discharge during the June 2006 transects was typical of the freshet at approximately 6000 m^3s^{-1}. During the March 2008 transects, freshwater discharge was near the annual minimum at 850 m^3s^{-1}. In June 2006, transects were made during both ebb and flood tide. In March 2008, transects cover most of a single ebb tide (figure 3.2). The tides in the Strait of Georgia have $M2$ and $K1$ components of similar amplitude (approximately 1 m) resulting in strong diurnal variations. The tidal range varies from approximately 2 m during neap tides to approximately 4.5 m during spring tides. During both the 2006 and 2008 observations the tidal range was approximately 3 m.

The distance salinity intrudes landward of Sand Heads, i.e. the total length of the salinity intrusion, varies considerably with tidal conditions and freshwater discharge. Ward [1976], found the maximum length of the intrusion occurred just after high tide and varied from 8 km at high discharge (9000 m^3s^{-1}) to 31 km at low discharge (850 m^3s^{-1}). Geyer & Farmer [1989] found that, at average discharge (3000 m^3s^{-1}), the maximum length of the intrusion matched the horizontal excursion of the tides (10 to 20 km) and, similar to Ward [1976], occurred just after high tide. Kostachuk & Atwood [1990] found that the minimum length of the salinity intrusion typically occurred approximately one hour after low tide. The longest intrusion they observed at low tide was approximately 20 km. They predicted that complete flushing of salt from the estuary would occur on most days during the freshet (freshwater discharge $> 5000\ m^3s^{-1}$).

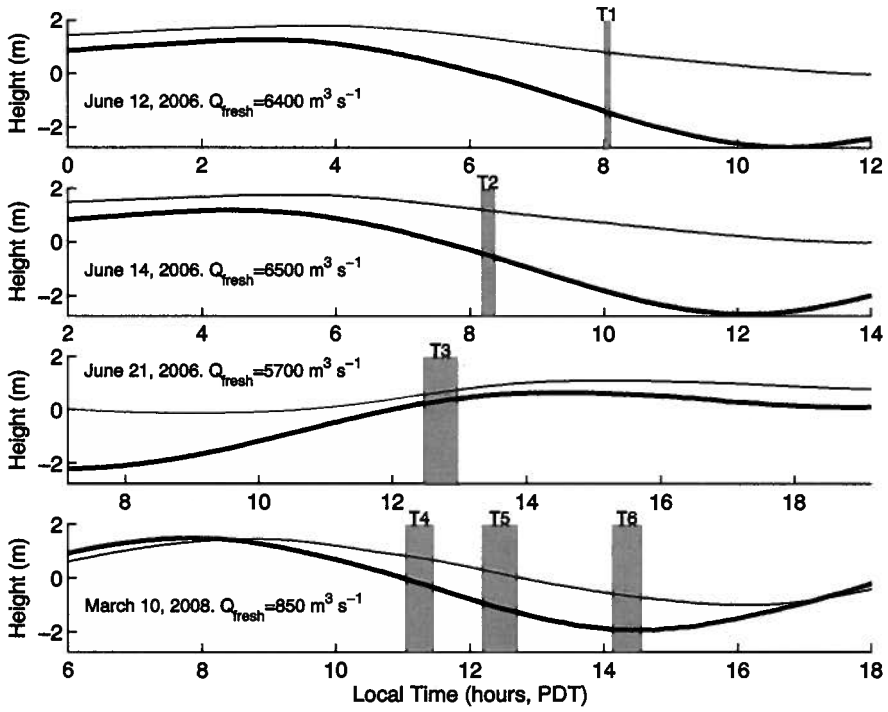

Figure 3.2: Observed tides at Point Atkinson (heavy line) and New Westminster (thin line) for the four days of field observations. The Point Atkinson data is representative of the tides in the Strait of Georgia beyond the influence of the Fraser River. New Westminster is located 37 km upstream of the mouth of the river at Sand Heads (see figure 3.1). The records are both referenced to mean sea level at Point Atkinson. The duration of the six transects are marked T1-T6.

Field Methods

Data along the six transects were collected by drifting seaward with the surface flow while logging velocity and echosounder data and yoyoing a CTD (conductivity, temperature and depth) profiler. The velocity measurements were made with a 1200 kHz RDI Acoustic Doppler Current Profiler (ADCP) sampling at 0.4 Hz with a vertical resolution of 250 mm. The velocities were averaged over 60 seconds to remove high frequency variability. The echo soundings were made with a 200 kHz Biosonics sounder sampling at 5

Hz with a vertical resolution of 18 mm. Profile data was collected with a Seabird 19 sampling at 2 Hz. Selected echosounder, ADCP and CTD data are shown in figure 3.3. As indicated by the superimposed density profiles, strong gradients in density are generally associated with a strong echo from the sounder.

The CTD was profiled on a load bearing data cable that provided constant monitoring of conductivity, temperature and depth. This data allowed us to quickly identify the front of the salinity intrusion and avoid direct contact of the instrument with the bottom. To increase the vertical resolution of the profiles, the CTD was mounted horizontally with a fin to direct the sensors into the flow. In this configuration, the instrument was allowed to descend rapidly and then was raised slowly (0.2 - 0.4 m s^{-1}) relying on horizontal velocity of the water relative to the CTD to flush the sensors. The upcast, which had higher vertical resolution, was in reasonable agreement with the echo intensity from the sounder. On the few occasions that the higher resolution upcast did not coincide with the appearance of instabilities in the echosounder, we used the downcast.

3.3 General Description of the Salinity Intrusion

We observed important differences in the structure of the salinity intrusion between high and low freshwater discharge. At high discharge, our observations were similar to those described by Geyer & Farmer [1989] at average discharge (3000 m^3 s^{-1}), where the salinity intrusion had a two-layer structure resembling a classic salt-wedge. At low discharge, however, the salinity intrusion exhibited greater complexity.

3.3.1 High Discharge

During flood tide, mixing was concentrated near the steep front at the landward tip of the salt-wedge (2.7 to 3.03 km in figure 3.3c). During ebb tide, the steep front was replaced by a gently sloping pycnocline (figure 3.3b landward of 11.6 km) and there was no apparent concentration of mixing at the landward tip of the salt-wedge (not shown).

We will focus on the wave-like disturbances that occur on the pycnocline especially during ebb tide. The largest of these were observed during transect 1 (figure 3.3a 8.7 to 8.9 km, between depths of 3 and 9 m). These disturbances occurred within the upper layer as it passed over the nearly stationary water below a depth of 10 m. Smaller amplitude disturbances

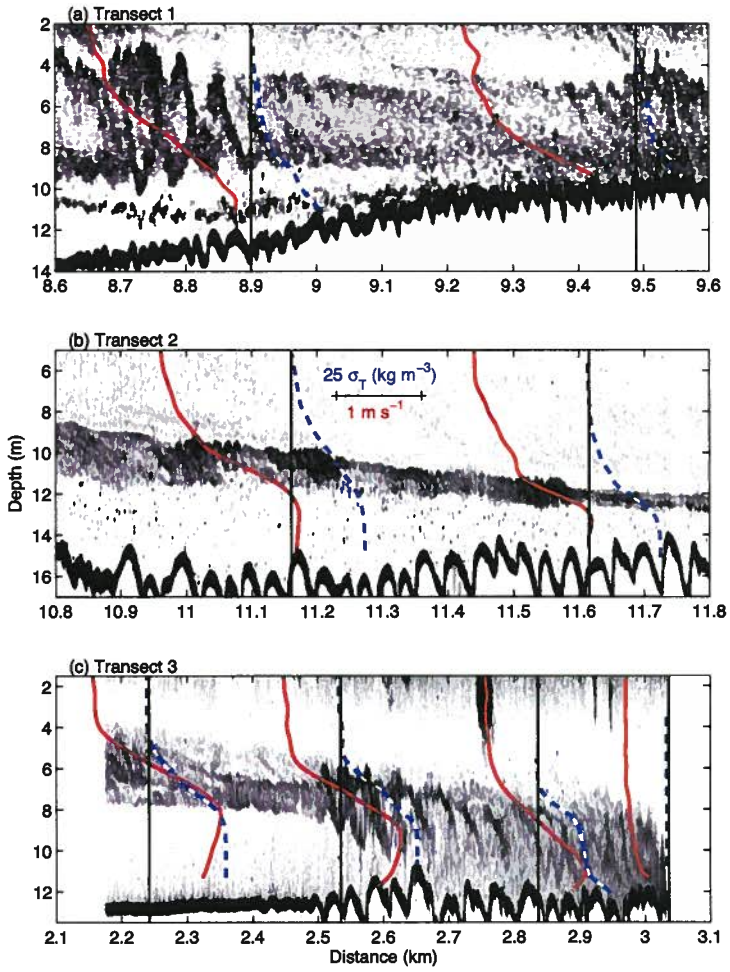

Figure 3.3: Echo soundings observed during high discharge on: (a) transect 1, ebb tide; (b) transect 2, ebb tide; (c) transect 3, flood tide. The shading scales with the log of the echo intensity with black corresponding to the strongest echos. Selected velocity profiles (red) from the ADCP and density profiles (blue dash) from the CTD are superimposed (not all are shown). The black line indicates the location of the boat in the middle of the cast, as well as the zero reference for the velocity and σ_t. The velocity profile was calculated as a 1 minute average centred on the time of the CTD cast. The undulations in the bed of the river (thick black line at the bottom of the echosoundings) are a result of sandwaves.

were observed during transect 2 (figure 3.3b 11.05 km). In our application of the TG equation we will show that disturbances like these are a result of shear instability.

Not all of the disturbances on the pycnocline are a result of shear instability. For example, for most of the velocity and density profiles collected during transect 3 (figure 3.3c) the TG equation does not predict instability. The disturbances seen from 2.5 to 2.8 km are caused by the large sand waves on the bottom (the thick black line in the echo sounding). The crests of the sand waves were typically 30 m apart and 1 to 2 m high, and were found over most of the river surveyed during high discharge (2.5 km to 15 km). During flood tide, flow over these sand waves caused particularly regular disturbances on the pycnocline.

3.3.2 Low Discharge

At low discharge, at the beginning of the ebb, the front of the salinity intrusion was located between 28 and 30 km from Sand Heads. Unlike the observations at high discharge a well defined front was not visible in the echosounder, and CTD profiles were needed to identify its location. Seaward of the front (figure 3.4a), the echosounder and the CTD profiles show a multilayered structure with more complexity than was observed at high discharge. At this early stage of the ebb, the CTD profiles generally show partially mixed layers separated by several small density interfaces.

Later in the ebb, during transect 5 (figure 3.4b), near bottom velocities turn seaward and the velocity shear between the top and the bottom increases. At maximum ebb (transect 6, figure 3.4c), the shear increases further, reaching a maximum of approximately 2.5 m s^{-1} over a depth of 12 m. Mixed water occurs at both the surface and the bottom resulting in an overall decrease in the vertical density gradient. By the time transect 6 is complete the ebb flow is decelerating. The salinity intrusion continues to propagate seaward until low tide but, given its length and velocity it does not have sufficient time to be completely flushed from the estuary. During the next flood the mixed water remaining in the estuary allows a complex density structure to develop similar to that seen early in the observed ebb. This differs from the behaviour at high freshwater discharge when nearly all of the seawater is flushed completely from the estuary at least once a day.

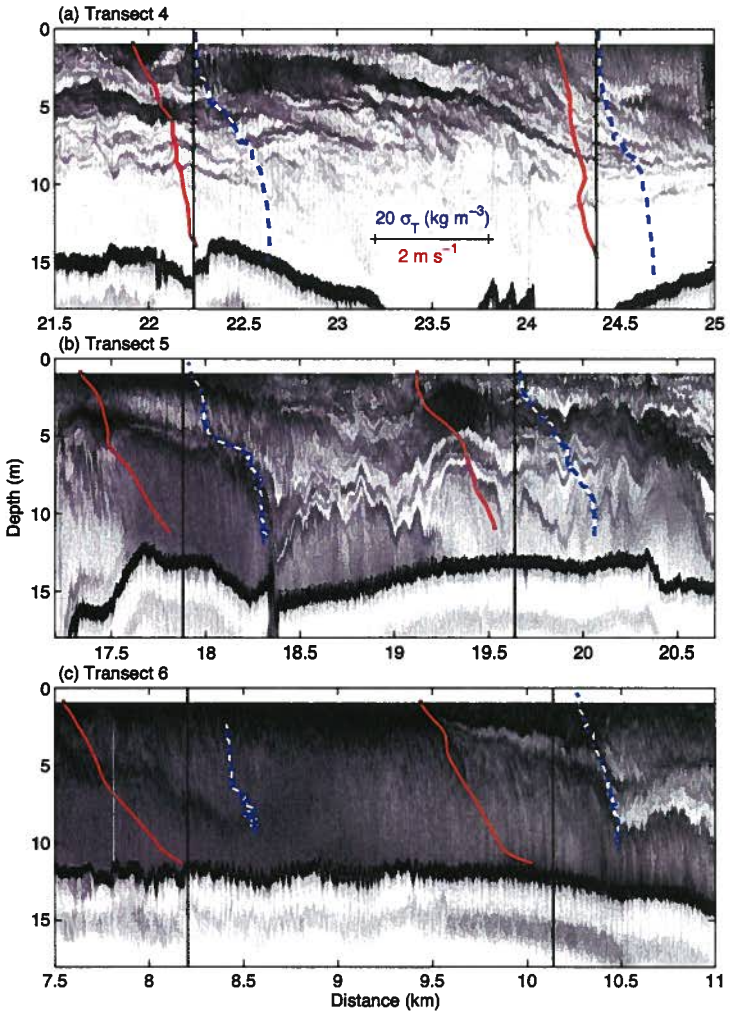

Figure 3.4: Echo soundings during low discharge observed during: (a) transect 4, early ebb; (b) transect 5, mid ebb; and (c) transect 6, late ebb. The shading scales with the log of the echo intensity with black corresponding to the strongest echos. Note that the scale of the shading is the same in all three panels. Velocities(red) from the ADCP and densities(blue dashed) from the CTD are superimposed. The black line indicates the location of the boat in the middle of the cast, as well as the zero reference for the velocity and σ_t. The velocity profile was calculated as a 1 minute average centred on the time of the CTD cast.

3.4 Stability of Stratified Shear Flows

3.4.1 Taylor-Goldstein Equation

Following Taylor [1931] and Goldstein [1931] we assess the stability of the flow by considering the evolution of perturbations on the background profiles of density and horizontal velocity, denoted here by $\rho(z)$ and $U(z)$, respectively. If the perturbations to the background state are sufficiently small they are well approximated by the linear equations of motion. It then suffices to consider sinusoidal perturbations, represented by the normal mode form $e^{ik(x-ct)}$, where x is the horizontal position and t is time. Here $k = 2\pi/\lambda$ is the horizontal wave number with λ the wavelength, $c = c_r + ic_i$ is the complex phase speed. If we further assume that the flow is incompressible, Boussinesq, inviscid, and non-diffusive, we arrive at the Taylor-Goldstein (TG) equation

$$\frac{d^2\hat{\psi}}{dz^2} + \Big[\frac{N^2}{(U-c)^2} - \frac{d^2U/dz^2}{U-c} - k^2\Big]\hat{\psi} = 0, \tag{3.1}$$

where the stream function is given by $\psi(x,z,t) = \hat{\psi}(z)e^{ik(x-ct)}$ and $N^2(z) = (g/\rho_0)(d\rho/dz)$ represents the Boussinesq form of the squared buoyancy frequency with a reference density, ρ_0.

Solutions to the TG equation consist of eigenfunction-eigenvalue sets $\{\hat{\psi}(z), c\}$, for each value of k. Each set $\{\hat{\psi}(z), c\}$ is referred to as a mode, and the solution may consist of the sum of many such modes for a single k. The background flow, represented by $U(z)$ and $\rho(z)$, is then said to be unstable if any modes exist that have $c_i \neq 0$. In this case the small perturbations grow exponentially at a rate given by kc_i. In general, unstable modes are found over a range of k, and it is the mode with the largest growth rate that is likely to be observed. Although they are based on linear analysis, TG predictions of the wave properties, k and c, typically match those of finite amplitude instabilities observed in the laboratory [Thorpe, 1973; Lawrence *et al.*, 1991, and Chapter 2].

3.4.2 Miles-Howard Criterion

A useful criterion to assess the stability of a given flow without solving the TG equation was derived by Miles [1961] and Howard [1961]. They found that if the gradient Richardson number, $Ri(z) = N^2/(dU/dz)^2$, exceeds 1/4 everywhere in the profile, then the TG equation has no unstable modes, i.e. c_i must be zero for all modes. In other words, $Ri > 1/4$ everywhere is a

sufficient condition for stability, referred to as the Miles-Howard criterion. Note that if $Ri \leq 1/4$ at some location, instability is possible, but not guaranteed.

Despite the inconclusive nature of the Miles-Howard criterion for determining instability, it is often employed as a sufficient condition for instability in density stratified flows, and has been found to have reasonable agreement with observations [Thorpe, 2005, p. 201-204]. Looking specifically at the Fraser River estuary, Geyer & Smith [1987] were able to compute statistics of Ri and show that decreases in Ri were accompanied by mixing in the estuary.

3.4.3 Mixing Layer Solution

Since the TG equation is an eigenvalue problem with variable coefficients, analytical solutions can only be obtained for the simplest profiles, and recourse is usually made to numerical methods [e.g. Hazel, 1972]. However, the available analytical solutions are often a useful point of departure. We look at one such solution that closely approximates conditions found in the estuary during high discharge. This solution is based on the simple mixing layer model of Holmboe [described in Miles, 1963].

In this model, the velocity and density profiles are represented by hyperbolic tangent functions,

$$U(z) = \frac{\Delta U}{2} \tanh\left(\frac{2z}{h}\right) \quad \text{and} \quad \rho(z) = -\frac{\Delta\rho}{2} \tanh\left(\frac{2z}{\delta}\right) + \rho_0. \tag{3.2}$$

In the simplest case the shear layer thickness, h, and the density interface thickness, δ are equal, giving $R = h/\delta = 1$. In this case, $Ri(z)$ is at its minimum at the center of the mixing layer ($z = 0$), and is equal to the bulk Richardson number $J = g\Delta\rho h/\rho_0(\Delta U)^2$. When the bulk Richardson number (i.e. the minimum Ri) drops below $1/4$, flows with $R = 1$ become unstable. The resulting instabilities are of the Kelvin-Helmholtz (KH) type, in which the shear layer rolls up to form an array of billows that are stationary with respect to the mean flow, and which display large overturns in density [Thorpe, 1973].

It is not generally the case that $J > 1/4$ results in stability. For example, if δ is reduced such that $R > 2$, an additional mode of instability, the Holmboe mode, is excited [Alexakis, 2005]. In this case, the range of J over which instability occurs extends above $1/4$. That is, $Ri < 1/4$ somewhere in z at the same time as $J > 1/4$. While it is generally true that flows with

higher J are subject to less mixing by shear instabilities, by itself, J does not indicate whether or not a flow is unstable.

For simplicity, the analytical solution of Holmboe's mixing layer model assumes the flow is unbounded in the vertical. In our analysis we include boundaries at the top and bottom where $\hat{\psi}$ must satisfy the boundary condition $\hat{\psi} = 0$. The presence of these boundaries tends to extend the range of unstable wavenumber to longer wavelengths [Hazel, 1972]. However, in the cases considered here, at the wavenumber of maximum growth, the boundaries have little or no impact on k and c.

3.4.4 Solution of the TG Equation for Observed Profiles

We use the numerical method described in Moum *et al.* [2003] to generate solutions to the TG equation based on measured velocity and density profiles. Whenever possible we use velocity and density profiles collected at the upstream edge of apparent instabilities in the echosoundings. The velocity profile, a 60 second average, is an average over one or more instabilities (the instabilities have periods < 60 seconds). This averaging reduces the influence of individual instabilities on the velocity profile, which in the TG equation, is taken to represent the background velocity profile. The velocity profile is then smoothed in the vertical using a low pass filter (removing vertical wavelengths < 2 m). The density profile is smoothed by fitting a linear function, and one or more tanh functions (one for each density interface). By using smooth profiles we are effectively ignoring instability associated with small scale variations in the profiles.

Because the point of observation moves in time, i.e. the boat is drifting seaward, predicted wavelengths from the TG equation cannot be compared directly to the wavelength of instabilities as they appear in the echosoundings. The wavelength predicted with the TG solution must be shifted to account for the speed of the instabilities with respect to the speed of the boat:

$$\lambda^* = \left|\frac{v_b}{c_r - v_b}\right|\lambda. \tag{3.3}$$

Here v_b is the velocity of the boat and c_r and λ are the phase speed and wavelength predicted with the TG equation. The predicted apparent wavelength, λ^*, is directly comparable to observations made from the moving boat. Seim & Gregg [1994] used a similar approach for estimating the wavelength of observed features.

As well as giving a wavelength, phase speed, and growth rate for each unstable mode, the TG solutions also give an eigenfunction that describes

the vertical structure of the growing mode. The vertical displacement eigenfunction $\hat{\eta}(z) = -\hat{\psi}/(U-c)$ is particularly useful. At the location in z where $|\hat{\eta}|$ is a maximum we expect to see evidence of instabilities in the echosoundings.

3.5 Results

In this section we use J, $Ri(z)$ and solutions of the TG equation to assess the stability of six sets of velocity and density profiles (one from each of the six transects). Each set of profiles was chosen to coincide with evidence of instability in the echosoundings.

Ebb During High Discharge: Transect 1

The selected velocity and density profiles from transect 1 are shown in figure 3.5. The corresponding value of J for these profiles is 0.29 (see Table 3.1). The stability analysis yields two modes of instability. The fastest growing mode is unstable for wavelengths greater than 11 m and has a peak growth rate of 0.025 s^{-1} (doubling time of 28 s) occurring at a wavelength of 21 m. The phase speed of the instability at this wavelength is -1.02 m s^{-1}, where the negative indicates a seaward direction. Given this phase speed and the seaward drift of the boat (-2.2 m s^{-1}), an apparent wavelength of 39 m is calculated.

Echosoundings collected at the same time, figure 3.5c, show clear evidence of instabilities. The prediction is found to be similar to, although shorter than, the approximately 50 m wavelength of the observed instabilities. The maximum displacement of the predicted instabilities is located at a depth of 7.6 m (indicated by the horizontal line), closely matching the depth of the observed instabilities. Both the observed and predicted instability occur within the region of shear above the maximum gradient in ρ (at a depth of 9 m). As indicated by the gray shading, this region of high shear and low gradient in ρ corresponds to $Ri < 1/4$.

For the set of profiles shown in figure 3.5 the TG equation predicts a second, weaker, unstable mode located at a depth of 2.5 m. This mode is associated with the inflection point ($d^2U/dz^2 = 0$) in the velocity profile at this depth. Because there is very little density stratification and hence weak echo intensity at this depth we are unable to confirm or deny the presence of this mode in the echosoundings.

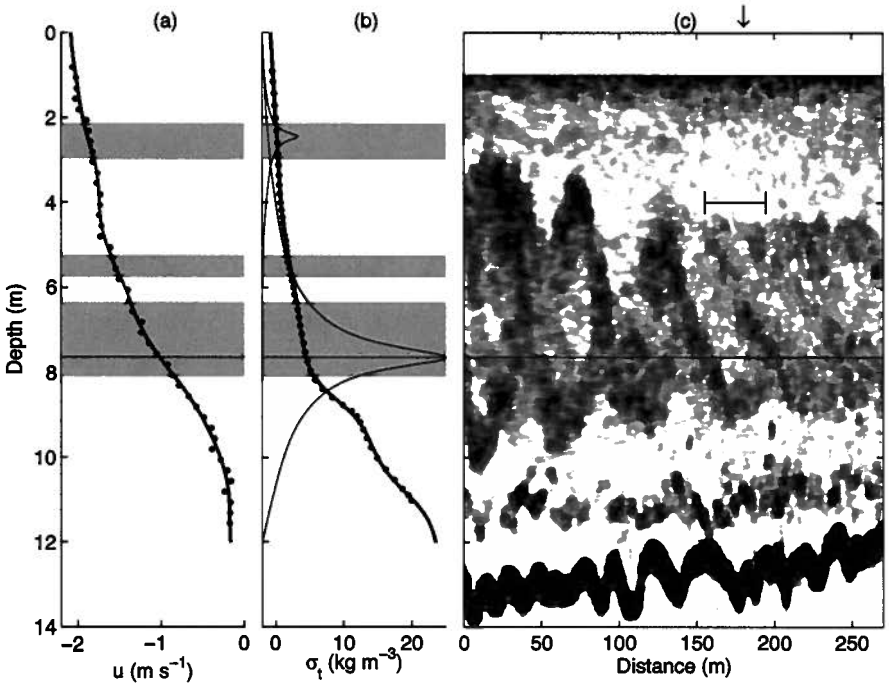

Figure 3.5: Velocity (a) and density (b) profiles observed during transect 1 (June 12, 2006, 8h05 PDT, 8.9 km upstream of Sand Heads). The smooth profiles used in the stability analysis are shown as thick black lines and the observed data are plotted as points. The gray shading indicates regions in which $Ri < 1/4$. The black horizontal line indicates the location of maximum displacement ($|\hat{\eta}|$) for the most unstable mode predicted with the TG equation. The thin lines in (b) show the displacement functions for each of the unstable modes. The functions are scaled in proportion to the growth rate. A close up of the echosounding logged near the location of the profiles is shown in (c), and includes a scale indicating the apparent wavelength predicted by the TG equation. The arrow at the top of image indicates the approximate location of the density and velocity measurements. In this case, the velocity is averaged over a distance of approximately 130 m.

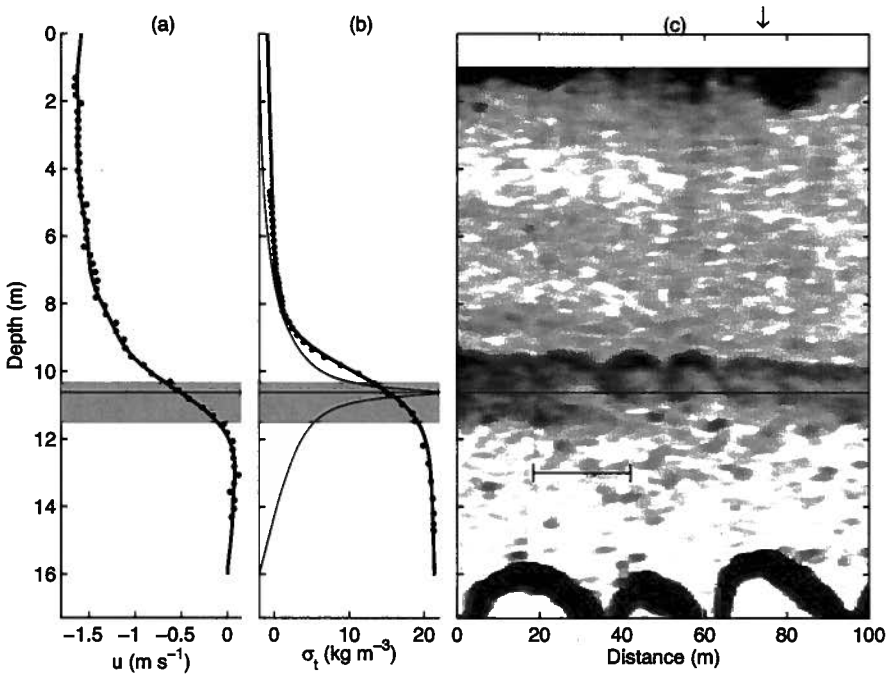

Figure 3.6: Velocity (a) and density (b) profiles observed during transect 2 (June 14, 2006, 8h21 PDT, 11.1 km upstream of Sand Heads). See figure 3.5 for details. In this case, the velocity is averaged over approximately 110 m.

Ebb During High Discharge: Transect 2

In transect 2 a single hyperbolic tangent gives a good fit to the measured density profile (figure 3.6b). Due to difficulties in profiling, the density profile at this location was missing data below 12 m. Data from the previous cast, taken 60 m upstream, was used below 12 m. This cast is expected to be sampling water of similar density below this depth.

In this case the stability analysis of the profiles results in a single mode of instability. The mode is unstable for wavelengths from 10 m to 35 m with a peak growth rate of 0.02 s^{-1} (doubling time of 35 s) occurring at a wavelength of 17 m. The phase speed of the instability at this wavelength is -0.51 m s^{-1}. Given the drift velocity of -1.9 m s^{-1}, an apparent wavelength of 24 m is calculated. This prediction is found to be similar to, although

longer than, the approximately 18 m wavelength of the small instabilities appearing in the echosounding (figure 3.6c). The maximum displacement of the predicted instabilities is located at a depth of 10.6 m, closely matching the depth of the observed instabilities.

Flood During High Discharge: Transect 3

Despite the occurrence of $Ri < 1/4$ the stability analysis of the profiles in figure 3.7a and 3.7b does not find any unstable modes. Echosoundings collected during the flood generally show features on the pycnocline that were well correlated with sand waves (figure 3.7c). These correlated features are likely controlled by the hydraulics of the flow over the sand waves.

There was very little evidence of instabilities independent of these sand waves. There appear to be some wave-like features on the pycnocline that are shorter ($\approx$ 10 m) than the sandwaves, however, these are not well resolved by the echosounder (e.g. depth of 9 m at $x = 60$ m). Properly assessing the stability of the flow over these sandwaves would require at least two or three sets of density and velocity profiles per sandwave, many more than we were able to obtain.

Low Freshwater Discharge

Early Ebb During Low Discharge: Transect 4

At low discharge, during the ebb tide, shear and density stratification are spread over the entire depth (see figure 3.4). The vertical scales, h and δ, are therefore greater than at high discharge, where shear and stratification were concentrated at a single interface. The increase in h results in greater J despite a decrease in the density stratification, $\Delta\rho$ (see Table 3.1).

The profiles collected early in the ebb (transect 4, figure 3.8) exhibit a number of homogeneous and weakly stratified layers connected by high-gradient steps, in both U and ρ. At some locations the steps appear to coincide in both velocity and density, however, this is not always the case. Note that smoothing of the velocity reduces much of the step structure in the measured profile, which occurs on the scale of the instrument resolution. Despite this smoothing the Ri profile shows four regions in which it drops below critical.

The stability analysis yields two modes of instability. The most unstable mode has a peak growth rate of 0.023 s^{-1} occurring at a wavelength of 10.3 m with a phase speed of -0.86 m s^{-1}. Given this phase speed and the seaward drift of the boat (1.6 m s^{-1}), an apparent wavelength of 22 m is

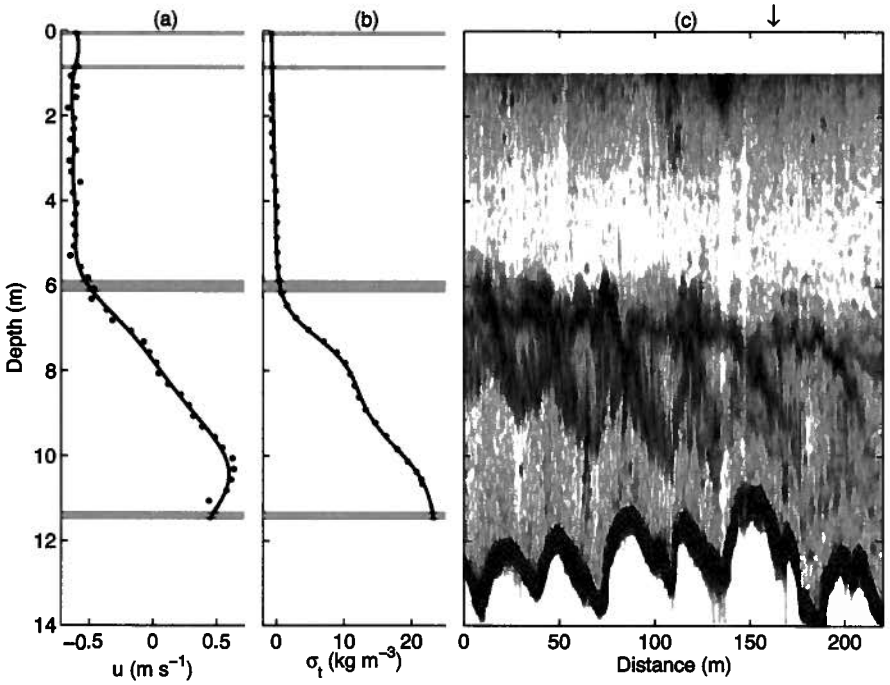

Figure 3.7: Velocity (a) and density (b) profiles observed during transect 3 (June 21, 2006, 12h38 PDT, 2.66 km upstream of Sand Heads). See figure 3.5 for details. In this case, the velocity is averaged over approximately 30 m.

calculated. This is very similar to the wavelength of the largest instability in figure 3.8c. This mode has a maximum displacement at a depth of 2.5 m, closely matching the location of the observed instabilities.

For these profiles there is a second, weaker, unstable mode located at a depth of 10.8 m. This mode is associated with the inflection point ($d^2U/dz^2 = 0$) in the velocity profile at this depth. Similar to the case in transect 1 (figure 3.5), the absence of strong vertical density gradients prevents us from confirming or denying the presence of this mode in the echosounding.

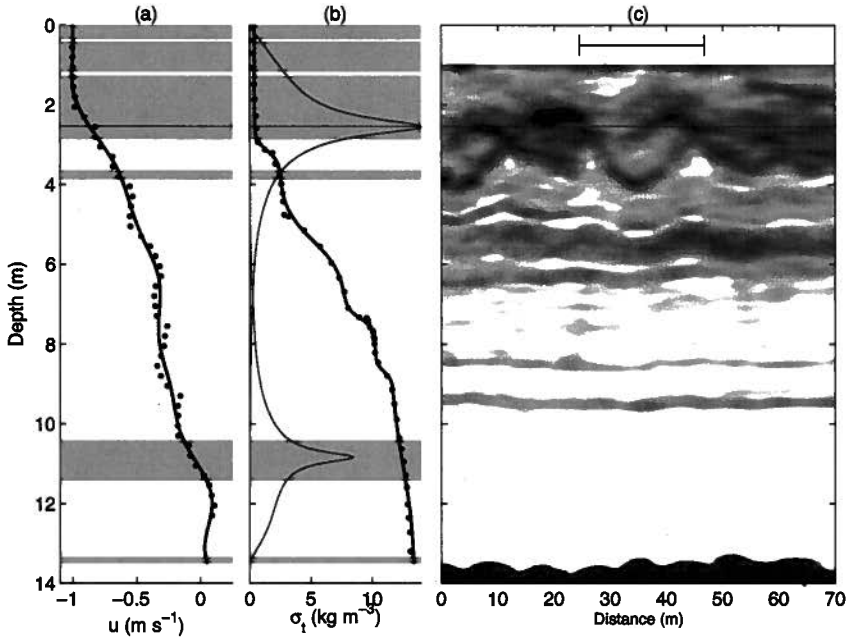

Figure 3.8: Velocity (a) and density (b) profiles observed during transect 4 (March 10, 2008, 11h20 PDT, 22.4 km upstream of Sand Heads). See figure 3.5 for details. In this case, the velocity is averaged over approximately 90 m.

Mid Ebb During Low Discharge: Transect 5

The instabilities in figure 3.9c were observed one hour later and approximately 3 km downstream from Transect 4. The ρ profile (figure 3.9b) again displays a number of layers consisting of high-gradient steps. However, the layers are not evident in the measured velocity profile (figure 3.9a), as was the case in figure 3.8, and the overall shape of the velocity profile is more linear.

The CTD cast is one of the few collected during the study where the instrument passed through an overturn in the pycnocline (depth of approximately 3.8 m). Consistent with the small amplitude of the instabilities in the echosounder, the overturn in the density profile has only water of intermediate density, i.e. no surface or bottom water is observed in the overturn.

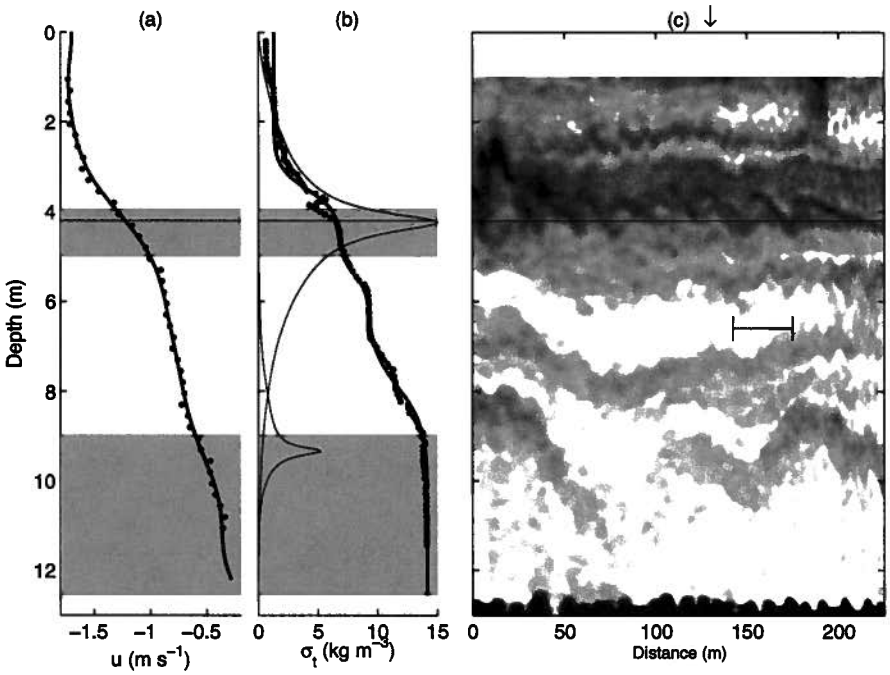

Figure 3.9: Velocity (a) and density (b) profiles observed during transect 5 (March 10, 2008, 12h21 PDT, 19.6 km upstream of Sand Heads). See figure 3.5 for details. In this case, the velocity is averaged over approximately 140 m.

The TG equation predicts an unstable mode with a peak growth rate (0.03 s^{-1}) at a wavelength of 14 m with a phase speed of -1.2 m s^{-1}. The apparent wavelength is predicted to be 32 m, whereas the features in the echosounder range in horizontal length from approximately 10 to 50 m, with the largest being near the TG prediction ($\approx$ 30 m). The predicted maximum in the displacement eigenfunction occurs at a depth of 4.2 m closely matching the depth of the instabilities.

As in the cases in figures 3.5 and 3.8, a second, weaker mode occurs near the bottom of the profile at a depth of 9.4 m. Again, this mode is associated with an inflection point in the velocity profile.

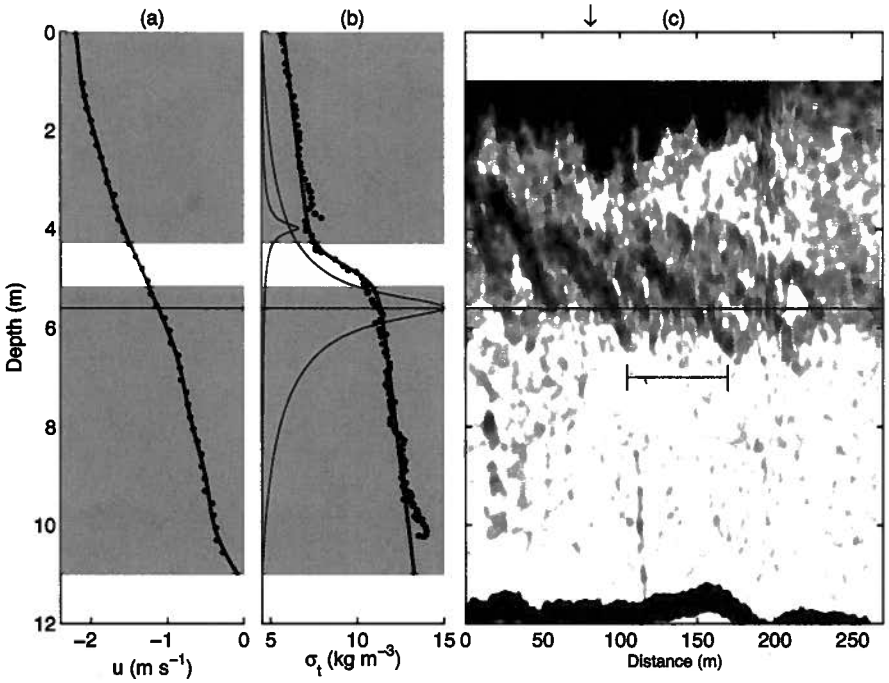

Figure 3.10: Velocity (a) and density (b) profiles observed during transect 6 (March 10, 2008, 14h34 PDT, 7.6 km upstream of Sand Heads). See figure 3.5 for details. In this case, the velocity is averaged over approximately 130 m.

Late Ebb During Low Discharge: Transect 6

In the later stages of the ebb, during transect 6 (figure 3.10), the shear has increased such that J is reduced to approximately 0.3. Unlike most of the other profiles collected during low or high discharge the density profile has no homogeneous layers, and shows small scale (i.e. on the scale of the instrument resolution) overturning throughout the depth. In these profiles Ri is below critical throughout most of the depth aside from at the density interface.

The most unstable mode predicted with the TG equation is located at a depth of 5.6 m and has a maximum growth rate of 0.019 s^{-1} at an apparent wavelength of 65m. This is close to, but longer than, the largest features in

the echosounder (approximately 50 m).

3.6 Small Scale Overturns and Bottom Stress

In figure 3.10 there are no features in the echosoundings that are associated with the small scale overturns in ρ below a depth of 7 m, and although our solutions to the TG equation suggest unstable modes, these are both located well above a depth of 7 m. To further examine the source of these overturns we compare selected density profiles from each of the low discharge transects (figure 3.11). In the density profile from transect 4, small scale overturns are rare or completely absent (figure 3.11, T4). Approximately two hours later, during transect 5, just one profile exhibits these small scale overturns (figure 3.11, T5). This cast was performed at the shallow constriction in the river associated with the Massey Tunnel (figure 3.4b 18 km). In this case the small scale overturns in the profile occur only below the pycnocline suggesting that the stratification within the pycnocline is confining the overturns to the lower layer. By maximum ebb, small scale overturns occur throughout the depth (figure 3.11, T6).

The presence of these small scale overturns is apparent, although not immediately obvious, in the echosoundings in figure 3.4. Note that the scale of the shading is the same in all three panels of figure 3.4 and that there is a gradual increase (darkening) in background echo intensity from early to late ebb (transects 4 to 6). This increase in echo intensity is attributed to the small scale overturning observed in the density profiles. Early in the ebb the dark shading associated with high echo intensity is concentrated at the density interfaces (transect 4). Otherwise, at this time, echo intensity is low (light shading) corresponding to an absence of small scale overturns in the density profiles (e.g. figure 3.11, T4). At this stage of the ebb, near-bottom velocities are close to zero and bottom stress is expected to be negligible. In transect 5 (figure 3.4b) there is an increase in echo intensity as the flow passes over the Massey Tunnel (18 km). At this location and during this stage of the ebb, near bottom velocity increases to approximately 0.2 m s^{-1} at 1 m above the bed. In this case the small scale overturns in the profile occur only below the pycnocline (figure 3.11 T5) suggesting that the stratification within the pycnocline is confining bottom generated turbulence to the lower layer. Near maximum ebb, during transect 6, near bottom velocities reach 0.5 m s^{-1} at 1 m above the bed. By this stage, high echo intensity and small scale overturns occur throughout the depth (figure 3.11, T6) suggesting that bottom generated turbulence has reached the surface despite the presence

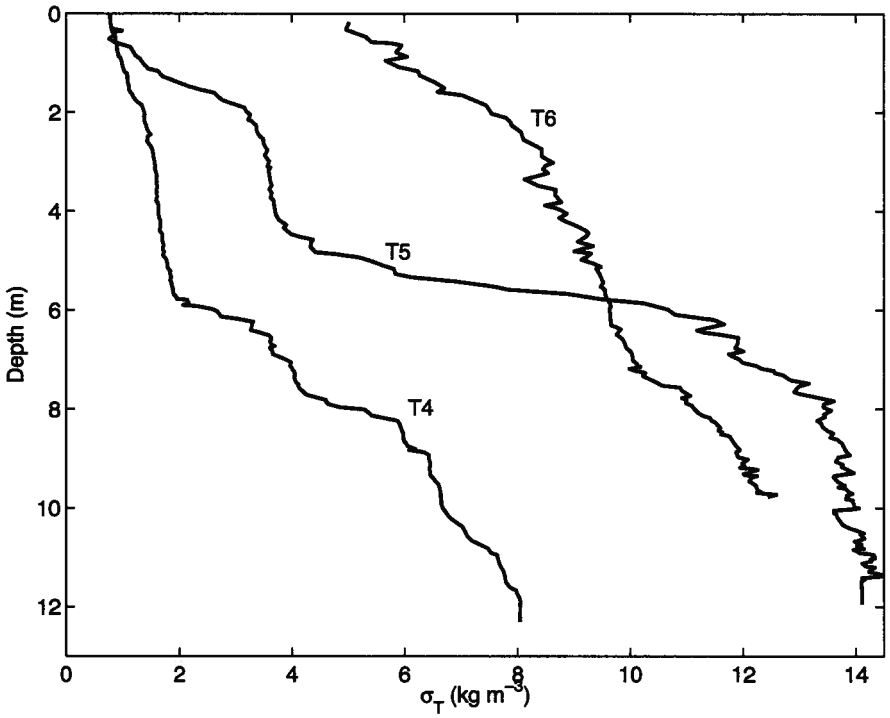

Figure 3.11: Selected density profiles from transects performed at low freshwater discharge. The profiles were collected at t=10h53, 12h36 and 14h25, at x=26.2, 17.9 and 8.8 km (transects 4, 5 and 6 respectively).

of stratification.

3.7 Discussion

One-Sided Instability

In all five of the cases that the TG equation predicted the occurrence of unstable modes, the bulk Richardson number, J, was greater than 1/4. This result suggests the mixing layer model and associated J (see section 3.4.3) are not adequate for describing the stability of the measured profiles. In all of these unstable cases, both the region of $Ri(z) < 1/4$ and the depth of the maximum in the displacement eigenfunction ($|\hat{\eta}(z)|$) were vertically

offset from the maximum gradient in density ($d\rho/dz$). This offset between the depth of the predicted region of instability and the density interface is due to asymmetry between the ρ and U profiles, i.e. deviations from the idealized profiles of the simple mixing layer model (equation 3.2 with $R = h/\delta = 1$).

Laboratory models and direct numerical simulations of asymmetry result in one-sided instabilities that resemble the features in the echosoundings in figures 3.5c, 3.6c and 3.8c [e.g. Lawrence *et al.*, 1991; Yonemitsu *et al.*, 1996; Carpenter *et al.*, 2007]. Similar observations were made in the Strait of Gibraltar by Farmer & Armi [1998] and in a strongly stratified estuary by Yoshida *et al.* [1998]. In both of these cases the instabilities were attributed to one-sided modes. One-sided modes are part of a general class of instability that includes the Holmboe mode. In contrast to the classic KH mode, the Holmboe mode is a result of the destabilizing influence of the density interface and can occur at relatively high values of J [Holmboe, 1962].

When these one-sided instabilities are modelled using DNS, at the values of J observed here, they lack the complete overturning of the density interface normally associated with KH billows. Unlike the mixed fluid that results from the KH instability, the mixed fluid that results from one-sided instabilities is not concentrated at the density interface, but, is instead drawn away from the density interface [Carpenter *et al.*, 2007].

Amplitude of the Instabilities

Unlike KH instabilities, the deflection of the density interface caused by one-sided instabilities does not necessarily equal the amplitude of the billows. It is therefore difficult to assess the amplitude of these instabilities using echosoundings (e.g. figure 3.5). Nevertheless, taking the approximate distance between the trough and the crest, the observed instabilities vary in height (twice the amplitude) from approximately 0.5 m to 2 m. The maximum height to wavelength aspect ratio of the observed instabilities varies between approximately 0.025 (0.5/20, figure 3.5c) and 0.1 (2/20, figure 3.6c). In the tilting tube experiments of Thorpe [1973] the maximum aspect ratio of KH instabilities varied between 0.05 and 0.6. Given the low values of J ($< 1/4$) in Thorpe's experiment this difference in aspect ratio is not surprising. Unfortunately, other than the case of the KH instability (symmetric density and velocity profiles and $J < 1/4$) the height of shear instabilities in stratified flows is not well documented.

Use of Echosoundings to Identify Instability

In section 3.5 our analysis focused on periods when instabilities were evident in the echosoundings. There were instances where the predictions from the TG equation suggested instabilities would occur when there were none visible in the echosounder. For example, in figures 3.5, 3.8 and 3.9 there are no apparent instabilities in the echosoundings associated with the weaker unstable modes. In these cases, this is explained by the absence of strong variations in salinity and temperature (i.e. density stratification) that are responsible for the back scatter of sound to the instrument [see Seim, 1999; Lavery *et al.*, 2003, for a thorough description of acoustic scattering in similar environments].

There was one notable case where the TG equation predicted an unstable mode in the presence of stratification while there was no clear evidence of instabilities in the echosoundings. For profiles collected at 2.2 km, during transect 3 (figure 3.3 c), the TG equation predicted instability close to the depth of the pycnocline (results not shown). In this region the boat speed and predicted instability speed were almost the same (-0.28 m s^{-1} versus -0.24 m s^{-1}). Considering equation 3.3, the resulting apparent wavelength would be 250 m. The corresponding apparent period of approximately 15 minutes (250 m / -0.28 m s^{-1}) would likely distort the appearance of an instability beyond recognition. This highlights an important challenge in identifying instabilities in echosoundings: if the point of observation is moving at a speed similar to the instability, the appearance of the instability becomes greatly distorted. On the other hand, if the observer is moving at a much different velocity than the instability, i.e. the apparent wavelength and period are relatively short, the sampling rate of the echosounder may not be sufficient to resolve the instabilities.

3.8 Conclusions

We successfully conducted a field program in the Fraser River estuary aimed at studying the details of shear instabilities. A bulk stability analysis showed the flow was least stable during mid and late ebb, consistent with the findings of previous investigators. Performing a detailed stability analysis on six sets of velocity and density profiles using the Taylor-Goldstein equation and comparing with the echosoundings we conclude the following.

1. All of the instabilities observed in the echosoundings coincided with the most unstable mode in the TG analysis. This confirms the appli-

cability of the TG equation in predicting instability, even in cases as complex as the Fraser River estuary.

2. The location of each of the observed instabilities occurs in a region of depth where $Ri < 1/4$. However, there are also cases that have $Ri < 1/4$ in which no unstable modes were observed. This result is in full agreement with the Miles-Howard criterion, but also highlights the inconclusive nature of this criterion .

3. Although the observed instabilities all involve the mixing of a well defined density interface, they appear to be concentrated on only one side of the interface. The maximum of $|\hat{\eta}|$ occurs either above or below the density interface in a region of z where $Ri < 1/4$. None of the observations show $Ri < 1/4$ *across* the width of a density interface. This is in contrast to the archetypal KH instability described by the simple mixing layer model, in which $Ri < 1/4$ where $d\rho/dz$ (N^2) is greatest. The observed instabilities might therefore be better described by the so-called 'one-sided' modes of Lawrence *et al.* [1991]; Carpenter *et al.* [2007], or the layered model of Caulfield [1994]; Lee & Caulfield [2001].

4. When there is active bottom generated turbulence in the water column, as in figure 3.10, we observe regions of z with near linear gradients in U and ρ and $Ri \lesssim 1/4$. In other stratified estuaries with moderate to strong tidal forcing, such as the Columbia and Hudson rivers, turbulence generated at the bottom is considered the dominant source of mixing [Nash *et al.*, 2008; Peters & Bokhorst, 2000]. The common occurrence of overturning caused by bottom generated turbulence in the late ebb of the present study suggests that this mixing process may be important in the Fraser River estuary.

Bibliography

ALEXAKIS, A. 2005 On Holmboe's instability for smooth shear and density profiles. *Phys. Fluids* **17**, 084103.

CARPENTER, J.R., LAWRENCE, G.A. & SMYTH, W.D. 2007 Evolution and mixing of asymmetric Holmboe instabilities. *J. Fluid Mech.* **582**, 103–132.

CAULFIELD, C.P. 1994 Multiple linear instability of layered stratified shear flow. *J. Fluid Mech.* **258**, 255–285.

FARMER, D.M. & ARMI, L. 1998 The flow of Atlantic water through the Strait of Gibraltar. *Prog. Oceanogr.* **21**, 1–98.

GEYER, W.R. & FARMER, D.M. 1989 Tide-induced variation of the dynamics of a salt wedge estuary. *J. Phys. Oceanogr.* **19**, 1060–1672.

GEYER, W.R. & SMITH, J.D. 1987 Shear instability in a highly stratified estuary. *J. Phys. Oceanogr.* **17**, 1668–1679.

GOLDSTEIN, S. 1931 On the stability of superposed streams of fluids of different densities. *Proc. R. Soc. Lond. A* **132**, 524–548.

HAZEL, P. 1972 Numerical studies of the stability of inviscid stratified shear flows. *J. Fluid Mech.* **51**, 39–61.

HOLMBOE, J. 1962 On the behavior of symmetric waves in stratified shear layers. *Geofys. Publ.* **24**, 67–112.

HOWARD, L.N. 1961 Note on a paper of John W. Miles. *J. Fluid Mech.* **10**, 509–512.

KOSTACHUK, R.A. & ATWOOD, L.A. 1990 River discharge and tidal controls on salt-wedge position and implications for channel shoaling: Fraser River British Columbia. *Can. J. Civil Eng.* **17**, 452–459.

LAVERY, A.C., SCHMITT, R.W. & STANTON, T.K. 2003 High-frequency acoustic scattering from turbulent oceanic microstructure: The importance of density fluctuations. *J. Acoust. Soc. Am.* **114** (5), 2685–2697.

LAWRENCE, G.A., BROWAND, F.K. & REDEKOPP, L.G. 1991 The stability of a sheared density interface. *Phys. Fluids* **3** (10), 2360–2370.

LEE, V. & CAULFIELD, C.P. 2001 Nonlinear evolution of a layered stratified shear flow. *Dyn. Atmos. Oceans* **24**, 173–182.

MACDONALD, D.G. & HORNER-DEVINE, A.R. 2008 Temporal and spatial variability of vertical salt flux in a highly stratified estuary. *J. Geophys. Res.* **113**.

MILES, J.W. 1961 On the stability of heterogeneous shear flows. *J. Fluid Mech.* **10**, 496–508.

MILES, J.W. 1963 On the stability of heterogeneous shear flows. part 2. *J. Fluid Mech.* **16**, 209–227.

MOUM, J.N., FARMER, D.M., SMYTH, W.D., ARMI, L. & VAGLE, S. 2003 Structure and generation of turbulence at interfaces strained by internal solitary waves propagating shoreward over the continental shelf. *J. Phys. Oceanogr.* **33**, 2093–2112.

NASH, J.D., KILCHER, L. & MOUM, J.N. 2008 Turbulent mixing in the Columbia River Estuary: structure and consequences for plume composition. *J. Geophys. Res.* p. submitted.

PETERS, H. & BOKHORST, R. 2000 Microstructure observations of turbulent mixing in a partially mixed estuary. part 1: Dissipation. *J. Phys. Oceanogr.* **30** (6), 1232–1244.

SEIM, H.E. 1999 Acoustic backscatter from salinity microstructure. *J. Atmos. Ocean. Technol.* **16**, 1491–1498.

SEIM, H.E. & GREGG, M.C. 1994 Detailed observations of naturally occurring shear instability. *J. Geophys. Res.* **99** (C5), 10049–10073.

TAYLOR, G.I. 1931 Effect of variation in density on the stability of superposed streams of fluid. *Proc. R. Soc. Lond. A* **132**, 499–523.

THORPE, S.A. 1973 Experiments on instability and turbulence in a stratified shear flow. *J. Fluid Mech.* **61**, 731–751.

THORPE, S.A. 2005 *The Turbulent Ocean*, 1st edn. Cambridge University Press.

WARD, P.R.B. 1976 Seasonal salinity changes in the Fraser River Estuary. *Can. J. Civil Eng.* **3**, 342–348.

YONEMITSU, N., SWATERS, G.E., RAJARATNAM, N. & LAWRENCE, G.A. 1996 Shear instabilities in arrested salt-wedge flows. *Dyn. Atmos. Oceans* **24**, 173–182.

YOSHIDA, S., OHTANI, M., NISHIDA, S. & LINDEN, P.F. 1998 Mixing processes in a highly stratified river. In *Physical Processes in Lakes and Oceans*, *Coastal and Estuarine Studies*, vol. 54, pp. 389–400. American Geophysical Union.

Chapter 4

Holmboe Wave Fields in Simulation and Experiment [3]

4.1 Introduction

Geophysical flows often exhibit stratified shear layers in which the region of density variation is thinner than the thickness of the shear layer [e.g. Armi & Farmer, 1988; Wesson & Gregg, 1994; Yoshida *et al.*, 1998, Chapter 3]. In these circumstances, when the stratification is sufficiently strong (measured by an appropriate Richardson number), Holmboe's instability develops. At finite amplitude the instability is characterized by cusp-like internal waves (referred to herein as Holmboe waves) that propagate at equal speed and in opposite directions with respect to the mean flow. Accurate modelling of these instabilities is important for the correct parameterization of momentum and mass transfers occurring in flows of this nature.

Previous studies on the nonlinear behaviour of Holmboe waves have adopted one of two methods: either an experimental approach in which the instability is studied under specified laboratory settings [Zhu & Lawrence, 2001; Hogg & Ivey, 2003], or a numerical approach that allows for a detailed description of the flow in an idealized stratified mixing layer [Smyth *et al.*, 1988; Smyth & Winters, 2003; Smyth, 2006; Smyth *et al.*, 2007]. It is difficult to make a meaningful comparison of laboratory and numerical results for a number of reasons. In the case of laboratory experiments, Holmboe waves often arise as a local feature of a larger-scale flow, such as an exchange flow between two basins of different density [Pawlak & Armi, 1996; Zhu & Lawrence, 2001; Hogg & Ivey, 2003], or an arrested salt wedge flow [Sargent & Jirka, 1987; Yonemitsu *et al.*, 1996]. In many of these experiments the mean flow varies appreciably over length scales that are comparable to the wavelength of the waves. For this reason, it can be difficult to isolate the dynamics of the waves from that of the mean flow.

[3] This chapter is in preparation for publication in: J.R. Carpenter, E. W. Tedford, M. Rahmani and G.A. Lawrence (2009), Holmboe Wave Fields in Simulation and Experiment.

The use of numerical simulations has been advantageous in this regard, and comprises a great majority of the literature on the nonlinear dynamics of Holmboe waves. The first verification of two oppositely propagating cusp-like waves of equal amplitude, predicted by the Holmboe [1962] theory, was made through the numerical simulations of Smyth *et al.* [1988]. Since then, increases in computational resources have led to fully three-dimensional direct numerical simulations (DNS) of Holmboe waves that resolve the smallest scales of variability. These simulations have been used to understand turbulence and mixing characteristics (Smyth & Winters 2003; Smyth, Carpenter & Lawrence 2007; Carpenter, Lawrence & Smyth 2007), as well as the growth of secondary circulations and the transition to turbulence [Smyth, 2006]. However, partly due to computational constraints, only a single wavelength of the primary instability has been reported in the literature. Furthermore, no attempt has been made to compare the results of numerical simulations with laboratory experiments.

In this paper, we undertake a combined numerical and experimental study of Holmboe waves. The experiments, originally described by Tedford, Pieters & Lawrence (2009) (Chapter 2), consist of an exchange flow through a relatively long channel with a rectangular cross-section. The experimental design allows for a detailed study of the Holmboe wave field within a steady mean flow that exhibits gradual spatial variation relative to the wave properties. The DNS of the present study were designed to correspond as closely as possible to the conditions present in the experiments to effect a meaningful comparison between the two methods. To our knowledge, this is the first study to compare experimental and numerical results, as well as the first to perform DNS for multiple wavelengths of the instability. We focus on comparing basic descriptors of the wave fields such as phase speed, wavenumber, and wave amplitude, in order to gain a fuller understanding of the processes affecting the nonlinear behaviour of the waves.

The paper is organized as follows. Section 4.2 gives a background on the stability of stratified shear flows. This is followed by a description of the numerical simulations, and laboratory experiments in section 4.3. We then discuss comparisons between the simulations and experiments in terms of the basic wave structure (section 4.4), phase speed (section 4.5), wave spectral evolution (section 4.6), and wave amplitude and growth (section 4.7). Conclusions are stated in the final section.

4.2 Linear Stability of Stratified Shear Layers

In both experiment and simulation, the mean flow exhibits the characteristics of a classic stratified shear layer. The velocity profile undergoes a total change of ΔU, over a length scale h, that is closely centred with respect to the density interface. Similarly, the density profile changes by $\Delta\rho$ between the two layers, over a scale of δ. This suggests using an idealized model of the horizontal velocity and density profiles that is given by

$$U(z) = \frac{\Delta U}{2}\tanh\left[\frac{2(z-z_0)}{h}\right] \quad \text{and} \quad \bar{\rho}(z) = \rho_0 - \frac{\Delta\rho}{2}\tanh\left[\frac{2(z-z_0)}{\delta}\right], \tag{4.1}$$

respectively. The density profile $\bar{\rho}(z)$ is measured relative to a reference density ρ_0, with z the vertical coordinate. A necessary condition for the growth of Holmboe's instability is that the thickness ratio $R \equiv h/\delta \gtrsim 2$ [Alexakis, 2005].

In addition to R, we may define three more important dimensionless parameters

$$Re \equiv \frac{\Delta U h}{\nu}, \quad J \equiv \frac{g'h}{(\Delta U)^2}, \quad \text{and} \quad Pr \equiv \frac{\nu}{\kappa},$$

where $g' = \Delta\rho g/\rho_0$ is the reduced gravitational acceleration, ν is the kinematic viscosity, and κ the diffusivity of the stratifying agent. These are the Reynolds, bulk Richardson, and Prandtl numbers, respectively.

Linear stability analysis of the profiles in (4.1) has been performed in numerous studies [e.g. Hazel, 1972; Smyth *et al.*, 1988; Haigh, 1995]. For the flows considered here, the effects of viscosity and mass diffusion have been included. The resulting equation is a sixth order eigenvalue problem originally described by Koppel [1964]. Like the better known Taylor–Goldstein equation, Koppel's equation gives predictions of the complex phase speed $c = c_r + ic_i$, and vertical mode shape, as a function of wavenumber k. Results of the stability analysis are shown in figure 4.1, which includes the temporal growth rate, kc_i, as well as the dispersion relation in terms of phase speed $c_r(k)$, and frequency $\sigma(k)$. This is done for the idealized profiles (4.1) using $Re = 630$, $J = 0.30$, $Pr = 700$, and $R = 8$, matching the conditions in the laboratory exchange flow (thick lines). As discussed in the next section, computational constraints limited our three-dimensional DNS to a $Pr = 25$ and $R = 5$, resulting in slightly different results (figure 4.1, thin lines). Although no appreciable changes are seen in the predicted phase speed c_r and frequency σ, there are differences in maximum growth rate and the location

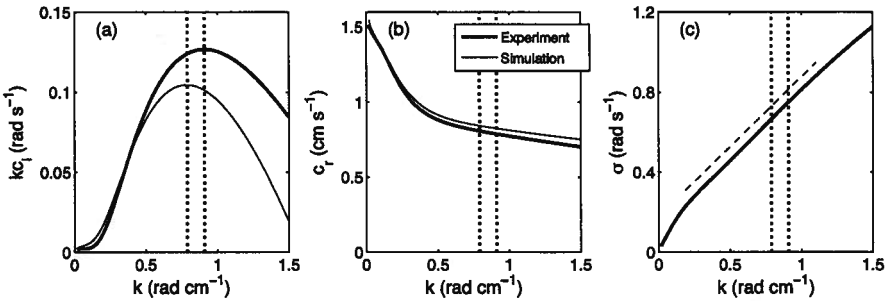

Figure 4.1: Plots of (a) growth rate kc_i, (b) phase speed c_r, and (c) frequency σ of the profiles in (4.1). Conditions in the experiment are shown as thick lines, and the three-dimensional simulation at $Pr = 25$ and $R = 5$ as thin lines. No noticeable difference between the simulation and experiment can be seen in (c). The location of the wavenumber of maximum growth in each case is marked with a vertical dotted line. The dashed line in (c) indicates $\sigma \propto k$.

of the wavenumber of maximum growth k_{max}.

4.3 Methods

4.3.1 Description of the Numerical Simulations

Numerical simulations were performed using the DNS code described by Winters, MacKinnon & Mills (2004), which has been modified to include greater resolution of the density scalar field by Smyth, Nash & Moum (2005). The simulations were designed to reproduce conditions present in the laboratory experiment as closely as possible, while still conforming to the general methodology used in recent investigations of nonlinear Holmboe waves [Smyth & Winters, 2003; Smyth, 2006; Smyth *et al.*, 2007; Carpenter *et al.*, 2007].

The boundary conditions are periodic on the streamwise (x) and transverse (y) boundaries, and free-slip on the vertical (z) boundaries. Simulations are initialized with profiles in the form of (4.1) that closely match what is observed in the experiment. Figure 4.2 shows a sequence of representative U and $\bar{\rho} - \rho_0$ profiles at three different times during a simulation, as well as profiles from the experiment for comparison. The periodic boundary conditions of the simulations cause the flow to 'run down' over time, i.e.

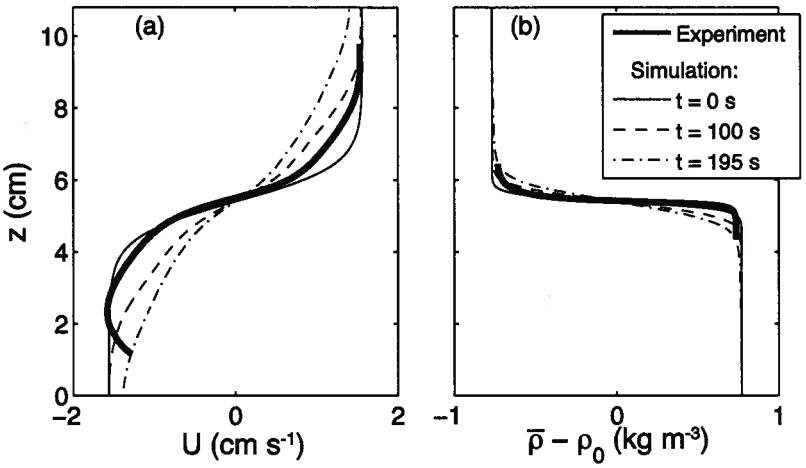

Figure 4.2: Evolution of the background profiles in both simulation and experiment. Plots (a) and (b) show temporal changes to $U(z)$ and $\bar{\rho}(z) - \rho_0$ profiles in the simulation with experimental profiles taken from the channel centre ($x = 0$) in thick lines overlain for comparison.

there is a continual loss of kinetic energy from the shear layer due to viscous dissipation and mixing. This results in an increase of h and δ over time, as can be seen in figure 4.2. To indicate conditions at the initial time step ($t = 0$ s) of the simulations we will use a zero subscript (e.g. h_0).

In order to initiate growth of the primary Holmboe instability, the flow is perturbed with a random velocity field at the first time step. The noise is distributed evenly in the x, y directions, but given greater amplitude near the centre of the shear layer and density interface, in the same manner as Smyth & Winters [2003]. The amplitude of the random perturbation was chosen large enough such that the instability grows to finite amplitude with minimal diffusion of the background profiles, yet is still small enough to satisfy the conditions for numerical stability.

While an ideal comparison between simulation and experiment would involve matching all four of the relevant dimensionless parameters, we are constrained by the high computational demands of DNS. Of particular difficulty is the fine grid resolution required for high Pr flows. For this reason we have chosen a $Pr = 25$, opposed to $Pr = 700$ for the laboratory salt stratification. Large values of R also place a high demand on the computa-

		Parameters				Linear Theory		Results
		Pr	R	L_x (cm)	L_y (cm)	k_{max} (rad cm^{-1})	c_r (cm s^{-1})	a_{rms} (cm)
Laboratory		700	8	200	10	0.91	0.79	0.31 (0.51-0.84)
Simulations								
I	(3D)	25	5	128	5	0.79	0.84	0.62
II	(2D)	700	8	64	0	0.91	0.79	0.48
III	(3D)	25	5	64	10	0.79	0.84	0.62
IV	(2D)	25	5	64	0	0.79	0.84	0.74

Table 4.1: Values of the various important dimensionless parameters for both the simulation and experiment. The parameters listed in the simulation are evaluated using the initial conditions. In all cases we have $J_0 = 0.3$, $Re_0 = 630$, and $L_z = 10.8$ cm. Also included are k_{max} and c_r from the results of the linear stability analysis, and the root mean square saturated amplitude observations. The bracketed value of a_{rms} is for the laboratory experiments with the effect of wave stretching taken into account.

tional resources, and we have therefore chosen $R_0 = 5$, opposed to the $R = 8$ observed in the experiments. The effects of Pr and R have been tested by performing a two-dimensional simulation (II) at $Pr = 700$ and $R_0 = 8$. The remaining two parameters, $Re_0 = 630$ and $J_0 = 0.30$, have been matched to the experimental values. Computational constraints also limit the size of the simulation domain. In all cases the vertical depth L_z, has been matched to the 10.8 cm of the experiments. The simulation width $L_y = 5$ cm, has been reduced to half of that in the experiment ($L_y = 10$ cm), but was not found to effect the results presented. This reduction in the width of the computational domain enabled a larger length $L_x = 128$ cm, allowing for approximately 16 wavelengths of the most amplified mode, and compares well with the $L_x = 200$ cm in the experiment. A summary of the parameters in the experiment and the simulations is shown in table 4.1.

In addition to the three- and two-dimensional simulations already mentioned (labeled I and II in table 4.1, respectively), two supplementary simulations (III and IV) were also performed to test the effects of L_y and R, Pr. Unless explicitly stated, we will refer to simulation I simply as 'the simulation', hereafter.

4.3.2 Description of the Laboratory Experiment

The laboratory experiment was performed in the exchange flow facility described by Tedford *et al.* [2009] (Chapter 2). A complete discussion of the experimental procedures and apparatus can be found in that study, however, we now provide a summary of the pertinent features.

The apparatus consists of two reservoirs connected by a rectangular channel 200 cm in length, and 10 cm in width. The reservoirs are initially filled with fresh and saline water ($\Delta\rho = 1.41$ kg m^{-3}) such that the depth in the channel is 10.8 cm. A bi-directional exchange flow is initiated by the removal of a gate from the centre of the channel. After an initial transient period in which gravity currents propagate to each reservoir, and mixed interfacial fluid is advected from the channel, the flow enters a period of steady exchange where the density interface is found to display an abundance of Holmboe wave activity. In contrast to the run-down conditions in the DNS, the storage of unmixed water in the reservoirs maintains a steady exchange flow for approximately 600 s. Our comparison is restricted to instabilities observed during the period of steady exchange.

The exchange flow exhibits internal hydraulic controls at the entrance to each of the reservoirs, effectively isolating the channel from disturbances in the reservoirs, and enforcing radiation boundary conditions at the channel ends. Friction between the layers leads to a gradually sloping density interface that produces an x-dependent mean velocity, $\bar{U} = (U_1 + U_2)/2$ (figure 4.3). The upper (U_1) and lower (U_2) layer velocities are the maximum and minimum free-stream velocities (see Chapter 2). The gradual variation of $\bar{U}(x)$ along the laboratory channel is a result of the acceleration in each of the layers due to the sloping interface. This variation is shown in figure 4.3(b), and is found to be a near-linear function of x for the central portion of the channel. In contrast, $\bar{U}$ is identically zero throughout the domain in the simulation, due to the periodic boundary conditions. This difference in mean flow is found to have important effects on the nonlinear development of the Holmboe wave field.

4.4 Wave Structure

In the first instance, it is beneficial to perform a simple visual comparison of the density structure of the waves. This is shown in figure 4.4, where a representative photograph of the laboratory waves is displayed above plots of the density field from the two-dimensional simulation II (figure 4.4b) and three-dimensional simulation I (figure 4.4c,d). The density structure in

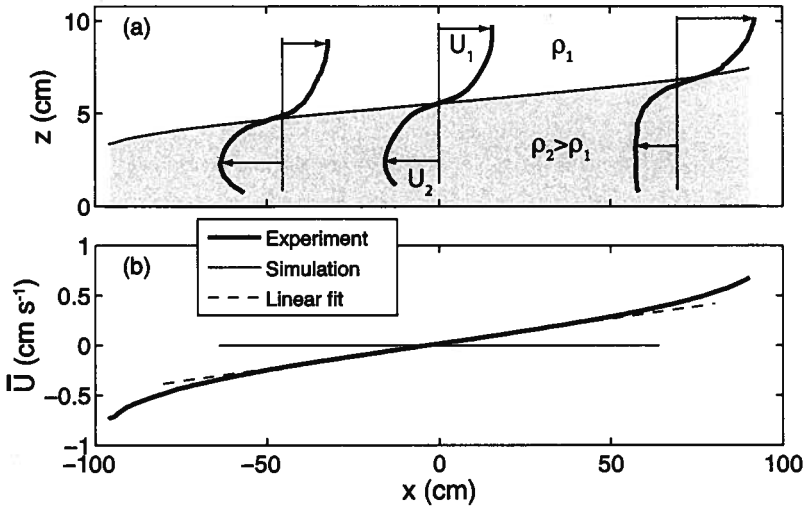

Figure 4.3: Spatial changes in $U(z)$ and layer depths that occur along the laboratory channel are shown in (a), along with the corresponding distribution of $\bar{U}(x)$ in (b). A linear fit to $\bar{U}(x)$ in the central portion of the channel is shown as the dashed line, and the mean velocity in the simulation domain is given by the thin solid line.

figures 4.4(a,b) is very similar, as each has an identical set of dimensionless parameters, differing only in the initial and boundary conditions. In all panels of figure 4.4 it can be seen that many of the waves display the typical form of the Holmboe instability, and consist of cusps projecting into the upper and lower layers. The upward pointing cusps are moving from left to right, in the same direction as the flow in the upper layer, while the downward cusps move at an equal but opposite speed with respect to the mean velocity. The waves do not always appear cusp-like, and many take a more sinusoidal form.

An important feature of nonlinear Holmboe waves is the occasional ejection of stratified fluid from the wave crests into the upper and lower layers. Two such ejections are shown in figure 4.4(d) where indicated, and can be characterized by thin wisps of fluid being drawn from the wave crest and advected by the mean flow. These wisps often settle back to the interface level, contributing to the accumulation of mixed fluid there. This accumulation is observed to a much greater extent in figure 4.4(c,d), and should

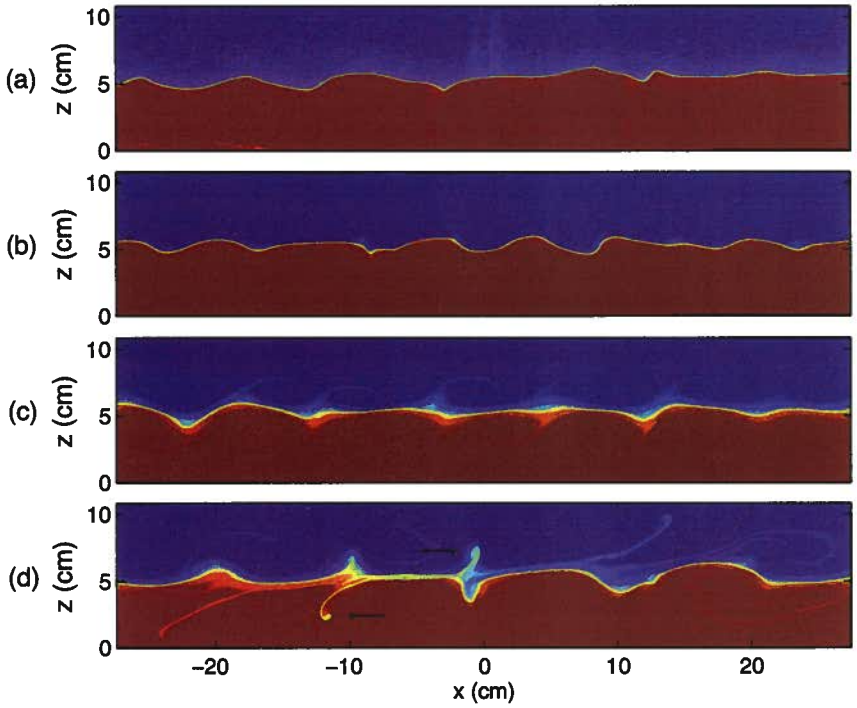

Figure 4.4: Representative plots of the density field for the experiment (a) along with simulation II (b), and simulation I (c,d). The plot in (d) is taken at a later time when two ejections are underway, indicated by arrows. The x-axis has been shifted by $L_x/2$ to the left in (d) to better display the ejection process.

be expected due to the larger value of R_0, as well as the higher diffusion that comes with the lower Pr used in this simulation. Although ejections are observed in both the laboratory experiment and high Pr,R simulation (II), there is a greater frequency of occurrence in the lower $Pr = 25$, $R = 5$ simulation (I).

Holmboe's instability has the uncommon property that, under certain conditions, the growth of the primary instability may take place as a three-dimensional wave. Such a wave would travel obliquely to the orientation of the shear, and produce significant departures from a two-dimensional wave. One of the conditions for this three-dimensional growth is that Re be

sufficiently low [Smyth & Peltier, 1990]. As the laboratory experiments are carried out at low Re, and show some variation in the spanwise direction, it must be questioned whether the growth of the primary Holmboe instability is three-dimensional. This is easily tested by the simulation results, which show a clear two-dimensional growth (see section 4.7 as well), even to an initially random perturbation as described above. We can therefore confirm that the primary instability is two-dimensional for the conditions examined in the present study.

4.5 Phase Speed

Many of the basic features in the wave field are revealed by an $x - t$ characteristics diagram of the density interface elevation, shown in figure 4.5 for both the simulation and experiment. Although the interface consists of contributions from both upper and lower Holmboe wave modes (each travelling in opposite directions), we have filtered the characteristics using a two-dimensional Fourier transform to reveal only the upper, rightward propagating wave modes.

Certain differences between the simulation characteristics (figure 4.5a) and the experimental characteristics (figure 4.5b) are immediately apparent. The experimental characteristics exhibit a greater degree of irregularity. Since each plot represents a two dimensional slice from a three-dimensional field, this may be a result of greater variability in the transverse direction in the case of the experiments. Since the waves in the simulation develop from an initial random perturbation at $t = 0$, there is also a temporal growth of the average wave amplitude in figure 4.5(a) that is not present in the experimental characteristics.

Despite these apparent differences in the characteristics, the phase speeds (inferred from the slope of the characteristics) are in good agreement. The observed phase speeds in both the simulation and experiment are found to be slightly greater than the predictions of linear theory (solid lines), which has been noted in previous studies [Haigh, 1995; Hogg & Ivey, 2003]. However, the observations also suggest an increase in phase speed with wave amplitude. This is a quintessential feature of nonlinear wave behaviour (e.g. Stokes waves). Note that a 'pulsing' of the wave amplitude and phase speed is present in both sets of characteristics in figure 4.5. This is a well known feature of Holmboe waves due to the interaction between the two oppositely propagating modes [Smyth *et al.*, 1988; Zhu & Lawrence, 2001; Hogg & Ivey, 2003].

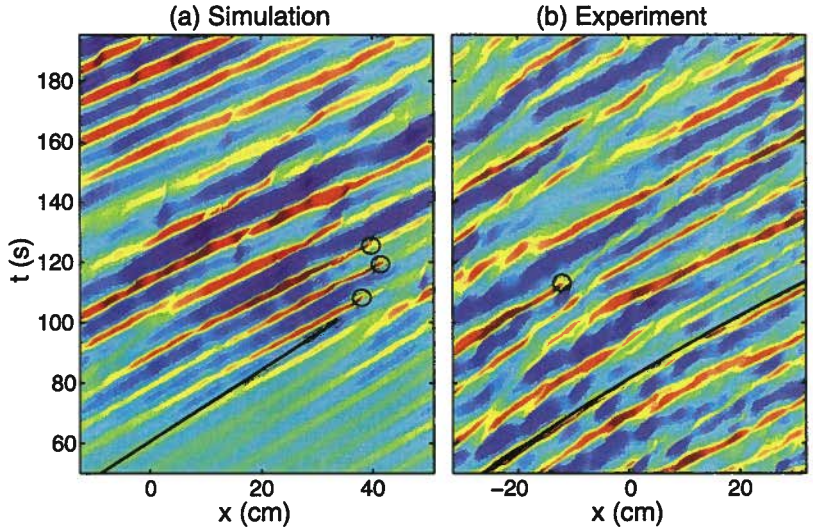

Figure 4.5: Rightward propagating wave characteristics for the simulation (a) and experiment (b). Shading represents the elevation of the density interface with red indicating a high (crest) and blue indicating a low (trough), and has been optimized in each of (a,b). Solid black lines indicate the characteristic slope given by the linear prediction of phase speed c_r. In the case of the laboratory experiment, the c_r has a slight curvature since the changes in $\bar{U}$ across the channel have been included. The dark circles indicate locations and times of ejections.

Sudden decreases in wave amplitude can be seen in both sets of characteristics at a number of times and locations. It is often the case (though not always) that these sudden amplitude changes are a result of the ejection process. Instances where ejections occur have been identified in figure 4.5, and are denoted by circles. It is generally observed that the ejection process preferentially acts on the largest amplitude waves, and in this way resembles a wave breaking mechanism.

4.6 Spectral Evolution

This section concerns the distribution and evolution of wave energy with k. It will be shown that there are two different processes acting separately in

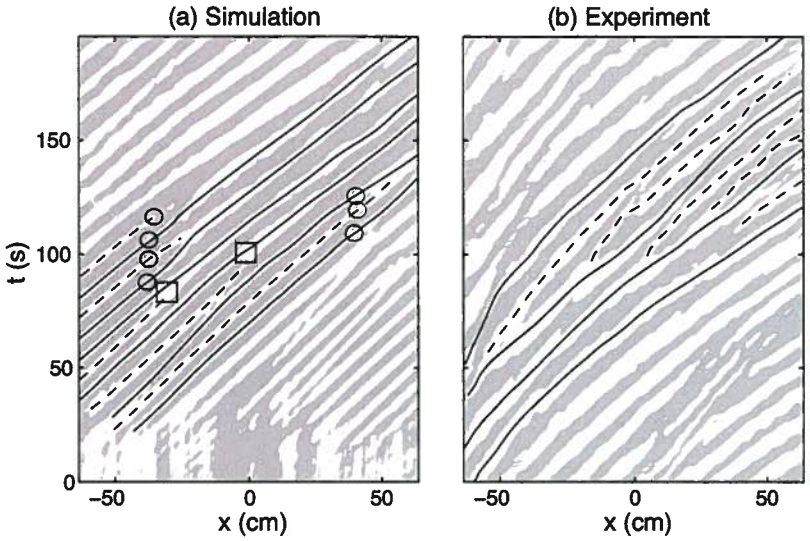

Figure 4.6: Rightward propagating wave characteristics for the simulation (a) and experiment (b). White indicates a wave crest while grey indicates a wave trough. In each panel a number of wave crests are indicated by solid and dashed lines. In (a), the dashed lines correspond to waves that are 'lost' over the duration of the simulation, whereas in (b), the dashed lines correspond to waves that have formed within the channel. Only the central portion of the laboratory channel corresponding to the simulation domain has been shown. Circles and squares indicate locations and times of ejections and pairing events, respectively.

the simulation and experiment that are responsible for a shifting of wave energy to lower k (i.e. longer waves).

4.6.1 Frequency Shifting

In order to gain an understanding of the wave spectrum, it is first useful to carefully examine the characteristic diagrams. Figure 4.6 shows rightward propagating characteristics from both simulation and experiment that highlight the location of wave crests (in white) and troughs (in grey). Characteristics from the simulation (figure 4.6a) are discussed first, and are shown for the entire computational domain.

Beginning with the initial random perturbation at $t = 0$, energy is ex-

tracted from the mean flow by the instability and fed into the wave field at, or very close to, the wavenumber of maximum growth, k_{max}. This results in approximately 16 waves in the computational domain (given by $L_x k_{max}/2\pi$) for early times. We see however, that as the simulation proceeds wave crests are continually being 'lost' over time. This feature is highlighted by the solid and dashed lines that are used to trace the wave crests in figure 4.6(a). The dashed lines indicate wave crests that are 'lost', while the solid lines correspond to crests that persist. This process of losing waves results in an observed frequency, ω, that is continually shifted downwards. Because previous numerical studies of Holmboe waves simulated only a single wavelength, this process has not been described before. This 'frequency downshifting' or 'wave coarsening' has, however, been noted previously in many other nonlinear wave systems [e.g. Huang *et al.*, 1999; Balmforth & Mandre, 2004].

It can be seen in figure 4.6(a) that three of the five lost waves indicated by dashed lines correspond to waves that have undergone ejections (indicated by circles). In general, for all of the simulations performed, the ejection process typically results in a loss of waves and a downshift in frequency. This observation mirrors similar findings in the frequency downshifting of nonlinear surface gravity waves, where the occurrence of wave breaking is related to lost waves [Huang *et al.*, 1996; Tulin & Waseda, 1999]. Close examination of the vorticity field also suggests that the Holmboe waves undergo a vortex pairing process. Although the pairing of adjacent vorticies is a well known feature of homogenous and weakly stratified shear layers [Browand & Winant, 1973], it has not previously been identified in Holmboe instabilities. This is an additional means to effect a shift of wave frequency, and is denoted by square symbols in figure 4.6(a).

In contrast, figure 4.6(b) shows that the experimental characteristics display a distinctly different behaviour. In this case, new wave crests are continually being formed as the waves traverse the channel. Again, this process is highlighted by the tracing of crests by solid and dashed lines. Now, the dashed lines represent new wave crests that have been formed within the channel. This process results in an increasing ω with x in the experiments.

Tedford *et al.* [2009] (Chapter 2) explain the formation of new waves as follows. As waves propagate through the channel they are accelerated by the increasing mean velocity $\bar{U}(x)$. This leads to a 'stretching' of the waves that decreases k from near k_{max}, where the waves initially formed, to lower values (i.e. longer wavelengths). Once a sufficiently low k is achieved, the Holmboe instability mechanism acts between the wave crests to form additional waves. This feeds energy back into the wave field near k_{max}, resulting in an average

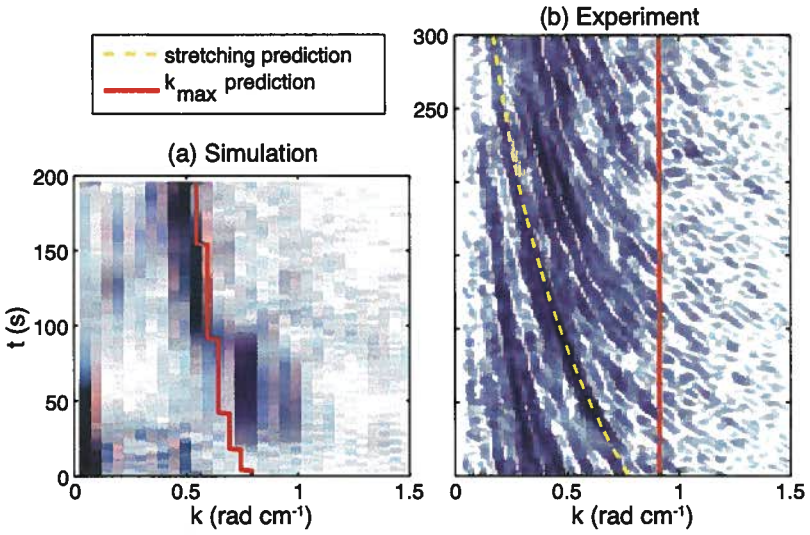

Figure 4.7: Spectral evolution of the rightward propagating waves from simulation (a) and experiment (b). Dark colours denote a high in energy which is proportional to the mean square amplitude of the interface displacement. The wave energy has been normalized by the variance in (a) to remove the time dependent wave growth. Linear stability theory is used to predict k_{max} (red lines), which changes in time for the simulations. The predicted stretching of wave energy in the experiment by $\bar{U}(x)$ to lower k is shown as the yellow dashed line in (b).

k that is constant across the channel, and an increasing ω.

The two processes, wave coarsening in the simulation, and wave stretching in the experiments, are best described quantitatively using wave spectra.

4.6.2 Wave Energy Spectra

Differences between the processes responsible for modifying k in the simulation and experiment can be seen in figure 4.7. It demonstrates how wave energy (indicated by the dark bands) is redistributed in k over time.

The spectra of the simulation (figure 4.7a), which has been normalized by the variance in order to remove the time-dependent growth of the waves, shows a discrete transfer of wave energy to lower k. The simulation spectra is required to evolve in discrete steps due to the periodic boundary conditions

(i.e. in wavenumber increments of $\Delta k = 2\pi/L_x$). As a point of comparison, the k_{max} prediction from linear stability theory is plotted in red. The predicted k_{max} has been discretized according to the boundary conditions, and decreases in time due to the diffusion of the background profiles, i.e. the increase in the shear layer thickness $h(t)$.

The spectral evolution plot (figure 4.7a) compliments the characteristics diagram of figure 4.6(a), showing an initial input of energy at $k_{max}(t = 0)$, and a subsequent shifting of that energy to lower k. It is interesting to note that the $k_{max}(t)$ curve shows the same general trend as the concentration of wave energy (shown by the dark 'blocks' in figure 4.7a). Although the details are unclear, we speculate that the shift in wave energy to lower k is the result of nonlinear processes such as the ejections and vortex pairing.

It is apparent from the wave spectra in figure 4.7(b) that the process responsible for the redistribution of wave energy in the experiments is a continuous one. Energy at any given time is found to be focused in a number of 'bands'. These bands originate near k_{max}, and move towards lower k in time. In addition, they all appear to have a similar trajectory in kt-space. Tedford *et al.* [2009] (Chapter 2) hypothesize that these bands are a result of the stretching of wave energy to lower k by $\bar{U}(x)$. We now formulate a simple model in order to quantify this hypothesis.

Wave Stretching Prediction

The changes in k that result from wave stretching by $\bar{U}(x)$ can be described by an application of gradually varying wave theory. This theory assumes that the density interface elevation $\eta(x,t)$, may be expressed in terms of a gradually varying amplitude $a(x,t)$, and a rapidly varying sinusoidal component *viz.*

$$\eta(x,t) = \mathrm{Re}\{a(x,t)\mathrm{e}^{\mathrm{i}\theta(x,t)}\}. \tag{4.2}$$

The local wavenumber and frequency are defined in terms of the phase function $\theta(x,t)$ by $k \equiv \partial\theta/\partial x$ and $\omega \equiv -\partial\theta/\partial t$, respectively. We assume, for the moment, that $\theta(x,t)$ is continuous. This implies that waves are conserved, giving

$$\frac{\partial k}{\partial t} + \frac{\partial \omega}{\partial x} = 0. \tag{4.3}$$

Recognizing that ω, which is the frequency that a stationary observer would measure, includes both an intrinsic portion $\sigma(k)$, and an advective portion $k\bar{U}$, leads to

$$\omega = \sigma(k) + k\bar{U}(x). \tag{4.4}$$

Substituting into (4.3) gives

$$\frac{\mathrm{D}k}{\mathrm{D}t} = -Sk, \tag{4.5}$$

where the material derivative, defined as

$$\frac{\mathrm{D}}{\mathrm{D}t} \equiv \frac{\partial}{\partial t} + (c_g + \bar{U})\frac{\partial}{\partial x},$$

denotes changes in time while moving at the speed $c_g + \bar{U}$, and $c_g \equiv \mathrm{d}\sigma/\mathrm{d}k$ is the intrinsic group speed. This is the speed that wave energy, i.e. the dark bands in figure 4.7(b), is expected to propagate through the channel. We have also defined $S \equiv \mathrm{d}\bar{U}/\mathrm{d}x$, which is found to be very nearly constant in the central portion of the laboratory channel (see figure 4.3b). Choosing a Lagrangian frame of reference, that moves at the speed $c_g + \bar{U}$ through the channel, allows for a simple integration of (4.5) to give

$$k(t) = k_* \mathrm{e}^{-S(t-t_*)}, \tag{4.6}$$

where $k_* = k(t_*)$ is some initial value of k that wave energy begins the stretching process at. A direct comparison is now possible between the prediction of (4.6) and the bands of energy in the observed spectral evolution. The prediction is shown by the yellow dashed line in figure 4.7(b), and is found to be in excellent agreement with the observations. This validates the hypothesis that the spectral shift towards lower k is a result of wave stretching. The excellent agreement between the predictions and observations also reveals that our assumption of wave conservation is justified. This is not in contradiction with the formation of new waves described in section 4.6.1 since wave conservation is applied only after energy is fed into the wave field by the instability mechanism.

4.7 Wave Growth and Amplitude

The final basic parameter that we intend to compare is the wave amplitude, a. This feature of the wave field is determined when the linear growth reaches some level where it must saturate. It is a nonlinear property of the waves, and may involve three-dimensional effects as well as interaction with the mean flow. We begin by discussing the various phases of wave growth.

4.7.1 Wave Growth

In the simulation, the instability mechanism causes the growth of waves from an initial random perturbation into a large-amplitude nonlinear wave form. This growth process is best illustrated by considering the kinetic energy of the waves, $\mathcal{K}$. Following Caulfield & Peltier [2000], we partition $\mathcal{K}$ into a two-dimensional kinetic energy $\mathcal{K}_{2d}$ associated with the primary Holmboe wave, and a three-dimensional component $\mathcal{K}_{3d}$, that provides a measure of the departures from a strictly two-dimensional wave. By this partitioning we have

$$\mathcal{K} = \mathcal{K}_{2d} + \mathcal{K}_{3d}, \tag{4.7}$$

where

$$\mathcal{K}_{2d} = \langle \boldsymbol{u}_{2d} \cdot \boldsymbol{u}_{2d}/2\mathcal{K}_0 \rangle_{xz} \quad \text{and} \quad \mathcal{K}_{3d} = \langle \boldsymbol{u}_{3d} \cdot \boldsymbol{u}_{3d}/2\mathcal{K}_0 \rangle_{xyz}, \tag{4.8}$$

and we have used

$$\boldsymbol{u}_{1d}(z,t) = \langle \boldsymbol{u} \rangle_{xy}, \tag{4.9}$$

$$\boldsymbol{u}_{2d}(x,z,t) = \langle \boldsymbol{u} - \boldsymbol{u}_{1d} \rangle_{y}, \tag{4.10}$$

$$\boldsymbol{u}_{3d}(x,y,z,t) = \boldsymbol{u} - \boldsymbol{u}_{1d} - \boldsymbol{u}_{2d}, \tag{4.11}$$

with $\langle \cdot \rangle_i$ representing an average in the direction i, and $\mathcal{K}_0$ the total kinetic energy at $t = 0$.

The $\mathcal{K}_{2d}$ and $\mathcal{K}_{3d}$ components are plotted on a log-scale in figure 4.8 for the simulation. The plot indicates that after a start up period where the energy of the initial perturbation rapidly decays, a stage of exponential growth is achieved in $\mathcal{K}_{2d}$. This stage of exponential growth can be compared to the prediction of linear theory (shown as a thick line), and is found to be slightly less than the prediction. The growth is entirely two-dimensional until the waves have reached a finite amplitude ($t \approx 65$ s), at which point the growth of three-dimensional secondary structures results (see Smyth 2006 for a discussion of this process in Holmboe waves). However, the waves remain primarily two-dimensional, with $\mathcal{K}_{3d}$ at least an order of magnitude smaller than $\mathcal{K}_{2d}$. There is not a well defined transition to turbulence, as is found in other types of stratified shear layers (e.g. Caulfield & Peltier 2000; Smyth, Moum & Caldwell 2001), likely due to the low Re. Once the saturated amplitude is reached, there is a slow decline of $\mathcal{K}$ over the remainder of the simulation.

In the laboratory experiments we have focused only on the period of steady exchange, and therefore do not observe a time-dependent growth of

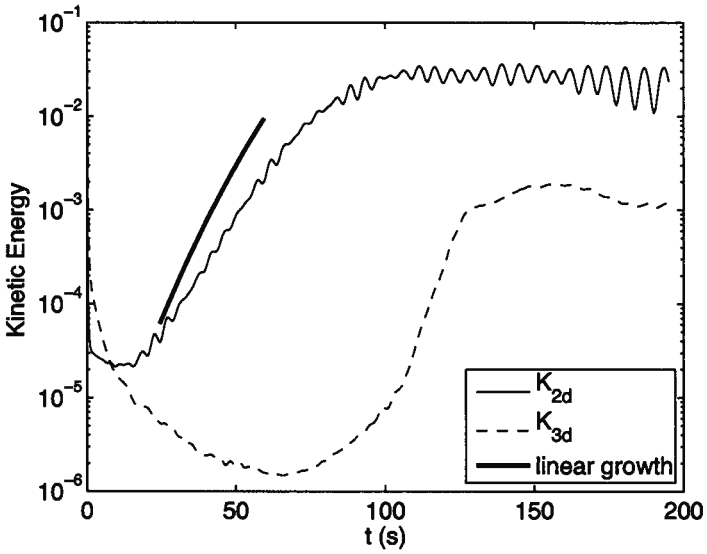

Figure 4.8: Growth of $\mathcal{K}_{2d}$ and $\mathcal{K}_{3d}$ for the simulation. The thick line gives the linear growth rate prediction of the growth of $\mathcal{K}_{2d}$, which is a weak function of time due to the changing background profiles.

the wave field on average. However, as discussed previously, the instability is constantly acting to produce new waves along the channel. It is difficult to measure the growth rate of these waves, but they appear to reach a saturated amplitude rapidly, suggesting that they are strongly forced by disturbances within the channel.

4.7.2 Comparison of Saturated Amplitudes

Although the transient growth of the instability is difficult to quantify in the experiments, it is possible to measure the mean amplitude of the waves. This is done by using the root mean square amplitude of the interface elevation $\eta(x,t)$, given by

$$a_{rms}(x) = \sqrt{\frac{1}{T}\int_T \eta^2 \, \mathrm{d}t}, \tag{4.12}$$

where T denotes the duration of the steady period of exchange. When averaged over a number of experiments a_{rms} is found to display little dependence

on x. A similar a_{rms} can be defined for the simulations, however, the temporal average is replaced by a spatial average in x. The growth of a_{rms} in time in the simulations shows a similar behaviour to $\mathcal{K}_{2d}$; an exponential initial growth, followed by a saturation, and subsequent decay. The saturated (maximum) amplitude reached during each of the simulations is shown in table 4.1, along with the mean amplitude in the experiments.

The first feature to note is that the waves of the two-dimensional simulation (II) at $R = 8$ and $Pr = 700$ (matching the conditions in the experiment) have a lower amplitude than of all the other simulations, especially the two-dimensional simulation (IV) at $R = 5$, $Pr = 25$. This indicates that there is a possible dependence of the saturated amplitude on R, Pr. Most importantly, the amplitude measured in the experiments is significantly smaller than any of the saturated amplitudes reached in the simulations. The small amplitudes observed in the experiments can be explained by, once again, appealing to the effects of wave stretching.

Wave Stretching Effects on Amplitude

To understand the effects of wave stretching on amplitude in the experiments, we apply principles that have been established for waves on slowly varying currents [e.g. Peregrine, 1976]. In doing so, we assume that the Holmboe waves may be represented by a simple train of linear internal waves that satisfy the dispersion relation in figure 4.1(c). We are then able to track the changes in wave amplitude that occur as a result of the spatially varying mean velocity $\bar{U}(x)$, i.e. the wave stretching. In this simplified model it is the conservation of wave action density that is relevant. This is given as E/σ, where E is the wave energy density, and recall that $\sigma(k)$ is the intrinsic wave frequency. Substitution into the conservation law, and following a similar procedure to section 4.6.2 leads to a similar result

$$\frac{\mathrm{D}}{\mathrm{D}t}\left(\frac{E}{\sigma}\right) = -S\left(\frac{E}{\sigma}\right), \tag{4.13}$$

which describes changes in action density due to the stretching by $\bar{U}$. In arriving at (4.13) we have neglected a term that is proportional to $\mathrm{d}^2\sigma/\mathrm{d}k^2$, which is small in the range of k that we are interested in (see figure 4.1c). Taking S to be constant once again, allows for simple integration of (4.13) to give

$$\left(\frac{E}{\sigma}\right) = \left(\frac{E}{\sigma}\right)_* \mathrm{e}^{-S(t-t_*)}.$$

For linear internal waves $E \propto a^2$, so that we have an estimate of the reduction in wave amplitude due to stretching of

$$\frac{a}{a_*} = \sqrt{\frac{\sigma}{\sigma_*}} \mathrm{e}^{-S(t-t_*)/2}. \tag{4.14}$$

If we now take the intrinsic frequency $\sigma \sim k$, as suggested by the linear dispersion relation in figure 4.1(c), it is possible to write the right hand side of (4.14) as $\mathrm{e}^{-S(t-t_*)}$, where we have used the spectral prediction in (4.6). By inspection of figure 4.7(b), we can estimate a time interval, Δt, that wave energy spends in the channel (i.e. the average time interval that the dark bands appear for) to be between 100 and 200 s. The amplitude reduction is therefore in the range $0.37 < \mathrm{e}^{-S\Delta t} < 0.61$.

Given this reduction, and assuming that no other processes are taking place that may affect the wave amplitudes, we would expect amplitudes in the range of that shown in table 4.1, given in parentheses. This adjusted amplitude is comparable to results of the simulations, and demonstrates that – in the absence of other processes – the stretching of wave action is significant in reducing the experimental wave amplitudes.

4.8 Conclusions

We have compared, for the first time, simulations of Holmboe wave fields with the results of laboratory experiments. A meaningful comparison was possible since both methods exhibit only gradual variations in the mean flow. In the laboratory experiment, the mean flow is spatially varying, whereas the numerical simulations display a temporal variation. Focusing on basic descriptors of the waves, such as phase speed, wavenumber, and amplitude, we have identified a number of processes affecting the nonlinear behaviour of Holmboe wave fields.

Similarities between results of the two methods include the basic structure of the waves, and the phase speeds. The observations show slightly greater phase speeds when compared with the predictions of linear theory, in agreement with previous studies [Haigh, 1995; Hogg & Ivey, 2003]. Further departures from the linear predictions are attributed to a nonlinear dependence of the phase speed on amplitude.

The greatest differences between simulation and experiment are found in the spectral evolution and wave amplitudes. In simulations, a transfer of wave energy to lower k was found to result from wave coarsening, which caused waves to be 'lost' through discrete merging events. These events

were found, at least in part, to result from the vortex pairing and ejection processes. The latter of which is suggested to be similar to wave breaking in surface waves, since it appears to act preferentially to reduce the amplitude of the largest waves. A detailed investigation of both ejections and vortex pairing in Holmboe waves is currently underway.

The shift of wave energy to lower k that was observed in the experiments can be attributed to the 'stretching' of the wave field by the spatially accelerating mean flow. This suggestion of Tedford *et al.* [2009] (Chapter 2) has been confirmed by a simple application of gradually varying wave theory, which is able to accurately predict the time dependence of the spectral shift.

The wave stretching process is also expected to have a significant effect in reducing the wave amplitudes observed in the experiments. This conclusion appears sufficient to explain discrepancies between wave amplitudes in experiment and simulation, and is based on a simple application of the conservation of wave action. In this application we have assumed that no other processes are actively influencing the wave amplitude, however, a dependence of wave amplitude on R, Pr has been noted.

A general result of this comparison is that the nonlinear evolution of a Holmboe wave field is dependent on the mean flow, and hence, on the boundary conditions. This must be considered when studying the nonlinear behaviour of the Holmboe instability.

Bibliography

ALEXAKIS, A. 2005 On Holmboe's instability for smooth shear and density profiles. *Phys. Fluids* **17**, 084103.

ARMI, L. & FARMER, D. 1988 The flow of Mediterranean water through the strait of Gibraltar. On the mechanism of shear flow instabilities. *Prog. Oceanogr.* **21**, 1–98.

BALMFORTH, N. J. & MANDRE, S. 2004 Dynamics of roll waves. *J. Fluid Mech.* **514**, 1–33.

BROWAND, F.K. & WINANT, C.D. 1973 Laboratory observations of shear-layer instability in a stratified fluid. *Boundary-Layer Met.* **5**, 67–77.

CARPENTER, J.R., LAWRENCE, G.A. & SMYTH, W.D. 2006 Instability mechanisms in asymmetric stratified shear layers. *Proceedings* 6^{th} *International Symposium on Stratified Flows* pp. 14–19.

CARPENTER, J.R., LAWRENCE, G.A. & SMYTH, W.D. 2007 Evolution and mixing of asymmetric Holmboe instabilities. *J. Fluid Mech.* **582**, 103–132.

CAULFIELD, C.P. & PELTIER, W.R. 2000 The anatomy of the mixing transition in homogenous and stratified free shear layers. *J. Fluid Mech.* **413**, 1–47.

HAIGH, S.P. 1995 Non-symmetric Holmboe waves. PhD thesis, University of British Columbia.

HAZEL, P. 1972 Numerical studies of the stability of inviscid stratified shear flows. *J. Fluid Mech.* **51**, 39–61.

HOGG, A. MCC. & IVEY, G.N. 2003 The Kelvin-Helmholtz to Holmboe instability transition in stratified exchange flows. *J. Fluid Mech.* **477**, 339–362.

HOLMBOE, J. 1962 On the behavior of symmetric waves in stratified shear layers. *Geofys. Publ.* **24**, 67–112.

HUANG, N. E., LONG, S. R. & SHEN, Z. 1996 The mechanism for frequency downshift in nonlinear water wave evolution. *Adv. Appl. Mech.* **32**, 59–117.

HUANG, N. E., SHEN, Z. & LONG, S. R. 1999 A new view of nonlinear water waves: the Hilbert spectrum. *Annu. Rev. Fluid Mech.* **31**, 417–457.

KOPPEL, D. 1964 On the stability of a thermally stratified fluid under the action of gravity. *J. Meth. Phys.* **5**, 963–982.

PAWLAK, G. & ARMI, L. 1996 Stability and mixing of a two-layer exchange flow. *Dyn. Atmos. Oceans* **24**, 139–151.

PEREGRINE, D. H. 1976 Interaction of water waves and currents. *Adv. Appl. Mech.* **16**, 9–117.

SARGENT, F.E. & JIRKA, G.H. 1987 Experiments on saline wedge. *J. Hydraul. Engng ASCE* **113** (10), 1307–1324.

SMYTH, W.D. 2006 Secondary circulations in Holmboe waves. *Phys. Fluids* **18** (064104), 1–13.

SMYTH, W.D., CARPENTER, J.R. & LAWRENCE, G.A. 2007 Mixing in symmetric Holmboe waves. *J. Phys. Oceanogr.* **37**, 1566–1583.

SMYTH, W.D., KLAASSEN, G.P. & PELTIER, W.R. 1988 Finite amplitude Holmboe waves. *Geophys. Astrophys. Fluid Dyn.* **43**, 181–222.

SMYTH, W.D., MOUM, J.N. & CALDWELL, D.R. 2001 The efficiency of mixing in turbulent patches: Inferences from direct simulations and microstructure observations. *J. Phys. Oceanogr.* **31**, 1969–1992.

SMYTH, W.D., NASH, J.D. & MOUM, J.N. 2005 Differential diffusion in breaking Kelvin-Helmholtz billows. *J. Phys. Oceanogr.* **35**, 1004–1022.

SMYTH, W.D. & PELTIER, W.R. 1990 Three-dimensional primary instabilities of a stratified, dissipative, parallel flow. *Geophys. Astrophys. Fluid Dyn.* **52**, 249–261.

SMYTH, W.D. & WINTERS, K.B. 2003 Turbulence and mixing in Holmboe waves. *J. Phys. Oceanogr.* **33**, 694–711.

TEDFORD, E.W., PIETERS, R. & LAWRENCE, G.A. 2009 Symmetric Holmboe instabilities in a laboratory exchange flow. *J. Fluid Mech.* p. to appear.

TULIN, M. P. & WASEDA, T. 1999 Laboratory observations of wave group evolution, including breaking effects. *J. Fluid Mech.* **378**, 197–232.

WESSON, J. C. & GREGG, M. C. 1994 Mixing at Camarinal Sill in the Strait of Gibraltar. *J. Geophys. Res.* **99**, 9847–9878.

WINTERS, K.B., MACKINNON, J.A. & MILLS, B. 2004 A spectral model for process studies of rotating, density-stratified flows. *J. Atmos. Ocean. Tech.* **21**, 69–94.

YONEMITSU, N., SWATERS, G.E., RAJARATNAM, N. & LAWRENCE, G.A. 1996 Shear instabilities in arrested salt-wedge flows. *Dyn. Atmos. Oceans* **24**, 173–182.

YOSHIDA, S., OHTANI, M., NISHIDA, S. & LINDEN, P.F. 1998 Mixing processes in a highly stratified river. In *Physical Processes in Lakes and Oceans, Coastal and Estuarine Studies*, vol. 54, pp. 389–400. American Geophysical Union.

ZHU, D. & LAWRENCE, G.A. 2001 Holmboe's instability in exchange flows. *J. Fluid Mech.* **429**, 391–409.

Chapter 5

Conclusion

5.1 Summary

Holmboe instabilities have been studied in the laboratory, the field and with direct numerical simulations (DNS). The instabilities were a result of interaction between shear and a density interface.

In the laboratory the instabilities were observed on the density interface of a two-layer exchange flow. The analysis was focussed on the middle portion of the channel where velocity and density profiles most closely matched the original model of Holmboe [1962]. The simplicity of the flow resulted in a relatively uniform wave field, which, combined with the prolonged period of steady exchange, provided instabilities with average wave properties in good agreement with the linear predictions of Holmboe.

The gradual slope of the interface along the length of the channel resulted in convective acceleration within each layer. The Holmboe instabilities experienced an equivalent acceleration as they propagated along the channel. This acceleration caused the waves to stretch until they were approximately twice the most amplified wavelength allowing new waves to form. The new waves formed uniformly along the channel such that the average wavelength was nearly constant and slightly greater than the most amplified wavelength.

The conditions in the Fraser River salinity intrusion provided a variety of shear instabilities for investigation. Although none were identical to the symmetric Holmboe instabilities of the laboratory many were similar in that they had crests or troughs that cusped away from the density interface. Some of these had billows or wisps that were displaced vertically from the density interface. As in the case of the laboratory experiments, linear predictions based on the Taylor-Goldstein (TG) equation compared well with the observed instabilities.

In chapter 4 the results from the laboratory experiments were compared with Direct Numerical Simulations (DNS). The DNS provided predictions of non-linear aspects of the instabilties, such as the shape of the density interface and the maximum amplitude. The initial and boundary conditions of the DNS did not exactly match those of the laboratory experiments resulting

in significant differences. However, the density interface had a similar cusp like appearance and once the differences in the mean flow were accounted for the amplitudes of the instabilities were well matched.

5.2 The Occurrence of Holmboe and Holmboe-Like Instabilities

In Chapter 1, the basic instabilities that occur in shear flows with stable density stratification were described in terms of the interaction of two interfaces: the Kelvin-Helmholtz (KH) instability resulted from the interaction of two vorticity interfaces (Rayleigh mechanism); the Taylor instability from the interaction of two density interfaces; and the Holmboe instability from the interaction of one vorticity interface and one density interface. The instabilities in both the laboratory and field study resembled the Holmboe mode most often.

The regular occurrence of Holmboe instabilities discussed in Chapters 2 and 4 has not generally been observed in laboratory experiments of salt stratified exchange flows, especially those that have used relatively short channels. The high degree of non-uniformity that occurs in short channels diminishes the regularity of propagating waves [e.g. the Holmboe instabilities observed by Hogg & Ivey, 2003]. On the other hand, stationary waves (i.e. KH instabilities) are not as strongly influenced by non-uniformity.

In the Fraser River estuary Holmboe-like instabilities were also present. However, the presence of multiple vorticity and density interfaces makes classification more difficult. In some cases, the instabilities are potentially the result of the interaction of more than two interfaces.

5.3 Contributions to the Study of Shear Instabilities in Stratified Flows

5.3.1 Laboratory Experiments

The laboratory work described in Chapter 2 was, in its very early stages, meant to form a baseline for proposed experiments focussed on the impact of barotropic oscillations on a two-layer exchange flow. The proposed experiments were specifically intended to model the two-layer exchange flow in the Burlington Ship Canal [Lawrence *et al.*, 2004]. Modifying the channel used by Zhu & Lawrence [2001] to more closely match the Burlington Ship canal (i.e. removing the sill and reducing the depth) inadvertently created

optimal conditions for generating symmetric, regularly occurring, Holmboe instabilities. This setup, two reservoirs connected by a long straight channel, is the simplest possible for studying stratified shear instabilities in a steady, nearly uniform, background flow. The long channel also provides a length to depth aspect ratio that is more representative of geophysical flows. In addition to clearly demonstrating the occurrence of Holmboe instabilities, Chapter 2 provides a foundation for future research in similar facilities.

The wave properties (i.e. phase speed, wavelength and frequency) of the instabilities were described quantitatively. This description relied on several techniques, the most important of which was filtering with the two dimensional Fourier transform (2DFFT). Because the experiments consisted of a long section of subcritical flow that was steady, the 2DFFT was effective in separating the instabilities into positive (rightward propagating) and negative (leftward propagating) modes. In comparison, in the experiments of Zhu & Lawrence [2001], the phase velocity of the negative modes changed sign (from rightward to leftward propagating), which would render the 2DFFT less effective in separating the two modes. Once the instabilities were separated into positive and negative modes, the quantification of the wave properties was straightforward and allowed direct comparison with the linear theory.

5.3.2 Field Experiments

Shear instabilities were observed in the Fraser River estuary using simultaneous measurements of velocity, density and echo intensity. Drifting with the upper layer allowed profiling of the CTD in a highly sheared flow while simultaneously logging high quality sounder and ADCP data. The use of a load bearing data cable for the CTD allowed us to quickly locate the front of the salinity intrusion. To my knowledge, previous studies of the Fraser River salinity intrusion did not use these techniques.

In the stability analysis, a vertical low-pass filter was used on the velocity profiles to ensure smooth profiles of d^2U/dz^2. Multiple hyperbolic tangents were used to remove statically unstable features from the density profiles, while retaining step-like features. This careful processing of the velocity and density profiles allowed application of the TG equation in a relatively complex flow. Knowledge of the basic stable and unstable modes outlined in Chapter 1 aided in interpreting the results of the stability analysis.

5.3.3 Direct Numerical Simulations

We have compared, for the first time, simulations of Holmboe wave fields with the results of laboratory experiments. The use of multi-wavelength domains combined with random perturbations allowed a number of important mechanisms to be modelled with DNS. These include, wave-group behaviour, vortex pairing and ejections. The use of the 2DFFT allowed us to compare the spectral evolution of the waves. In the DNS, vortex pairing and ejections resulted in wave energy getting shifted in discrete steps to longer and longer wavelengths. In contrast, in the laboratory exchange flow, wave energy moved continuously to longer wavelengths due to spatial acceleration. The wave stretching in the laboratory reduced the height of waves relative to the DNS.

5.4 Future Research

The most common criticism of laboratory experiments and DNS is their low Reynolds number. The use of larger laboratory facilities and more powerful computers could address this issue in future research. During the course of this study we have built a larger exchange flow facility that will allow an increase in the depth of flow to 0.6 m. This will increase the Reynolds number by a factor of approximately 5. The use of a stronger density gradient between the two reservoirs, i.e. more salt, will generate higher velocities and also higher Reynolds numbers. Higher velocities will require a camera with greater frame rate and sensitivity.

Once Holmboe instabilities can be modelled at higher Reynolds number either physically or numerically, the associated mixing should be quantified. While it is straightforward to quantify mixing in DNS, it is challenging in laboratory flows. Integrative methods are typically the most accurate, however, these generally sum the effects of all of the mechanisms that cause mixing [see Prastowo *et al.*, 2008]. Specifically, mixing caused by turbulence generated at no slip boundaries (the bottom and side walls) must be separated from mixing caused by shear instabilities. Micro conductivity-temperature (CT) probes and laser induced fluorescence could also be used to measure mixing. CT probes require a large channel so that the action of the probes does not significantly alter the flow or mixing.

The long term goal in the Fraser River estuary is to conduct higher resolution sampling over the full range of freshwater discharge. A CTD with a higher sampling rate would provide greater horizontal and vertical resolution of the density field. In addition, the simultaneous use of multiple

echosounders could provide a more direct measure of the phase speed and wavelength of internal waves. The work described in Chapter 3 focussed on observing and identifying shear instabilities. Future work should include a component focussed on quantifying the mixing associated with these instabilities. This would require either multiple transects in rapid succession or multiple moorings along the length of the salinity intrusion. Future studies of mixing should also examine three dimensional aspects, particularily in the rivers bends. These features may have a strong infuence on shear instabilities and associated mixing.

Bibliography

HOGG, A. McC. & IVEY, G.N. 2003 The Kelvin-Helmholtz to Holmboe instability transition in stratified exchange flows. *J. Fluid Mech.* **477**, 339–362.

HOLMBOE, J. 1962 On the behavior of symmetric waves in stratified shear layers. *Geofys. Publ.* **24**, 67–112.

LAWRENCE, G.A., PIETERS, R., ZAREMBA, L., TEDFORD, T., GU, L., GRECO, S. & HAMBLIN, P. 2004 Summer exchange between Hamilton Harbour and Lake Ontario. *Deep-Sea Res. II* **51**, 475–487.

PRASTOWO, T., GRIFFITHS, R.W., HUGHES, G.O. & HOGG, A.McC. 2008 Mixing efficiency in controlled exchange flows. *J. Fluid Mech.* **600**, 235–244.

ZHU, D. & LAWRENCE, G.A. 2001 Holmboe's instability in exchange flows. *J. Fluid Mech.* **429**, 391–409.